ELECTROCHEMICAL IMPEDANCE SPECTROSCOPY FOR THE STUDY OF CATALYSIS AND ELECTRODE DEGRADATION IN VANADIUM REDOX-FLOW BATTERIES

Dissertation
to obtain the academic degree

Doctor rerum naturalium
(Dr. rer. nat.)

submitted to the Department
of Biology, Chemistry, Pharmacy of
Freie Universität Berlin

by

Jonathan Schneider

December 2022

This thesis was written in original TeX language developed by Donald E. Knuth and typset using a custom version of the LaTeX template by Leslie Lamport accessible at `https://hci.rwth-aachen.de/karrer-thesistemplate`.

I hereby declare that I have created this work completely on my own and used no other sources or tools than the ones listed, and that I have marked any citations accordingly. This thesis has not been accepted or rejected in any previous doctoral process.

....

Berlin, December *2022*
Jonathan Schneider

Abstract

Vanadium redox-flow batteries (VRFBs) are emerging as promising systems for large-scale energy storage. Yet, certain key aspects require for substantial improvements in order to achieve broad commercial success of this technology. In that respect, further development of electrode materials in terms of increased and durable electrocatalytic activity is of essence, especially in the negative half cell. Myriads of approaches for surface modification of the predominantly employed macroporous carbons have thus been proposed so far. However, upon thorough review of pre-existing literature, it became evident that meaningfully benchmarking and quantifying the effects of those procedures with regard to resulting performance enhancement is anything but a straightforward task. The emphasis of this thesis was therefore put on establishing methodical approaches for reliable and unambiguous quantification of electrode kinetics by properly utilizing electrochemical techniques, predominantly electrochemical impedance spectroscopy (EIS), and exploiting their full capabilities.

In an exemplary study on bismuth-modified carbon felt electrodes it was demonstrated how applying proper normalization to *ex-situ* impedance data enables thorough characterization and standardized comparison of electrocatalytic effects induced by incorporation of metal (oxide) particles or any other type of supposedly activating treatment. Intrinsic catalytic activity of Bi for the $V(II)/V(III)$ redox reaction has been verified and stability of modified electrodes was assessed for the first time. By eliminating the often misleading impact of electrode wetting, reproducibility of obtained results was greatly enhanced compared to other approaches commonly pursued in the open literature.

Subsequently, the innovative concept of distribution of relaxation times (DRT) analysis was introduced to the field of *in-situ* examination of VRFB cells. Loss

processes during operation of the battery have been unraveled before proving the feasibility of DRT-based monitoring of electrode ageing. Gained insights underline the importance of keeping future research focused on the negative half cell electrode, at least in terms of electrocatalysis and degradation.

Further investigations explored how synergistic use of additional techniques may complement the experimental capabilities of EIS to determine electrode characteristics in the most comprehensive way. This involved unequivocal separation of respective current contributions from V^{3+}-reduction and parasitic hydrogen evolution reaction (HER) at planar model electrodes during rotating ring-disc electrode (RRDE) and alternating current cyclic voltammetry (ACCV) measurements as well as visualization of bismuth dissolution and redeposition in an operating VRFB by utilization of X-ray-based imaging procedures.

Zusammenfassung

Vanadium-Redox-Flow-Batterien gelten als vielversprechende Systeme für die elektrochemische Energiespeicherung in großtechnischem Maßstab. Bestimmte Schlüsselaspekte bedürfen jedoch erheblicher Verbesserungen, um einen endgültigen kommerziellen Durchbruch dieser Technologie zu ermöglichen. In diesem Zusammenhang ist die Weiterentwicklung der Elektrodenmaterialien bezüglich erhöhter elektrokatalytischer Aktivität und Langlebigkeit essentiell, insbesondere in der negativen Halbzelle. Daher wurden bisher unzählige Ansätze zur Oberflächenmodifikation der bevorzugt eingesetzten makroporösen Kohlenstoffe vorgeschlagen. Eine ausführliche Begutachtung der diesbezüglich verfügbaren Studien legt jedoch den Schluss nahe, dass ein fundierter Vergleich dieser Verfahren auf Grundlage einer verlässlichen Quantifizierung der erzielten Leistungssteigerungen diverse Hürden mit sich bringt. Folglich lag der Schwerpunkt dieser Arbeit darauf, durch zweckmäßigen Gebrauch und das Ausreizen des vollen Anwendungspotentials von elektrochemischen Analyseverfahren, vordergründig der elektrochemischen Impedanzspektroskopie (EIS), methodische Ansätze für die belastbare Untersuchung und eineindeutige Bestimmung von Elektrodenkinetik sowie damit verbundenen Parametern zu entwickeln.

In einer exemplarischen Untersuchung Bismut-modifizierter Kohlenstofffilzelektroden wurde gezeigt, wie die Anwendung eines geeigneten Normalisierungsansatzes auf *ex-situ* gewonnene Impedanzdaten eine umfassende Charakterisierung und den standardisierten Vergleich elektrokatalytischer Effekte ermöglicht, welche durch eine vermeintlich aktivierende Behandlung der Elektrode (z.B. durch Dekoration mit Metall(oxid)partikeln) hervorgerufen wurden. Hierdurch konnten die intrinsische katalytische Aktivität von Bi hinsichtlich der V(II)/V(III)-Redoxreaktion zweifelsfrei nachgewiesen und die Langzeitstabilität

der modifizierten Elektroden bewertet werden. Durch die Eliminierung des oft irreführenden Einflusses schwankender Benetzungsgrade der Elektroden wurde zudem die Reproduzierbarkeit der erzielten Ergebnisse im Vergleich zu den in der Literatur üblicherweise verfolgten Ansätzen erheblich verbessert.

Anschließend wurde das innovative Konzept der Analyse von Relaxationszeit-verteilungen (engl.: distribution of relaxation times - DRT) erstmalig auf die *in-situ*-Untersuchung von VRFB-Zellen angewendet. Nach erfolgreicher Entschlüsselung und Zuordnung der im Betrieb auftretenden Verlustprozesse konnte die Machbarkeit einer DRT-basierten operativen Überwachung der Elektrodenalterung demonstriert wurde. Die gewonnenen Erkenntnisse unterstreichen die dringende Notwendigkeit, den Fokus künftiger Forschungsarbeiten mit Bezug zu Elektrokatalyse und Degradation vornehmlich auf die Elektrode der negativen Halbzelle zu konzentrieren.

In weiterführenden Arbeiten wurde ergründet, wie unter Zuhilfenahme komplementärer Methoden die aufklärerischen Fähigkeiten der EIS synergistisch erweitert werden können, um ein vollumfängliches Bild der untersuchten Elektrodeneigenschaften zu erhalten. In diesem Zusammenhang sind die Unterscheidung der jeweiligen Strombeiträge von V^{3+}-Reduktion und parasitärer Wasserstoffentwicklung an planaren Modellelektroden mittels rotierender Ring-Scheiben-Elektroden (engl.: rotating ring-disk electrode - RRDE) und Wechselstrom-Zyklovoltammetrie (engl.: alternating current cyclic voltammetry - ACCV) sowie die Visualisierung der Auflösung und erneuten Abscheidung von Bismutpartikeln während des Betriebs einer VRFB durch den Einsatz bildgebender Röntgenverfahren zu nennen.

List of Publications

Publications to be considered in this Thesis

J. Schneider, E. Bulczak, G. A. El-Nagar, M. Gebhard, P. Kubella, M. Schnucklake, A. Fetyan, I. Derr, C. Roth, Degradation phenomena of bismuth-modified felt electrodes in VRFB studied by electrochemical impedance spectroscopy, *Batteries* **2019**, 5, 16. DOI: 10.3390/batteries5010016.

J. Schneider, T. Tichter, P. Khadke, R. Zeis, C. Roth, Deconvolution of electrochemical impedance data for the monitoring of electrode degradation in VRFB, *Electrochim. Acta* **2020**, 336, 135510. DOI: 10.1016/j.electacta.2019.135510.

T. Tichter, J. Schneider, D. N. Viet, A. Diaz Duque, C. Roth, Rotating ring-disc electrode measurements for the quantitative electrokinetic investigation of the V^{3+}-reduction at modified carbon electrodes, *J. Electroanal. Chem.* **2020**, 859, 113843. DOI: 10.1016/j.jelechem.2020.113843.

M. Gebhard, T. Tichter, J. Schneider, J. Mayer, A. Hilger, M. Osenberg, M. Rahn, I. Manke, C. Roth, On the stability of bismuth in modified carbon felt electrodes for vanadium redox flow batteries: An in-operando X-ray computed tomography study, *J. Power Sources* **2020**, 478, 228695. DOI: 10.1016/j.jpowsour.2020.228695.

Publications not to be considered

A. Fetyan, G. A. El-Nagar, I. Lauermann, M. Schnucklake, **J. Schneider**, C. Roth, Detrimental role of hydrogen evolution and its temperature-dependent impact on the performance of vanadium redox flow batteries, *J. Energy Chem.* **2019**, 32, 57-62. DOI: 10.1016/j.jechem.2018.06.010.

T. Tichter, D. Andrae, J. Mayer, **J. Schneider**, M. Gebhard, C. Roth, Theory of cyclic voltammetry in random arrays of cylindrical microelectrodes applied to carbon felt electrodes for vanadium redox flow batteries, *Phys. Chem. Chem. Phys* **2019**, 21, 9061–9068. DOI: 10.1039/c9cp00548j.

M. Schnucklake, L. Eifert, **J. Schneider**, R. Zeis, C. Roth, Porous n- and s-doped carbon-carbon composite electrodes by soft-templating for redox flow batteries, *Beilstein J. Nanotechnol.* **2019**, 10, 1131–1139. DOI: 10.3762/bjnano.10.113.

A. Fetyan, **J. Schneider**, M. Schnucklake, G. A. El-Nagar, R. Banerjee, N. Bevilacqua, R. Zeis, C. Roth, Comparison of electrospun carbon-carbon composite and commercial felt for their activity and electrolyte utilization in vanadium redox flow batteries, *ChemElectroChem* **2019**, 6, 130–135. DOI: 10.1002/celc.201801128.

T. Tichter, **J. Schneider**, D. Andrae, M. Gebhard, C. Roth, Universal algorithm for simulating and evaluating cyclic voltammetry at macroporous electrodes by considering random arrays of microelectrodes, *ChemPhysChem* **2020**, 21, 428–441. DOI: 10.1002/cphc.201901113.

T. Tichter, D. Andrae, **J. Schneider**, M. Gebhard, A. Hilger, I. Manke, C. Roth, Real-space simulation of cyclic voltammetry in carbon felt electrodes by combining micro ct data, digital simulation and convolutive modeling, *Electrochim. Acta* **2020**, 353, 136487. DOI: 10.1016/j.electacta.2020.136487.

M. Maleki, G. A. El-Nagar, D. Bernsmeier, **J. Schneider**, C. Roth, Fabrication of an efficient vanadium redox flow battery electrode using a freestanding carbon-loaded electrospun nanofibrous composite, *Sci. Rep.* **2020**, 10, 11153. DOI: 10.1038/s41598-020-67906-6.

T. TICHTER, **J. SCHNEIDER**, C. ROTH, Finite heterogeneous rate constants for the electrochemical oxidation of VO^{2+} at glassy carbon electrodes, *Front. Energy Res.* **2020**, 8, 155. DOI: 10.3389/fenrg.2020.00155.

K. SCHUTJAJEW, T. TICHTER, **J. SCHNEIDER**, M. ANTONIETTI, C. ROTH, M. OSCHATZ, Insights into the sodiation mechanism of hard carbon-like materials from electrochemical impedance spectroscopy, *Phys. Chem. Chem. Phys.* **2021**, 23, 11488–11500. DOI: 10.1039/d1cp00610j.

T. TICHTER, **J. SCHNEIDER**, C.ROTH *Electrochemical Methods* in *Flow Batteries: From Fundamentals to Applications*, (EDS.: C. ROTH, J. NOACK, M. SKYLLAS-KAZACOS), Wiley-VCH, Weinheim, **2023**. ISBN: 978-3-527-34922-7.

Conference Contributions

J. SCHNEIDER, R. ZEIS, M. A. DANZER, C. ROTH, Degradation study of VRFB using distribution of relaxation times analysis, *GdCH Electrochemistry* **2018**, Ulm, Germany. (Poster)

J. SCHNEIDER, T. TICHTER, R. ZEIS, M. A. DANZER, C. ROTH, Deconvolution of electrochemical impedance data for the monitoring of electrode degradation in VRFB, *International Flow Battery Forum* **2019**, Lyon, France. (Poster)

J. SCHNEIDER, T. TICHTER, C. ROTH, Understanding the vanadium redox-flow battery: an in-depth study using the distribution of relaxation times analysis *RedoxFlow2020* **2020**, web conference. (Talk)

Contents

X

Chapter 1

Introduction

1.1 Significance and objective

The concerted, world-wide efforts to terminate emission of greenhouse gases necessitate a massive expansion of global sustainable energy generation capabilities. This process of energy transition is unique in human history in that it not only adds and integrates e.g. wind and solar power to the energy mix but on the other hand also aims to back out of the generation of energy from unsustainable sources such as coal, oil or natural gas. Following the political milestones of the Kyoto Protocol in 1997 or the Paris Agreement in 2015 [1, 2], the vast majority of industrialized nations have established national and transnational strategies targeted at limiting global warming (with respect to the pre-industrial era) to 1.5 °C by the year 2050. As the energy sector contributed around 76 % of greenhouse gas emissions globally and 77 % within the European Union in 2019 [3, 4], *decarbonising* it by the aforementioned replacement of conventional energy sources with sustainable ones is the largest setscrew for achieving those ambitious goals. In Germany, renewable energy produced from wind, photovoltaics, biomass and hydropower contributed 45.8 % (equivalent to 225 TW h) of the total net electricity generation in 2021 [5]. This share should be increased to 100 % by the year 2050 [6].

Due to the highly intermittent nature of these energy sources, the importance of

energy storage technologies will rise in order to ensure stability of the electrical grid. Given the obvious shortcomings, namely low flexibility and high environmental impact, of today's predominantly utilized technologies pumped hydro and compressed air energy storage, electrochemical energy storage systems have drawn considerable attention in recent years. Among these, redox-flow batteries (RFBs) and especially the vanadium redox-flow battery (VRFB), are widely considered viable candidates [7, 8]. Although inferior in terms of energy density and investment cost when compared to e.g. Li-Ion batteries, VRFBs are emerging as strong competitor due to advantages such as very long cycle-life, flexible scalability, absence of fire hazard or the inherit need for critical minerals and easy recyclability. In a recent technical report commissioned by the U.S. Department of Energy (DOE) [9], the projected cost for a 100 MW, 10 h storage system were estimated at 356 \$/kWh and 366 \$/kWh for Li-Ion batteries of the LFP- and NMC-type, respectively and at 399 \$/kWh for a VRFB. Annualized cost on the other hand were considered to be 93 \$/kWh, 140 \$/kWh and 65 \$/kWh, respectively.

In order to take full advantage of this economic potential, real VRFB systems have to achieve or better exceed their predicted lifetime of 20 years and 10000 cycles [10, 11]. Therefore, all degradation processes that occur during operation of the battery, or even during times of rest, have to be fully understood before measures to maximize the lifetime can be taken. This is where the joint research project *DegraBat*, funded by the Federal Ministry for Economic Affairs and Energy (BMWi), set in. In a collaborative effort of partners from science and industry, component-specific degradation phenomena in VRFB have been systematically studied throughout the project duration between July 2017 and January 2021. After implementing suitable methods for material characterization and online-monitoring (to estimate e.g. state of charge (SOC) or membrane resistance), a profound understanding regarding the aging of cell components should be gained and used to develop respective accelerated degradation protocols. The ultimate goal was to quantify the influence of degradation processes on key performance indicators such as energy efficiency or maximum discharge power density and subsequently develop an aging model which would allow for estimation of lifetime, cost and optimal operating conditions of a single-cell VRFB. The processing of the the work packages associated with the subproject *electrodes* in the labs of Prof. Christina Roth at Freie Universität Berlin finally lead to the emergence of the present thesis.

Macroporous carbon-based electrodes are crucial components in VRFB systems, as they provide the large electrochemically active surface area (ECSA) for the

respective redox reactions to take place. In other words, the electrode-electrolyte interface is where the conversion from electrical to chemical energy (and vice versa) occurs, ultimately enabling the storage and supply of energy using a VRFB. Any change in the electrode's functional surface composition and/or morphology is presumably altering the interfacial redox kinetics and thus directly affecting the battery's conversion efficiency. While this opens up immense possibilities to increase battery performance - and therefore profitability - by adding electrocatalytically active moieties (like metal or metal oxide nanoparticles, heteroatom-containing functional groups, edge sites, ...), any such change induced by (electro)chemical degradation processes is likely to have a negative impact. Consequently, parasitic side reactions like the hydrogen evolution reaction (HER) in the negative half cell will become more pronounced and lead to an electrolyte imbalance which constitutes an irreversible capacity loss. Therefore, electrode degradation is among the factors that limit life expectancy of a VRFB. As such, it has to be comprehensively analysed, understood and, finally, mitigated.

Although a plethora of studies proposed a huge variety of novel electrocatalysts for use in VRFB, the available literature on electrode degradation appears to be rather scarce, while catalyst durability is hardly ever assessed. Furthermore, reported results are often contradictory and sometimes even misleading. This is largely owing to the fact that many investigations have been focused predominantly on the *ex-situ* characterization of electrode materials. Large efforts are taken to assess material properties by micro- and spectroscopic methods while electrochemical methods are often not utilized to their full potential and sometimes simply misinterpreted. Also, reproducibility of results is a severe issue in (*ex-situ*) electrochemical testing of electrode materials in VRFB which remains largely disregarded. This complicates the act of drawing reliable conclusions regarding the relationship between an electrode's composition and morphology on one hand and it's kinetic properties (and durability) on the other.

The foremost goal of the present thesis is therefore to elevate the scientific discourse in VRFB research by outlining methodologies for reliable, robust and reproducible assessment of electrode kinetics. The experimental technique of choice will be electrochemical impedance spectroscopy (EIS), owing to its non-invasive, non-destructive nature, its flexible applicability for both *in-situ* and *ex-situ* measurements as well as the straightforward distinction of different processes based on their characteristic frequencies it enables. By exploring mitigation strategies to common experimental pitfalls in *ex-situ* EIS, discussing measures to assure data quality and finally introducing the novel concept of dis-

tribution of relaxation times (DRT) analysis to the study of single-cell VRFBs, EIS will be established as an essential tool to assess electrode kinetic properties, study the effects of electrode modifications or degradation and evaluate catalyst durability in the context of VRFBs.

1.2   Outline

The contents presented herein are organized as follows. Chapter 2 will provide a fundamental understanding regarding the main aspects of the subject matter. In section 2.1, the basic design principles, materials, electrode reactions and common benchmarking routines of VRFBs are discussed. The subsequent section 2.2 constitutes a critical review of pre-existing literature concerning macroporous carbon-based electrode materials. The focus here will be on kinetic properties, surface modifications aimed at enhancing them as well as degradation. In section 2.3, the reader will be familiarized with the basic principles of EIS before being introduced to the theory behind the advanced concept of DRT analysis. Chapter 3 is of particular interest for any experimental electrochemist. It discusses neccessary actions to be taken in order to obtain reproducible results and consistently high data quality during both *ex-situ* and *in-situ* EIS (sections 3.1 and 3.2, respectively). All peer-reviewed journal articles included in this thesis are discussed and reprinted in chronological order of publication within chapters 4 and 5. The concluding chapter 6 serves to put them into perspective, highlight their substantial interrelations and derive possible directions of future research activities.

Chapter 2

State of the art

2.1 Fundamental aspects of RFB systems

The development of what is today known as a redox-flow battery (RFB) dates back to the 1940's with *Kangro* demonstrating a chromium-based RFB within a patent that he applied for in 1949 and which was finally granted in 1954 [12]. He described a system, in which electrical energy can be stored via redox reactions of redox couples dissolved in liquids which are passed through half-cells into seperate storage tanks. By passing the liquids back through, redox reactions might as well be reversed. This fundamental design principle essentially decouples power from energy in that both can be scaled independently by changing the size of either the electrochemical cell or the storage tanks. This feature sets RFBs apart from other types of batteries and shows their strong relationship to fuel cells. The schematic of an exemplary RFB is illustrated in Fig. 2.1. It shows the tanks storing the electrolytes of negative (*anolyte* or *negolyte*) and positive half-cell (*catholyte* or *posolyte*), respectively. Using two pumps, the electrolytes are circulated through the heart of the battery system - the electrochemical cell, where the actual conversion takes place. Additional components like power converters and battery management system are not shown for the sake of simplicity and only a single cell is depicted, even though real systems operating outside the lab will feature a multiple of cells
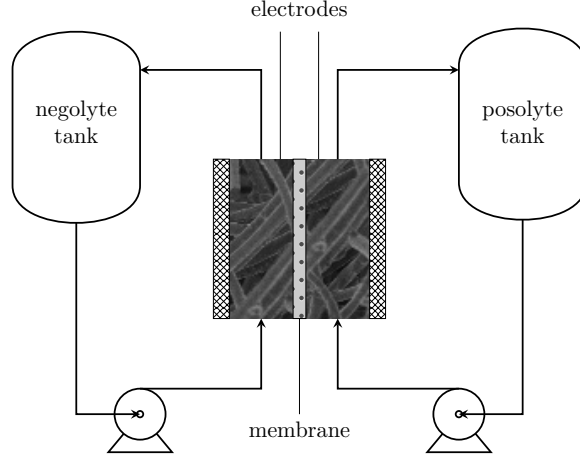
Figure 2.1: Basic schematic of a single-cell RFB system.

electrically connected in series - the *stack*. In a single cell, the two respective half-cells are commonly seperated by means of a membrane that accounts for a balancing of ion concentrations between the half-cells by selectively conducting either cations in case of a cation-exchange membrane (CEM) or anions in case of an anion-exchange membrane (AEM)[1]. An ideal separator features high ionic conductivity (which translates to low ohmic resistance), high selectivity, i.e. being non-permeable for electroactive species, high chemical, thermal and mechanical stability and low cost. Except for the cost aspect, these requirements are best met by the proton-exchange membrane (PEM) material *Nafion*, at least in aqueous RFB. Although the membrane constitutes the smallest fraction (in terms of wt.-%) of a VRFB module [14], it is responsible for up to 40% of stack cost in Nafion-based RFB systems [11, 15]. Therefore, huge efforts are put into finding a suitable replacement [16].

Further components of a typical RFB cell include the porous electrodes, flow

---

[1]Although the feasibility of membrane-less RFB has been demonstrated [13] the vast majority of RFB systems - including those operated in the context of this thesis - utilizes a membrane. Therefore, in the further discussion the presence of a membrane will be assumed.
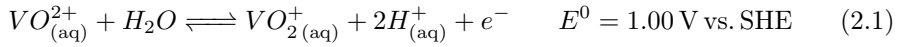
plates and current collectors which will be sandwiched between two end plates. Depending on and in accordance with the cell design, gaskets are used to certain extents in order to seal the cell (or stack) and ensure leak-free operation. Porous, mainly carbon-based, electrodes supply a large active surface area at which the respective half-cell reactions take place. They will be subject of an in-depth discussion in section 2.2. The enclosing flow plates distribute the flow of electrolyte evenly across the whole width of the electrodes. This should assure a uniform mass transport and thus avoid the emergence of significant gradients in potential or current density within the cell [17–20]. Flow plates are usually either completely made of graphitic material or feature an embedded graphite plate that presses against the electrodes, thus acting as a bipolar plate in a stack. Furthermore, they ensure electrical contact between electrodes and current collectors (typically consisting of very conductive material like Au or Cu), while preserving the latter from having contact to the electrolyte. Depending on the flow geometry, different types of electrode materials and flow plate designs are applied. A *flow-through* cell will make use of comparably thicker (several mm) electrode, typically carbon felt, and the electrolyte *flow* will have to pass *through* the whole volume of the electrodes. In this case, the flow plate usually features a flat graphite plate and some means of flow distribution at the electrolyte inlet. In *flow-by* geometry, flow channels are engraved into the bipolar plate, which enable the electrolyte *flow* to pass *by* the µm-thin (carbon paper) electrodes. Optimizing the flow in a RFB is crucial for enhancing electrolyte utilization while minimizing pressure drop. Therefore, improving geometrical aspects of electrodes and flow plates is of utmost importance in the engineering of flow cells [21–26].

While the majority of RFB types share the herein discussed principles of design and construction, the variety of utilized chemistries resembles a colorful bouquet of flowers [27, 28]. All-liquid RFBs can be categorized based on solvent as *aqueous* or *non-aqueous* and based on dissolved active species as *organic* or *inorganic*. Besides, also hybrid systems exist, like solid-liquid Zinc-Bromine or gas-liquid Vanadium-Air batteries [29]. However, unless otherwise noted, throughout this thesis the term *redox-flow battery* will refer exclusively to all-liquid systems.

Among these, the all-vanadium redox-flow battery (VRFB) has found the highest degree of commercialisation with more than 200 installations globally [30]. Furthermore, the world's largest battery electric energy storage system, rated at $100\,\mathrm{MW}$ and $400\,\mathrm{MW\,h}$ (to be doubled in the final development stage), which was brought online by Rongke Power in the chinese province Dalian in 2022,

relies solely on VRFB technology [31].

The latter has been pioneered by the group of *Skyllas-Kazacos* in the 1980's [32] and utilizes vanadium as the only active element in both half cells. This is enabled by the fact that vanadium can occupy four stable oxidation states in aqueous solution and thus eliminates the issue of cross-contamination which is a significant disadvantage of other battery chemistries. I.e., a cross-over of vanadium ions from one half cell into the other may lead to a certain extent of self-discharge but never to an irreversible capacity loss. The electrode reactions (with potentials reported with respect to standard hydrogen electrode (SHE)) are:

$$VO^{2+}_{(aq)} + H_2O \rightleftharpoons VO^+_{2\,(aq)} + 2H^+_{(aq)} + e^- \qquad E^0 = 1.00\,\text{V vs. SHE} \qquad (2.1)$$

in the positive half cell and:

$$V^{2+}_{(aq)} \rightleftharpoons V^{3+}_{(aq)} + e^- \qquad\qquad E^0 = -0.26\,\text{V vs. SHE} \qquad (2.2)$$

in the negative half cell, leading to an overall (theoretical) open-circuit potential (OCP) of $E_{oc} = 1.26\,\text{V}$ at $25\,°\text{C}$ and $50\,\%$ SOC. However, real cells will display a higher voltage of $E_{oc} \approx 1.40\,\text{V}$ under the same conditions, mainly due to the Donnan potential across the membrane [33].

Being an all-liquid RFB, no plating and re-dissolvment of active species takes place during the fundamental redox processes of a VRFB. This eliminates a severe issue characteristic for battery chemistries involving solid active phases which is the formation and growth of dendrites [34]. Further advantages of a VRFB include low self-discharge, very high depth of discharge and, as for all aqueous RFBs, the absence of fire hazard. On the other hand, significant challenges arise from the low solubility and temperature stability of V(V). Due to the former, typically achievable total vanadium concentrations range from $1.5 - 2.0\,\text{M}$, only enabled by using rather high concentrations of sulfuric acid (up to $5\,\text{M}$ total sulfate concentration) as supporting electrolyte. Applying additives such as phosphoric acid and ammonium sulfate, higher concentrations up to $3\,\text{M}$ can be stabilized [35]. This makes for a maximum theoretical energy density of around $40\,\text{W}\,\text{h}\,\text{L}^{-1}$, which is still about three times lower than in a typical Li-Ion battery [36]. Furthermore, at temperatures $T > 40\,°\text{C}$ and concentrations $c \geq 2\,\text{M}$ V(V) starts to irreversibly precipitate as V_2O_5 [37, 38]. While for V(II), V(III) and V(IV) high temperature stability is not an issue at these concentrations, they instead tend to precipitate at low temperatures of $T < 10\,°\text{C}$ [39]. The oxidative nature of V(V) combined with the necessary

high concentrations of sulfuric acid render VRFB electrolyte solutions strongly corroding media. This greatly limits the available choice of materials for membranes, electrodes, gaskets, tubing, etc. to be utilized in a VRFB system. Additionally, the usable cell voltage is limited by the stability window of water. Exceeding the later will result in parasitic side reactions induced by the electrolysis of water. Special attention has to be paid in the negative half cell, where occurence of the HER is practically not avoidable [40–44] and seemingly even enhanced by the mere presence of vanadium itself [44]. In fact, only the use of carbon-based electrodes allows for the V(III) reduction to become the dominant reaction due to the high kinetic overpotentials of the HER at carbon surfaces in acidic media [45]. Further challenges in the negative half cell are the need for an inert atmosphere, as formed V(II) is not stable in the presence of oxygen, and sluggish electrode kinetics of the V(II)/V(III) redox couple. While the former is rather straightforward to solve by keeping the negolyte tank under nitrogen or argon, the latter has been a major motivation for the present thesis and will be discussed in detail in the upcoming section 2.2. A last factor associated with vanadium is its price and the fluctuations of the same. Both have given rise to an increased research interest aimed at replacing vanadium with low cost, taylor-made organic molecules [46–51]. Although promising, still significant issues, especially concerning demonstrated energy densities and long-term stability of active species, have to be overcome in these *aqueous organic RFBs* in order to rival the VRFB system.

Benchmarking RFBs is commonly done by performing consecutive galvanostatic charge/discharge cycles which yield insights into Coulombic efficiency (CE), voltage efficiency (VE) and energy efficiency (EE) as well as the maximum achievable discharge power density (DPD) [29, 36]. In this sense, CE is defined as the ratio of the amount of charges transferred during discharge Q_{out} to the amount of charges transferred during charging Q_{in}:

$$CE = \frac{Q_{\mathrm{out}}}{Q_{\mathrm{in}}} \tag{2.3}$$

Main factors limiting CE are crossover of active species through the membrane, leading to self-discharge, as well as parasitic side reactions. VE describes the ratio of average discharging voltage $V_{\mathrm{discharge}}$ to average charging voltage V_{charge}:

$$VE = \frac{V_{\mathrm{discharge}}}{V_{\mathrm{charge}}} \tag{2.4}$$

It is impeded mainly by kinetic, Ohmic and mass-transport overpotentials. CE and VE combined yield the EE, indicating how much of the stored energy can be supplied during discharge of the battery:

$$EE = CE \cdot VE \tag{2.5}$$

In analogy to fuel cell research, occuring overpotentials are often assessed using polarization curves [29, 52, 53]. Such curve, also referred to as *i-V*-curve, is exemplarily depicted in Fig. 2.2. It shows a plot of cell voltage E_{cell} with respect
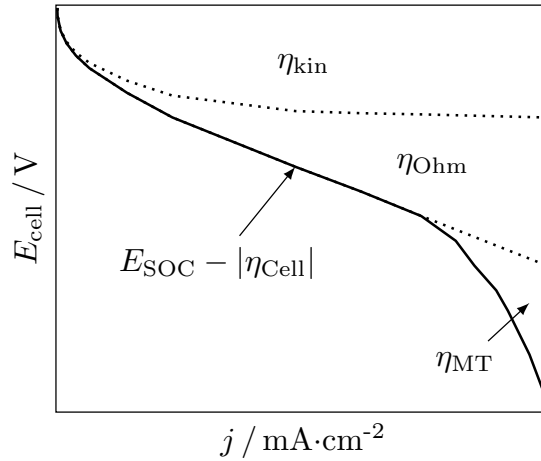

Figure 2.2: Exemplary polarization curve of a VRFB for charging and discharging at a SOC of 50%.

to current density in charging and discharging direction. The former is given as:

$$E_{\text{cell}} = E_{\text{SOC}} \pm |\eta_{\text{cell}}| \tag{2.6}$$

where E_{SOC} is the open-circuit potential (OCP) defined by the state of charge (SOC), the sign depends on the current direction ("+" for charging and "-" for discharging) and η_{cell} is the sum of all overpotentials in negative and positive half cell, η_{NHC} and η_{PHC}, respectively. The overpotentials of one half cell in turn

consist of contributions from Ohmic (η_{Ohm}), kinetic (η_{kin}) and mass transport (η_{mt}) losses. Therefore the overall overpotential of the cell is defined as:

$$|\eta_{\text{cell}}| = |\eta_{\text{NHC}}| + |\eta_{\text{PHC}}| = (|\eta_{\text{Ohm}}| + |\eta_{\text{kin}}| + |\eta_{\text{mt}}|)_{\text{NHC}} + (|\eta_{\text{Ohm}}| + |\eta_{\text{kin}}| + |\eta_{\text{mt}}|)_{\text{PHC}} \tag{2.7}$$

Each of these three sources of voltage losses are dominant at different current densities, which manifests in three distinct regions of the polarization curve. At low absolute current densities, kinetic overpotentials are most pronounced. Intermediate current densities are dominated by Ohmic losses, while mass transport overpotentials are significantly increasing at high current densities[2]. Eliminating, or at least minimizing, these overpotentials can be seen as the primary goal in the development of (V)RFB stacks and systems. This requires for detailed insights into the origins of voltage losses.

The latter are commonly functions of temperature, concentration of active species, SOC as well as density and direction (charge or discharge) of current. Mass transport losses furthermore depend on numerous factors such as geometrical arrangement of electrode fibers and electrode compression, both effecting open porosity in the electrodes, design of flow plates and flow velocity of electrolyte. While transport losses can be effectively minimized by increasing the electrolyte flow rate, this comes at the expense of a more pronounced energy consumption of the pumps, limiting overall system efficiency. The main source of Ohmic losses in VRFB is the resistance of the membrane, along with contact resistances between electrodes and bipolar plates, cabling, etc. Kinetic losses mainly result from low electrocatalytic activity of the electrodes. While a huge variety of *activating* methods have been proposed in order to minimize kinetic overpotentials, they are likely to increase with ongoing electrode degradation. The upcoming section 2.2 is devoted to comprehensively shine a light on this specific matter in the context of VRFB electrodes.

---

[2]Even though one type of overpotential may dominate a certain region, all types are present over the whole range of current densities. As a polarization curve always yields the sum of all overpotentials, resolving for individual contributions is not possible based on this type of measurement alone.

2.2 Carbon-based electrodes in VRFB

2.2.1 Kinetic aspects

When speaking of *kinetics* in an electrochemical context, one usually refers to the *Butler-Volmer (BV) model* of electrode kinetics [54, 55], which shall be very briefly introduced in the following. For a simple one-step, one-electron reaction

$$O + e \underset{k_\mathrm{b}}{\overset{k_\mathrm{f}}{\rightleftharpoons}} R \tag{2.8}$$

with rate constants k_f and k_b of forward and backward reaction, respectively, the net current i is related to the overpotential, or deviation of electrode potential from equilibrium $\eta = E - E_\mathrm{eq}$ according to:

$$i = i_0 \left[e^{\frac{-\alpha F}{RT} \eta} - e^{\frac{(1-\alpha) F}{RT} \eta} \right] \tag{2.9}$$

where i_0 is the *exchange current*, α the *transfer coefficient*, F, R and T have their usual meaning and the two exponential terms in square brackets represent cathodic and anodic current components i_c and i_a, respectively. This *historical* form of the BV equation doesn't account for potential gradients introduced by presence of a double-layer or mass transport effects. The latter implies that Eq. 2.9 is therefore only valid in a regime where overall currents are sufficiently small and the electrolyte solution is well-stirred (or -pumped) enough to assure that concentrations of active species are the same at the electrode surface and in bulk solution. Detailed derivation, implications, further discussion and more general forms of the BV model can be found elsewhere [56]. The decisive aspect of Eq. 2.9 for the ongoing discussion in this section, however, is the seemingly rather inconspicious exchange current i_0. It is defined for equilibrium conditions, where cathodic and anodic current components i_c and i_a are balanced (leading to a net current of $i = 0$) but not zero, and its magnitude is equal to either one of these components. According to

$$i_0 = F A k^0 c_\mathrm{O}^{*(1-\alpha)} c_\mathrm{R}^{*\alpha} \tag{2.10}$$

where c_O^* and c_R^* are the bulk concentrations of oxidized and reduced species, respectively, the exchange current is directly proportional to the standard rate constant k^0. The latter is in turn defined for the special case of an equilibrium in a solution where $c_\mathrm{O}^* = c_\mathrm{R}^* = c$. Under these circumstances, Eq. 2.10 further simplifies to:

$$i_0 = F A k^0 c \tag{2.11}$$

and the respective rate constants of forward and backward reaction in Eq. 2.8, k_f and k_b, exhibit the same value - k^0. This quantity is practically the essence of any discussion concerning electrode kinetics: high values are indicative of kinetically *facile* systems[3], where equilibrium will be reached rather fast, while those with low k^0 are often termed *sluggish* or kinetically hindered. In this context, *catalysis* refers to an increase in k^0. The term *degradation* on the other hand will be used throughout this thesis to describe processes that decrease k^0. Since i_0 is directly proportional to k^0, both quantities are often used synonymous in electrochemical literature. Discussing electrode kinetics in terms of *exchange current density* $j_0 = i_0/A$ is also quite common. However, a high degree of caution is adviced at this point as the area A is a rather ambiguous quantity. Generally, and especially in Eqs. 2.10 and 2.11, it refers to the electrochemically active surface area (ECSA). In contrast, current densities (including j_0) at porous electrodes are most often reported with respect to geometrical area rather than actual ECSA, as the latter is not straightforward to determine in such cases. Many studies assume the ECSA to be identical to the surface area determined by the Brunauer-Emmett-Teller (BET) method. However, this assumption seems to lack justification [57, 58], yielding unreliable results in the conversion of experimentally obtained i_0 to k^0. Also, the rather commonly utilized treatment of cyclic voltammetry (CV) data by means of the Randles-Ševčík equation is not suited for proper determination of ECSA or kinetic properties of porous electrodes [58, 59]. It is therefore not surprising that *Friedl et al.* found reported values of k^0 for the V(II)/V(III) and V(IV)/V(V) redox couples at carbon-based porous electrodes to vary over four orders of magnitude [60]. As this severely impedes a well-founded discussion about the factors affecting redox kinetics in the context of VRFB, they proposed a workaround based on normalization with respect to the double layer capacity C_{DL} obtained by EIS [58–60]. This approach is of central importance for the proper determination of kinetic properties, which, in turn, is the foundation of any assessment of catalytic activity or degradation as pursued within this thesis. It will therefore be introduced in detail in section 3.1.

Besides the apparent need for high electrochemical activity (= fast kinetics) towards the employed vanadium redox couples, an electrode material has to meet following criteria in order to be considered suitable for use in a VRFB [61]: high electrical conductivity, large active surface area, chemical and mechanical

---

[3]Herein, the term *system* refers to a certain combination of electrode, redox couple and supporting electrolyte. It is worth keeping in mind that a reasonable assessment of kinetic properties is only possible if the whole system is taken into account.

stability, low cost and high hydrophilicity (or wettability). These requirements are best fulfilled by macroporous carbons. While such materials can in principle be obtained by pyrolysis of literally any kind of biomass (e.g. coconut shell [62], orange peel [63], fungi [64], coffee beans [65], chicken bones [66], ...), the two dominant precursors in industrial production of VRFB electrodes are rayon (regenerated cellulose) and polyacrylonitrile (PAN) [67]. The elaborate preparation processes involve spinning of fibers into macroporous paper- or felt-like structures followed by several stages of stabilizing and carbonizing heat treatment [68, 69]. Carbonization is initiated by subjecting stabilized fibers to temperatures of $T > 300\,^{\circ}\mathrm{C}$ under inert atmosphere which triggers the formation of disordered (*turbostratic*) layers of graphene - the *basal planes* - by aromatization and condensation of individual polymer strains. Optional graphitization demands for temperatures of up to $3000\,^{\circ}\mathrm{C}$ and refers to the formation of the typical hexagonal crystal structure of graphite by enhanced stacking of basal planes. Crystallite size and degree of ordering (orientation along the fiber axis) were found to behave as monotonic functions of applied temperature during this stage of treatment [70]. This effect is more pronounced at or in close proximity to the surface, leading to fibers with a highly graphitized shell and comparably turbostratic core. As the individual graphene layers exhibit excellent *in-plane* conductivity, enlarged size of graphitic domains and increased long-range order associated with high degree of graphitization consequently enhances electrical conductivity κ of the finally obtained fibrous material, which is highly desirable for energy storage applications. For instance, increasing the graphitization temperature of PAN-based fibers from $1000\,^{\circ}\mathrm{C}$ to $2200\,^{\circ}\mathrm{C}$ led to a remarkable rise in κ from formerly $5.32\,\mathrm{S\,cm^{-1}}$ to $75.91\,\mathrm{S\,cm^{-1}}$.

However, electrochemical properties of carbon-based electrode materials are not only determined by graphitization degree and resulting electrical conductivity. Instead, superficial composition, i.e. the ratio of edge- or defect-sites to sites located at the basal plane and the presence of heteroatom-containing functional groups, also has to be considered a decisive factor impacting redox kinetics in many cases. For instance, edge-sites are generally known to be more reactive than basal-plane sites [71–74]. Furthermore, increasing the number of oxygen surface functionalities greatly enhance wetting of the otherwise rather hydrophobic carbon felts in VRFB [75]. The improved interpenetration of the porous fiber network with vanadium electrolyte leads to a significantly enlarged ECSA, which, in turn, causes a rise in i_0 (cf. Eq. 2.11). Besides this undisputed surface effect, several reports claimed an additional catalytic effect of oxygen-containing functional groups. Early studies assumed this effect to

benefit both half cell reactions in VRFB [76, 77]. Consequently, a lot of following research has been focused on increasing the number of oxygen functionalities by subjecting carbon-based electrodes to treatment routines like thermal [76, 78] or electrochemical [79–81] surface oxidation, acidic [77, 82, 83] or alkaline [84–86] etching or plasma treatment [87, 88]. Introduction of heteroatoms different than oxygen, i.e. by surface halogenation [89] or nitrogen doping [90, 91] has also been suggested for electrode activation in VRFB. However, the following discussion shall be limited to the effects of oxygen-containing functional group since these are most comprehensively assessed in the recent literature.

In contrast to the aforementioned assumptions made in the early studies by *Sun et al.* [76, 77], a catalytic effect of oxygen groups could only be verified for the V(II)/V(III) redox couple [58, 67, 92–95]. That means electrode kinetic in the negative half cell of a VRFB is highly sensitive to the presence (or absence) of surface functional groups, or surface composition in general, while the positive half cell reaction seems to depend more strongly on graphitization degree, and therefore electrical conductivity, of the electrode [58, 67, 95]. Furthermore, excess of oxygen functionalities was found to actually inhibit kinetics of the V(IV)/V(V) couple [58, 79–81, 88]. Based on these findings, *Miller, Buckley et al.* [81, 96] stated that during operation of a VRFB the applied potential window in the negative half cell would lead to reduction of oxygen groups at the electrode surface, inducing deactivation towards the V(II)/V(III) redox couple while at the same time activating it with respect to the V(IV)/V(V) couple. On the other hand, the potential window in the positive half cell will have the opposite effect. Consequently, they were able to partially restore performance losses observed after cycling by simply reversing the cell voltage (thus interchanging positive and negative half cell).

It is worth to note that these conclusions are not universally accepted. Instead, numerous studies claimed a catalytic effect of oxygen functionalities also for the positive half cell reaction [82, 86, 97–100]. Similarly, some authors assume the overall cell performance to be limited by the latter [101, 102], whereas many others identified the negative half cell electrode to be the performance-limiting[4] one [103–107]. Besides the already mentioned improper use of electrochemical methods (cf. page 13), lack of differentiation of surface effects from inherent catalytic effects and the influence of pretreatments discussed herein, these con-

---

[4]In fact, and as discussed in the previous section (2.1), cell performance is actually limited by the sum of all (Ohmic, kinetic, mass transport) overpotentials. The term *perfomance-limiting electrode* is therefore a rather imprecise phrasing which is, nonetheless, frequently used in VRFB literature to refer to the major source of kinetic overpotential in the cell.

tradictory results might further be due to electrolyte properties that are often overlooked or neglected when discussing electrode kinetics in VRFB. First, the type of anion(s) present in the electrolyte might severly impact both half cell reactions [108, 109]. Second, even trace amounts of metallic impurities are able to significantly alter the redox behaviour of a carbon surface [110, 111]. Despite the presence of such impurities being practically inevitable in commercial VRFB electrolytes, they are rarely quantified, let alone assessed in terms of how they affect vanadium redox kinetics [112]. Finally, the concentration of vanadium itself seems to play a decisive role. In a recent review article, *Roznyatovskaya et al.* found that reported values of k^0 are very similar for both half cell reactions when total vanadium concentrations were kept below 0.1 M [113]. However, at practical concentrations above 1 M, there is a tendency that reducing a carbon surface decreases its kinetic activity towards the negative half cell reaction while kinetics of the positive half cell reaction is enhanced. This tendency is reversed for oxidized carbon surfaces. This means, that for a pristine carbon electrode under realistic operating conditions of a VRFB $k^0_{V(II)/V(III)} < k^0_{V(IV)/V(V)}$, thus the performance-limiting electrode would be that of the negative half cell. Consequently, best cell performance can be expected for unsymmetric cells featuring a pristine electrode in the positive and an oxidized electrode in the negative half cell.

2.2.2 Metal-based electrocatalysts

Further improvements of electrode kinetics in VRFB can be achieved by decoration of carbon fibers with electrocatalytically active moieties like metal or metal oxide (nano)particles. Pioneering studies conducted within the research group of *Skyllas-Kazacos* identified Ir as the most promising among a variety of candidates, while Mn, Te and In yielded encouraging results as well [114]. However, scarcity of iridium and the resulting high costs impeded the widespread implementation of iridium-based electrocatalysts in VRFB. Other metals like Pt, Pd or Au had been dismissed very early on due to their high tendency to catalyze parasitic side reactions such as HER rather than the envisaged conversion reactions of vanadium. Ever since, myriads of researchers have studied an evergrowing variety of metal-based electrocatalysts, resulting in an accumulated list of proposed options which reads like a broad sweep through nearly the entire periodic table of elements [115, 116].

In recent years, Bi has drawn a considerable amount of attention, particularly due to its low cost and toxicity as well as high HER overpotential (compared to

the aforementioned noble metals). Following an initial study by *Gonzalez et al.* [102], metallic or oxidic Bi particles have been deposited onto carbon fibers using *ex-situ* wet chemical impregnation [102, 117, 118] or electrodeposition [119] methods or incorporated into the fibers via electrospinning [120]. Furthermore, *Li et al.* have used bismuth salts as an electrolyte additive to *in-situ* electrodeposit Bi particles onto a graphite felt electrode during charging of the VRFB [121]. Irrespective of the preparative approach, bismuth particles will adopt a state of Bi^0 when subjected to the potential window of a VRFB's negative half cell during charging and discharging [122] and increase the perceived rate of the V(II)/V(III) redox reaction. Some authors claimed that bismuth was able to suppress the HER at carbon-based electrodes and proposed reaction mechanisms involving the formation of non-stochiometric bismuth hydrides BiH_x [118, 119]. Even though these mechanisms might be based on reasonable assumptions, no experimental evidence (or theoretical calculation) in support of their validity has been presented so far. Moreover, the commonly presented CV curves of Bi-modified electrodes are not sufficient to proof the HER-inhibiting qualities of bismuth. To do so, further efforts are needed, e.g. to quantify evolution of gaseous byproducts during operation of an VRFB or to deconvolve CV response of modified and unmodified electrodes in order to assess which fraction of the observed overall current can be attributed to the HER reaction in each case.

While the modification of carbon-based electrodes with bismuth undoubtedly enhances the perceived electrode performance in the negative half cell, it remains unclear wether this enhancement is due to intrinsic catalytic activity of Bi or rather the result of an increased ECSA caused by a more hydrophilic character of the modified electrode. Apparently, this question has not yet been adressed in the VRFB literature, which appears to be the case not only for bismuth but rather generally for all types of proposed metal (oxide) catalysts [115, 123]. This is at least surprising since contact angle measurements have, in numerous cases, demonstrated that the presence of metal or metal oxide particles significantly increases the wettability of carbon-based electrodes [124–127]. Even though this fact is occasionally acknowledged, it is hardly ever taken into account when discussing electrochemical measurement results. It is therefore impossible to reasonably benchmark the different types of proposed electrocatalysts with respect to their intrinsic electrocatalytic activity. The result is a paradox situation in which the evergrowing number of studies proposing ever new variations of metal-based electrocatalysts does not contribute any substantial advancements to the field of electrocatalysis research in the context of VRFB.

Furthermore, available literature shows a certain repetitiveness in that new approaches for incorporating metal-based electrocatalysts, once proposed, will be outright duplicated except for the type of utilized metal. As an example, the previously mentioned addition of metal salts to the electrolyte followed by *in-situ* electrodeposition of metal particles on the electrode during charging of the battery has so far at least been conducted with salts of Bi[121], Mo[128], Sb[129] and W[130]. While this approach has been reported to initially benefit energy efficiency of the VRFB in all cases, no data is available on the long-term stability of electrodes modified this way.

2.2.3   Degradation

Generally and in contrast to PEM fuel cells, where degradation of catalyst particles and possible consequential damages of other components (e.g. membrane, carbon support) are widely studied topics[131–133], durability of metal-based electrocatalysts appears to be another issue that has so far been neglected within VRFB research.

Overall, ageing and degradation processes in VRFB (especially those related to electrodes) have only recently come into focus and related literature remains rather scarce. In addition, the majority of the studies published so far have been limited to the investigation of partial aspects, without taking into account the interactions of different ageing mechanisms within an operating system. Only one review article is currently available on ageing at the cell and material level[134], while *Wittmann et al.* emphasized the urgent need for further ageing studies for all types of RFB[34].

Degradation phenomena in VRFB can be symptomatically classified into those leading to capacity loss and those leading to increased cell impedance. Capacity loss typically refers to a decrease in Coulombic efficiency and thus a loss of accessible energy storage capacity of the battery. Reasons for this include side reactions occurring at very high SOC such as evolution of hydrogen from the aqueous electrolyte in the negative half cell[40–44], cross-diffusion of active species or other electrolyte constituents (such as sulphate ions or water), which lead to an imbalance of vanadium concentrations in the two half-cells[135] or precipitation of V(V) oxides from the electrolyte of the positive half-cell at temperatures $T > 40\,^{\circ}\mathrm{C}$[37, 38]. Furthermore, elevated cell impedance may arise from increased contact resistances between electrodes and bipolar plates (either due to the onset of C-corrosion on the bipolar plate and/or electrode or mechanical fatigue of the latter)[136, 137], raised Ohmic resistance induced by

electrolyte precipitation within the membrane or additional overvoltages due to electrolyte shift or passivation of the electrodes [138]. It is worth pointing out the synergies between the different modes of degradation, i.e. in an operating VRFB all of the stated processes will occur concurrently and possibly enhance (or be enhanced by) one another.

Previous studies on electrode ageing in VRFB can be divided into *ex-situ* and *in-situ* investigations based on the experimental approach followed. Herein, the term *ex-situ* refers to the comprehensive physico-chemical characterisation of electrodes after storage in ageing-inducing media (such as concentrated acid, VRFB electrolyte with a high state of charge, potentially with addition of specific impurities), polarisation in sulphuric acid (in the absence of vanadium) or operation in a battery cell (*post-mortem analysis*). Frequently utilized analytical techniques include CV and EIS in a 3-electrode arrangement, spectroscopic methods such as Raman spectroscopy, X-ray photoelectron spectroscopy (XPS) or near-edge X-ray absorption fine structure spectroscopy (NEXAFS), electron microscopy like scanning electron microscopy (SEM) or transmission electron microscopy (TEM) and X-ray computed tomography (CT) [29]. Furthermore, coupling of a 3-electrode setup with a mass spectrometer enables the potential-dependent quantification of degradation products (H_2, CO, CO_2) [139, 140]. In line with the previously discussed correlation between V^{2+}/ V^{3+} redox kinetics and the presence of oxygen containing funtional groups on the electrode surface, *post-mortem* XPS analysis revealed the decrease of electrode activity in the negative half-cell to be accompanied by a loss of superficial O-functionalities [141]. Similar studies found the VO^{2+}/ VO_2^+ pair to be rather unaffected by such changes in surface composition. Instead, the sp^2/sp^3 ratio and consequently the associated electrical conductivity within the carbon fibers has been identified as a critical factor for the electrode kinetics in the positive half-cell [67, 142].

Determining the electrodes' state of health *in-situ* or *in-operando* by means of optical or spectroscopic methods, which are commonly employed in the characterization of electrolyte solutions [134], is hardly feasible due to the strong absorption of the latter. Therefore, electrochemical techniques are used almost exclusively in this context. Probably the most common approach is to subject a VRFB cell to galvanostatic cycling (repeated charging and discharging), possibly with variation of current density or cut-off voltage, followed by characterization using polarization curve or EIS measurements [107, 141, 143]. Raising the cut-off voltage during charging extends the range of accessible SOC. Higher SOC in turn increases the likelihood for parasitic side reactions to occur. Gaseous products thereby evolved have been quantified e.g. by incorporating a hydrogen sensor

19

into the headspace of the negolyte tank [42]. While gas evolution is primarily considered a mode of electrolyte decomposition, its significance for the degradation of electrodes can't be overstated. For instance, *Liu et al.* found that the onset of oxygen evolution from the aqeous electrolyte lies at potentials far more anodic than that of carbon corrosion. This implies that the main products of gas evolution in the positive half cell during operation of a VRFB are CO and CO_2, originating from the degradation of the carbon electrode. Although not initially critical to electrode kinetics of the V(IV)/V(V) redox reaction, prolonged carbon corrosion might impair the mechanical strength of electrode fibers, leading to an increased Ohmic resistance and therefore ultimately inducing a capacity loss in the long term. On the other hand, hydrogen evolution reaction (HER) has been found to qualitatively correlate with passivation of the negative half cell electrode towards the V(II)/V(III) redox reaction [42, 43, 80, 81, 143, 144]. Functional groups like C-OH or C-O-C are often assumed to be mechanistically involved in the evolution of hydrogen, thus being reduced during the process. Consequently, HER could be termed a "self-amplifying" phenomenon since the loss of active sites for vanadium reduction, supposedly caused by the formation of hydrogen, would further enhance the latter (at least if the battery cell is to be run at a constant current density). However, it might as well be argued that electrode passivation and HER be independent processes that only occur in conjunction since both are induced by the same reducing conditions. Both of these two lines of argument have neither been verified nor disproven as of yet. In addition, no quantitative correlation between gas evolution and electrode state of health could be established so far.

Further challenges associated with the *in-situ* investigation of electrode degradation in VRFB involve the discrimination of different degradation processes as well as the distinct study of the individual half cell electrodes. Changes in energy efficiency or maximum achievable storage capacity observed during cycling always represent the sum of all ageing phenomena occuring within the battery cell. Polarization curves may offer additional insights, e.g. with respect to increased kinetic overpotentials that relate to electrode degradation. However, those overpotentials again constitute the sum of overpotentials in both half cells. For this reason, reference electrodes [104, 105, 145] and pseudo-reference electrodes [78, 146, 147] have been succesfully incorporated into full cell setups in order to unravel the individual half cell contributions. Despite yielding valuable insights in lab scale experiments, such modifications further complicate the already complex VRFB test setup and might introduce additional challenges such as higher Ohmic resistance, increased risk of leakage or contamination

with foreign ions. The prospects of adopting these approaches to idustrial ($\geq$ kW-scale cell stack) applications are therefore rather limited.

In principle, making use of EIS could serve the same cause, given that a suitable equivalent circuit model (ECM) is at hand. As this has been a major objective of the present thesis, the following chapter will familiarize the reader with the basic principles of EIS and subsequently discuss how this experimental technique can be utilized to deduce half cell-specific information from full cell impedance spectra of a VRFB without the need for cumbersome setup modifications.

2.3 Electrochemical impedance spectroscopy and the distribution of relaxation times

2.3.1 Short introduction to EIS

Figure 2.3: Comparison of (left) polarization curve with individual voltage losses and (right) impedance spectrum with correlating types of resistance.

Electrochemical impedance spectroscopy (EIS) is a non-invasive analytical technique with widespread application in characterization of e.g. corrosion processes, semiconductors, metallic paints, insulating coatings, lubricants and electrochemical power sources like fuel cells and batteries [133, 148–153]. It can be seen as (one of) the prevalent electrochemical characterization method(s) in Li-Ion battery research, where is has been extensively used to study kinetics of charge-transfer [154–157] and ion transport [158–161], estimate state of charge (SOC) [162–166], state of health (SOH) [167–169] and internal cell temperature [170–175] or to assess the effects of e.g. cell design [176] or electrolyte composition [177–179] on battery performance. By monitoring the evolution of cell impedance over time or through different operating conditions, valuable insights in aging and degradation mechanisms can be gained for Li-Ion batteries [180–185], fuel cells [186, 187] or vanadium redox-flow batteries (VRFBs) [107, 146, 188, 189]. In VRFB research, EIS has found broad usage as an *ex-situ* technique (conducted in a three-electrode setup), especially for determining charge-transfer kinetics of carbon-based electrodes [58, 59]. It

has proven to be very useful in characterizing and comparing the effects of pre-treatment procedures [79–81, 87, 96], addition of electrocatalysts [117, 127, 129, 190] or different aging routines [191, 192]. Apart from these more material-science focused *ex-situ* applications, RFB engineering also greatly benefits from *in-situ* EIS, which enables the investigation of design aspects from the single-cell [26, 188, 193, 194] up to the large-scale stack level [195, 196].

The great advantage of EIS, besides its flexible applicability, is that it allows for a distinction of several processes based on their characteristic frequencies. A polarization curve on the other hand can only yield the overall differential impedance (a superposition of all contributing processes) as the local slope at a given working point. However, especially in the presence of diffusional limitations, the system response at low frequencies might become unstable which severly complicates the determination of the overall impedance $\lim_{f \to 0} Z$ by EIS. Therefore, it is good practice to use both techniques in conjunction. The correlation between EIS and polarization curve measurements is further illustrated in Fig. 2.3.

In a typical EIS experiment, a small amplitude sinusoidal perturbation is imposed on the system under study and the subsequent system response is recorded. Several repetitions will be performed in order to cover a wide range of logarithmically equispaced frequencies. The input signal S_{in} is characterized by it's amplitude $\hat{S}_{in}$ and angular frequency $\omega = 2\pi f$:

$$S_{in}(t) = \hat{S}_{in} \cdot \sin(\omega t) \tag{2.12}$$

The corresponding output is additionally governed by a phase shift φ:

$$S_{out}(t) = \hat{S}_{out} \cdot \sin(\omega t + \varphi(\omega)) \tag{2.13}$$

Under potentiostatic control mode, input and output quantity are voltage $V(t)$ and current $I(t)$, respectively and vice versa for (pseudo) galvanostatic mode. By applying the Fourier transform

$$\mathfrak{F}[f(t)](\omega) = \tilde{f}(\omega) = \frac{1}{\sqrt{2\pi}} \int_{-\infty}^{+\infty} f(t)e^{-i\omega t} \, dt \tag{2.14}$$

to both quantities, the impedance in the frequency domain is obtained as:

$$Z(\omega) = \frac{\tilde{V}(\omega)}{\tilde{I}(\omega)} = |Z|e^{i\omega\varphi} \tag{2.15}$$

with $|Z|$ being the magnitude, or modulus, of the impedance and $i = \sqrt{-1}$ being the imaginary unit. Having defined impedance as the transfer function of voltage and current in the way outlined above, it is noteworthy that by applying this concept to other input and output quantities, a large variety of different transfer functions can be defined in a similar fashion [197].

From Euler's formula $e^{ix} = \cos(x) + i \cdot \sin(x)$ it is obvious, that Z is a complex quantity consisting of a real part $Re(Z) \equiv Z'$ and an imaginary part $Im(Z) \equiv Z''$ according to:

$$Z(\omega) = Z' + iZ'' = |Z|\cos(\omega\varphi) + i|Z|\sin(\omega\varphi) \tag{2.16}$$

which further leads to:

$$|Z| = \sqrt{(Z')^2 + (Z'')^2} \tag{2.17}$$

as well as:

$$\varphi = \tan^{-1}\left(\frac{Z''}{Z'}\right) \tag{2.18}$$

These relationships are further illustrated in Fig. 2.4. Depicting impedance in the complex plane like shown in Fig. 2.4 is one of the two most commonly used visual representations, often referred to as Nyquist plot. This form of presentation is especially popular in battery and fuel cell research, while the so-called Bode plot is predominantly used in corrosion studies. Both representations complement each other, since the Bode plot relates modulus $|Z|$ and phase shift φ to frequency. While no information about the latter can be withdrawn from a Nyquist plot, the ratio of Z' to Z'' can not be directly obtained from a Bode plot. Fig. 2.5 contrasts both approaches to plotting
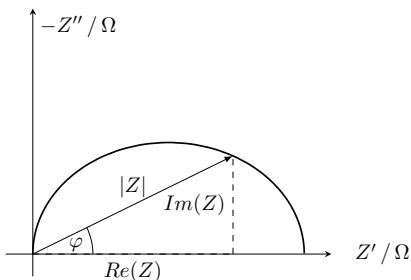

Figure 2.4: Vector representation of impedance in the complex plane with the typical semicircular shape obtained for the impedance plot of an *(RC)-* circuit.

EIS data. It also hints at the central aspect of evaluation and interpretation of EIS: the use of equivalent circuit models (ECMs).

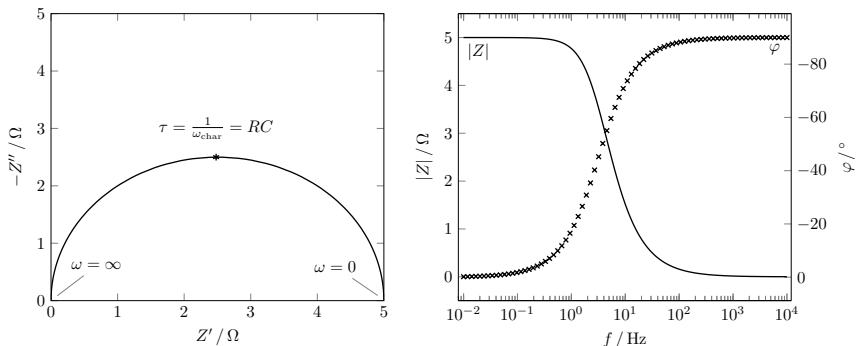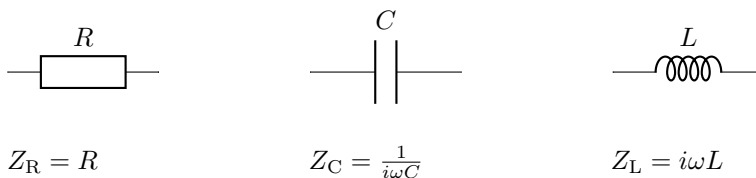Classically, system-specific characteristic parameters are obtained by fitting

Figure 2.5: Typical graphical representation of EIS: Nyquist (left) and Bode (right) plot of data simulated for an *(RC)*-circuit with $R = 5\,\Omega$ and $C = 0.01\,\mathrm{F}$.

these models to experimental data via complex non-linear least-squares (CNLS) minimization. The three most basic elements used to form an equivalent circuit are resistor R, capacitor C and inductor L. As can be seen from Table 2.1, the

Table 2.1: Common depiction and associated impedance of basic circuit elements resistor R, capacitor C and inductor L.

$Z_\mathrm{R} = R$	$Z_\mathrm{C} = \frac{1}{i\omega C}$	$Z_\mathrm{L} = i\omega L$

impedance Z_R of a resistor is simply equal to its resistance value. It is therefore frequency-independent and purely real-valued, as $Z_\mathrm{R}'' = 0$. On the other hand, Z_C and Z_L are purely imaginary and indirectly or directly, respectively, proportional to the angular frequency. Since impedance of electrochemical systems can be expressed in terms of arbitrary combinations of these three circuit elements [198–200], it is usually found in the first and fourth quadrant, as illustrated in Fig. 2.6. Although some cases of negative resistances have been reported [201–203], electrochemical impedances occuring in the second and third
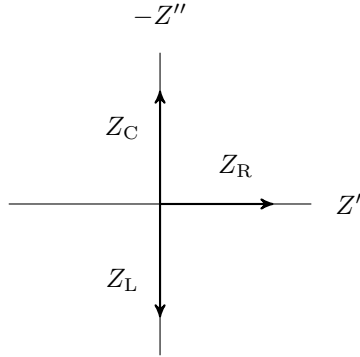
Figure 2.6: Directions of purely capacitive, resistive and inductive impedance vectors Z_C, Z_R and Z_L in the complex plane.

quadrant are a rather rarely observed phenomenon.

To form an equivalent circuit model, circuit elements can be connected either in series or in parallel. From Kirchhoff's rules it follows that for two elements connected in series, the combined impedance Z_{ser} is obtained as

$$Z_{ser} = Z_1 + Z_2 \tag{2.19}$$

where Z_1 and Z_2 are the impedance of the first and second element. Consequently, in case of a parallel connection, the combined impedance Z_{par} is given as

$$\frac{1}{Z_{par}} = \frac{1}{Z_1} + \frac{1}{Z_2} = \frac{Z_1 + Z_2}{Z_1 Z_2} \tag{2.20}$$

Unambiguous description of circuit models is possible using a simple notation introduced by Boukamp in the 1980's [204]. Connecting elements in series is implied by simply stringing together their according symbols, while the use of brackets implies a change from serial to parallel connection (and back to serial for the next respective bracket and so forth). So for instance, connecting a resistor and a capacitor in series would be denoted *RC* while *(RC)* indicates a parallel circuit.

Using this notation, the circuit in Fig. 2.7 is given by $R_{sol}(C_{dl}(R_{ct}Z_{diff}))$. It is also referred to as Randles circuit and describes the impedance of a faradaic reaction in the presence of (diffusional) mass transfer [149, 150]. Considering an electrochemical cell with three electrodes - working (WE), counter (CE)
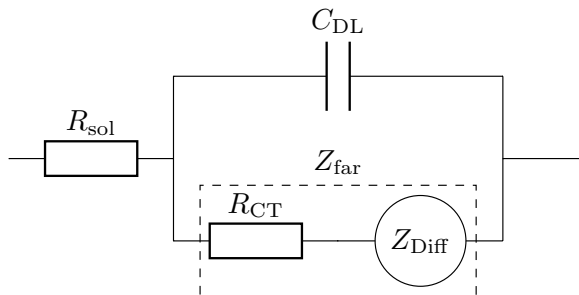
Figure 2.7: Randles circuit describing an interfacial electrochemical reaction with diffusion and double layer components.

and reference (RE) electrode - in a solution that contains active species as well as supporting electrolyte, R_{sol} represents the ohmic resistance of the bulk solution between WE and RE, C_{dl} is the double layer capacitance of the WE, R_{ct} the charge-transfer resistance and Z_{diff} the diffusional impedance, also called Warburg impedance. The latter two combined form the impedance of the faradaic reaction Z_{far}. The physical origin of this circuit can be explained as follows. R_{sol} is the resistance the ions in bulk solution are opposing towards being migrated through the external electrical field. Since this resistance has to be overcome in any case to enable a flux of charge carriers in the electrolyte, it is connected in series to the remaining circuit elements. At the electrode/electrolyte interface, a crossover from ionic to electronic charge transport occurs, which is accompanied by an electrochemical reaction in the nm-thick Helmholtz layer directly adjacent to the electrode. Therefore, an energy barrier has to be overcome that is determined by the electrochemical properties of the active species, e.g. their susceptibility to take up or release electrons at a given potential. This barrier is represented by the charge-transfer resistance R_{ct}. Consequently, R_{ct} is closely related to the exchange-current density j_0, according to:

$$R_{CT} = \frac{RT}{nFj_0 A_{wet}} \tag{2.21}$$

with gas constant R, temperature T, number of transferred electrons n, Faraday

constant F and wetted electrode area A_{wet}, which is synonymous with the ECSA. Since j_0 is in turn directly proportional to the kinetic constant k^0, R_{ct} can be seen as a direct measure of electrode kinetic properties. Consumption of active species throughout the interfacial redox reaction leads to depletion of said species and excess of reaction products at the electrode. The resulting concentration gradient is compensated by diffusion to or from the bulk solution in a thick diffusion layer. As this process is a direct result of the interfacial charge-transfer reaction with the same species being involved, the complex diffusional impedance Z_{diff} is connected in series to R_{ct}. C_{dl} arises from charged species not taking part in the electrode reaction. While they are still drawn towards the electrode, their charge is balanced by charges of opposite sign, leading to the formation of an electrochemical double layer in close proximity to the electrode. Since the forming ions are different from the reacting and diffusing species, charging of the double layer can be seen as a parallel path of energy storage. The double layer capacitance C_{dl} is therefore connected in parallel to the faradaic impedance Z_{far} and can be expressed as:

$$C_{\text{DL}} = \epsilon_r \epsilon_0 \frac{A_{\text{wet}}}{d_{\text{DL}}} \tag{2.22}$$

with relative dielectric permeability ϵ_r, permittivity of free space ϵ_0 and double layer thickness d_{DL}. Both R_{ct} and C_{dl} are important metrics in the assessment of electrode degradation. While a decreased C_{dl} hints at a loss of ECSA (e.g. due to a reduced number of functional surface groups), an increased R_{ct} indicates a decline in intrinsic electrode kinetics. Since both quantities are, besides the obvious dependencies stated in equations 2.21 and 2.22, functions of electrode potential, it is extremely important to assure consistent experimental conditions in order to compare results between different series of measurements. In case of non-planar and/or hydrophobic electrode materials, like the carbon felts utilized in VRFB, comparison of various materials (or stages of degradation) is futher complicated since A_{wet} is both unknown and experimentally not directly accessible. However, this challenge can be circumvented by using a normalization method [59, 60], which will be discussed in more detail in section 4.1.

In order for EIS to yield reliable results, the three basic conditions of linearity, causality and stationarity have to be fulfilled, as will be briefly discussed in the following.

By definition, the linearity criterion is met if the response of a system to a stimulus of a given frequency does not contain any contributions from higher harmonic frequencies. That is, the system output takes the form of equation 2.13.

However, real (and especially electrochemical) systems tend to show highly non-linear behaviour. Consequently, system output can be stated in the more general form of a Fourier series:

$$S_{\text{out}}(t) = \hat{S}_{\text{out},0} \cdot \sin(\omega t + \varphi_0(\omega)) + \hat{S}_{\text{out},1} \cdot \sin(\omega t + \varphi_1(\omega))$$

$$+ ... + \hat{S}_{\text{out},N} \cdot \sin(\omega t + \varphi_n(\omega)) = \sum_{n=0}^{N} \hat{S}_{\text{out},n} \cdot \sin(\omega t + \varphi_n(\omega)) \tag{2.23}$$

Only if the contributions of all terms with $n \geq 1$ are neglectable, equation 2.23 condenses into equation 2.13 and the system output is regarded as linear. This is presumably the case if the voltage amplitude $\hat{E}$ is kept below $10\,\text{mV}$, regardless of which type of excitation (potentiostatic or galvanostatic) is used. Experimentally, this can be verified in a straightforward manner by running a series of measurements with decreasing $\hat{S}_{\text{in}}$ until the obtained spectra become independent of the excitation amplitude.

Causality means that the system output strictly has to be a function of the input signal, i.e. $\hat{S}_{\text{out}} = 0$ for $t \leq 0$ and sole cause for a system response is the applied perturbation. The term stationarity refers to the consistency of equilibrium conditions during experimental data acquisition, implying that no apparent time-drift in SOC and therefore OCP occurs and degradation is negligible on the experimental time-scale. Fulfillment of this criterion can be easily verified by running repetitive measurements with identical parameters and checking spectral consistency.

Additionally, it is good practice to assess data quality by examining compliance of measured data with the so-called Kramers-Kronig relations [205–208]:

$$Z''(\omega) = -\frac{2\omega}{\pi} \int_0^{\infty} \frac{Z'(x) - Z'(\omega)}{x^2 - \omega^2} \, \mathrm{d}x \tag{2.24}$$

$$Z'(\omega) = Z'(\infty) + \frac{2\omega}{\pi} \int_0^{\infty} \frac{x Z''(x) - \omega Z''(\omega)}{x^2 - \omega^2} \, \mathrm{d}x \tag{2.25}$$

These transforms enable calculating the real part of the impedance from the imaginary part and vice versa. However, direct evaluation of equations 2.24 and 2.25 is impractical, as it requires the measured frequency range to be extended to infinity, which is experimentally impossible. This issue can be

circumvented by using the linear KK transform, which was first introduced by *Boukamp* [209] and later refined by *Schönleber et al.* [210]. Underlying idea of this aproach is that if a data set can, within a certain range of error (usually around 1 %), be approximated by a KK-transformable equivalent circuit, it must also be KK-transformable and therefore meet the above stated criteria of linearity, causality and stability. A so-called Voigt network, made up by a serial connection of a large number of parallel (RC)-circuits, is used as generalized circuit able to mimic impedance response of any electrochemical system, given that the number of RC-elements is sufficiently high [198, 199]. The network impedance may be expressed as:

$$Z_{\text{Voigt}}(\omega) = \sum_{n=1}^{N} \frac{R_n}{1 + i\omega R_n C_n} \tag{2.26}$$

Linearization of the fitting problem is achieved by providing a pre-defined set of time constants $\tau_n = R_n C_n$, leaving only R_n as unknown parameters. Once these are obtained by fitting equation 2.26 to either real or imaginary part of the measured impedance, the respective other part can be calculated. By inspecting the residuals between measured and calculated values with respect to the frequency, systematic errors can be identified and the corresponding data points (or frequency regions) expelled from further evaluation. This is illustrated in Fig. 2.8. It shows residuals obtained for the impedance of a single-cell VRFB, measured once at OCP and once with a significant discharging bias. In the first case, deviations between measured and calculated data points are well below 1 % over the whole experimental frequency range, although a systematic increase is observed in the high frequency regime ($\geq 1 \times 10^5$ Hz). This is due to non-linearities introduced by the measurement electronics and cable inductances. The latter is usually more pronounced for low-impedance systems like batteries and practically unavoidable (to a certain extent). In presence of a discharging bias, residuals are consistently higher, especially for the imaginary part. Additionally, errors systematically increase in the lower frequency region since the applied bias leads to a considerable discharge of the battery during the experiment. This change in SOC violates the stability criterion which is reflected in the error structure revealed by the linear KK test. If this data set was to be further evaluated at all, data points below 10 Hz and above 1×10^4 Hz should be excluded.

However, repeating the experiment while taking measures to stabilize the system is highly advisable in such a case. This can, for instance, be achieved through
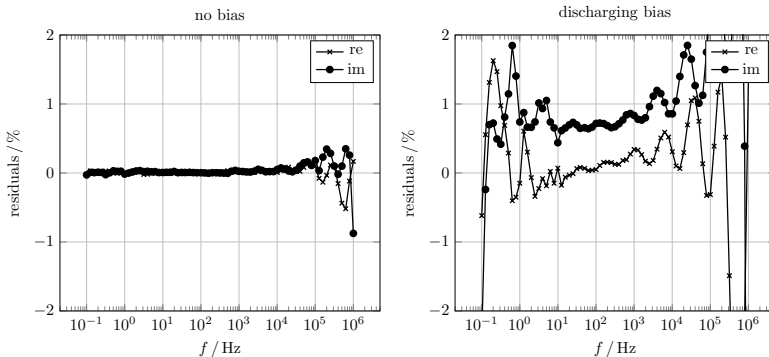
Figure 2.8: Exemplary result of linear KK testing: residuals obtained between
measured and calculated values of real and imaginary impedance of a single-cell
VRFB operated once at OCP (no bias, left) and once at a significant discharging
bias (right).

significant reduction of experimental duration by modifying the input signal.
When replacing the "classical" sweep of single-sine excitations with discrete
multi-sine signals [201, 211–213] or using different waveforms like rectangular
steps or pulses [214–218], system response to several different frequencies can
be recorded simultaneously. The resulting savings in acquisition time effectively
reduce system drift during the experiment and thus greatly enhance stability
especially in the low-frequency range. On the other hand, mathematical theory
behind these approaches is more challenging and evaluation of obtained data
sets might be computationally more demanding when compared to "classical"
EIS. Also, the initial issue of unstable SOC caused by running experiments with
significant bias is not tackled by such (more "theoretically focused") approaches.
Luckily, especially for RFB it can be overcome in a rather straightforward
way. In principle, there are three modifications to a RFB setup that are easy
to implement for lab-scale experiments and allow to conduct electrochemical
measurements under constant SOC [29]: the single-pass experiment [219], the
cell-in-series setup [220] and the symmetric cell operation [221], sometimes also
denoted as double half-cell configuration. These approaches will be discussed in
detail in section 3.2.

2.3.2 The distribution of relaxation times in EIS

One fundamental issue of using and evaluating EIS the way discussed in the previous section is the necessity of finding a physically meaningful ECM able to faithfully replicate experimental EIS data. This requires for a profound knowledge of all electrochemical processes occurring in the system under study, which might not always be available beforehand, especially when dealing with emerging technologies like VRFB. Furthermore, validating a postulated ECM is complicated by the inherent ambiguity of EIS, meaning that different models might fit the same data set equally well [148, 149]. In such cases, it is nearly impossible to decide which model describes the physicochemical circumstances the most realistically without the use of complementary characterization techniques.

Regarding the electrochemical characterization of electrode materials in VRFB, which is often performed ex-situ (using a 3-electrode setup and diluted electrolytes), the previously discussed Randles circuit (Fig. 2.7) has been employed with great success to model experimentally gathered EIS data [58, 59, 87, 107, 117, 127, 145, 191, 222]. Although the diffusional impedance might sometimes be neglected and a few pitfalls exist, which will be discussed in section 3.1, this ECM can be regarded suitable to both sufficiently describe experimental data and at the same time adequately represent the physical reality.

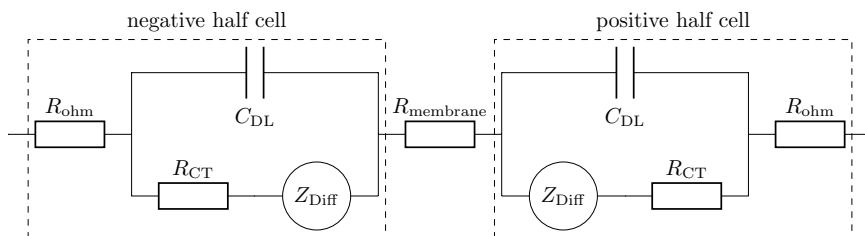As the Randles circuit is an appropriate choice to model ex-situ half-cell mea-

Figure 2.9: Hypothetical circuit model to represent full-cell impedance data.

surements, it seems reasonable to combine two such circuits in order to describe cell impedance in case of in-situ full-cell experiments. Fig. 2.9 displays the resulting circuit model consisting of one Randles circuit for each respective

half-cell, connected via the ohmic resistance of the membrane R_{membrane}. While the ohmic contributions of both half cells and the membrane will indistinguishly collapse into one overall ohmic resistance, this ECM would still enable extracting and separating information on the two half-cell reactions, given that their respective kinetic and diffusional time constants are differing enough to be discriminated. Unfortunately, in VRFB this requirement seems to be unfulfilled and thus any attempts of CNLS fitting using the ECM in Fig. 2.9 fail. Instead, oftentimes a modified Randles circuit is used, where the capacitor is exchanged for a so-called constant phase element (CPE) [188]. The CPE can be interpreted as a non-ideal, or leaking, capacitor with its impedance defined as:

$$Z_{\text{CPE}} = \frac{1}{Q(i\omega)^\phi} \tag{2.27}$$

with Q corresponding to the electrode capacitance ($\text{F\,s}^{\phi-1}\,\text{cm}^{-2}$), $0 < \phi \leq 1$ and $Z_{\text{CPE}} = Z_{\text{C}}$ for $\phi = 1$. It was introduced to account for deviations of the double-layer capacitance from purely capacitive behaviour, which are often observed at solid electrodes [148, 149]. The resulting frequency dispersion of impedances can, in analogy to the complex dielectric constant [223], be described by:

$$\frac{Z(\omega) - Z_\infty}{Z_0 - Z_\infty} = \int_0^{+\infty} \frac{G(\tau)}{1 + i\omega\tau}\,\mathrm{d}\tau \tag{2.28}$$

with $Z_\infty = \lim_{f \to \infty} Z$ and $Z_0 = \lim_{f \to 0} Z$, time constant $\tau = \omega^{-1}$ and the distribution of relaxation times (DRT) $G(\tau)$. An in-depth discussion of the physical origins of CPE behaviour is beyond the scope of this thesis, but can be found in the very recommendable text book by *Lasia* [149]. In brief, it can be ascribed to either a dispersion of time constants $\tau = R_{\text{sol}}C_{\text{DL}}$, e.g. due to variations of the local ohmic solution impedance, or a dispersion due to surface adsorption/diffusion processes, often of impurities. One critically important aspect to keep in mind is that the usage of a CPE in data fitting can be quite misleading when it comes to physically accurate interpretation of EIS results. For example, from Fig. 2.10, it is obvious that mathematical description of measured data might be achieved quite well when using a CPE-modified Randles circuit. However, the possibility to physically interpret obtained fitting results with regard to seperated contributions of the respective half-cell reactions is lost. Instead, carefully analyzing the underlying DRT governed by Eq. 2.28 can yield more detailed and meaningful insights.
Following pioneering works of *Macdonald* [224–228] and others [198, 229–231],
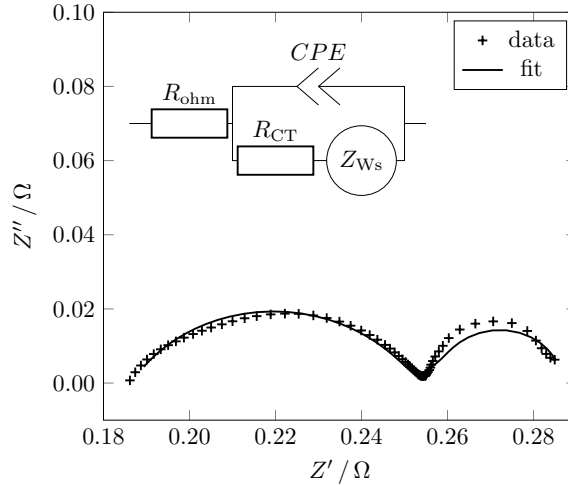
Figure 2.10: Full cell EIS data of a single-cell VRFB and respective fit obtained using a CPE-modified Randles circuit with finite-length, transmissive boundary Warburg element, often denoted as short Warburg element Ws.

this approach has seen an increased attention and further methodological development in recent years [197, 200, 232–235]. It has found widespread application in fuel cell [231, 236–240] and Li-ion battery [218, 241–243] research and is emerging as state of the art in EIS data evaluation in these fields, not least because of the comprehensive research activities in the group of *Ivers-Tiffée* [244]. Surprisingly, prior to the work conducted in conjunction with this thesis, no study on the DRT in VRFB, or even RFB in general, has been available in the open literature. This is remarkable to a certain extent, as DRT analysis can be regarded superior to common CNLS fitting of discrete ECMs in at least two decisive aspects. First, the need to find and validate a physically adequate model prior to data analysis is omitted, since a generalized "mesurement model" (cf. Voigt circuit at page 30) is used instead, as will be discussed below. This enables examining scarcely investigated systems where little to no knowledge about the occuring processes and their physical nature is available beforehand.

Second, different processes can be recognized and discriminated as distinct peaks located at their respective relaxational time constant τ in the DRT representation, as displayed in Fig. 2.11. Therefore, several time constants per decade can be distinguished, which would otherwise yield overlapping contributions in a Nyquist or Bode plot that can not be resolved by common CNLS fitting approaches. Physical interpretation of results can be achieved by following the dependencies of features apparent in the obtained DRT on systematically varied measurement parameters [244]. That way, DRT analysis can be used on its own as a powerful tool to study a system's dynamic behaviour or to identify all present processes and derive a suitable ECM.

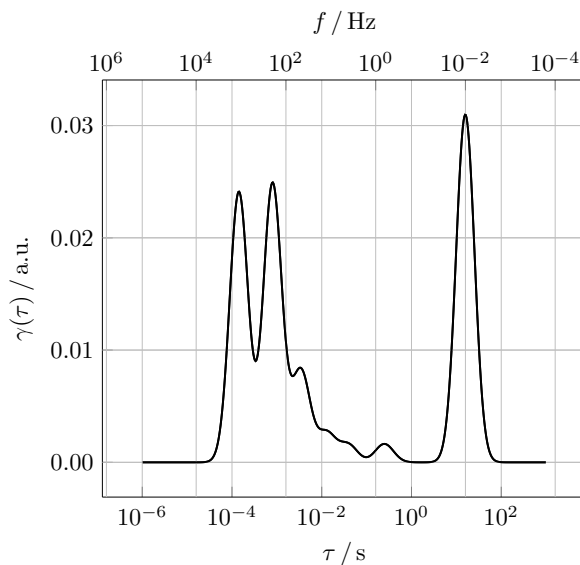Obtaining the underlying distribution by inversion of experimental data ac-

Figure 2.11: Exemplary distribution of relaxation times of a VRFB obtained from the full cell EIS data shown in Fig. 2.10.

cording to Eq. 2.28 involves solving a Fredholm integral equation of the first kind [245–247], which is a mathematically ill-posed problem. Therefore, a

variety of approaches employing regularization have been proposed, e.g. Fourier transform [229, 231], Tikhonov regularization [232, 238, 248–251] maximum entropy [252, 253], or evolutionary programming [254, 255]. Throughout this thesis, Tikhonov regularization was used to unravel the underlying DRT of experimental data. This approach was chosen owing to its ease of implementation and its capability to faithfully reproduce DRT even in rather complex cases [239, 256]. It can be briefly summarized as follows [230, 249].

A Fredholm integral equation of the first kind can be generally formulated as:

$$g(E) = \int_a^b K(u, E) f(u) \mathrm{d}u \tag{2.29}$$

where $g(E)$ is the measured quantity, $K(u, E)$ a known kernel function and $f(u)$ the unknown distribution. With $u = \tau$, $E = \omega$, $g(\omega) = \frac{Z(\omega) - Z_\infty}{Z_0 - Z_\infty}$, $K(\tau, \omega) = \frac{1}{1 + i\omega\tau}$, $f(\tau) = G(\tau)$ and lower and upper integration limits of 0 and ∞, respectively, equation 2.28 is obtained. In order to solve this equation, $G(\tau)$ is numerically approximated by discretizing the problem, i.e. transforming Eq. 2.28 into a system of linear equations:

$$\mathbf{g} = \frac{Z(\omega) - Z_\infty}{Z_0 - Z_\infty} = \sum_{l=1}^n \frac{\gamma(\tau_\mathrm{l})}{1 + i\omega\tau_\mathrm{l}} = \mathbf{Kf} \tag{2.30}$$

where $\gamma(\tau) = \tau G(\tau) \Delta \ln \tau$. As a sidenote, the discrete sum herein is reminiscent of the one used in Eq. 2.26 to express the impedance of a Voigt circuit. In fact, obtaining the distribution function $\gamma(\tau)$ can, in analogy to the linear KK transform, be interpreted as fitting a Voigt circuit to experimental EIS data[5]. The number of time constants n is chosen as a multiple of the number of measured data points m. Furthermore, the pre-defined time constants are determined as logarithmically equispaced values between τ_min and τ_max, obtained as:

$$\tau_\mathrm{min} = 10^{floor\left(\log\left(\frac{1}{f_\mathrm{max}}\right)\right) - b} \, \mathrm{s}$$

$$\tag{2.31}$$

$$\tau_\mathrm{max} = 10^{ceil\left(\log\left(\frac{1}{f_\mathrm{min}}\right)\right) + b} \, \mathrm{s}$$

---

[5]In fact, both approaches differ significantly only in the way regularization is ensured during the fitting process. While the linear KK transform aims at yielding the *best fit* possible for a given data set, the goal of DRT analysis is to find the *optimal fit* in order to identify the actual underlying physical distribution.

Herein, parameter b allows for an expansion of the time domain beyond the range of measured frequencies. This enhances the inversion quality at the boundaries of the spectrum. Based on gained experience, it is sufficient to set $b = 3$.

Having set the time constants and constructed the kernel matrix $\mathbf{K}$, the DRT is obtained by solving Eq. 2.30 with respect to $\mathbf{f}$. This is achieved by least-squares minimization and finding:

$$\min \left(\|\mathbf{K}\mathbf{f} - \mathbf{g}\|^2 \right) \tag{2.32}$$

where $\|*\|$ denotes the euclidian norm. Since this is an ill-posed problem, Tikhonov regularization is applied by extending the cost function by a regularization term according to [257]:

$$\min \left(\|\mathbf{K}\mathbf{f} - \mathbf{g}\|^2 + \lambda \|\mathbf{M}\mathbf{f}\|^2 \right) \tag{2.33}$$

where λ is the regularization parameter and $\mathbf{M}$ the regularization matrix. In the simplest case, which was also used for the calculations presented herein, $\mathbf{M} = \mathbf{I}$, the $n \times n$ identity matrix. Further options are discussed in Ref. [249]. Since negative contributions to the impedance are not reasonable according to Eq. 2.28, a non-negative least-squares (NNLS) solver [258] is used, which causes a three-fold implication. First, any possible inductive contribution to the impedance will be neglected and ignored during the fitting routine. In EIS data of VRFB, inductive behaviour might be observed in the high freqency range ($\geq 1 \times 10^5$ Hz). However, this can be ruled out as being insignificant as it stems from cable inductances resulting from the measurement setup and not from the battery itself. Therefore, using this somewhat limited approach is still justified. Second, the solver can not handle complex valued inputs and third, it is only able to deal with problems in the form of Eq. 2.32, but not in the form of Eq. 2.33. Luckily, these constraints can be circumvented as follows. The use of complex valued inputs could in principle be avoided, if only the real or imaginary part of the impedance is used:

$$\min \left(\|\mathbf{K}^*\mathbf{f} - \mathbf{g}^*\|^2 \right) \tag{2.34}$$

with $\mathbf{K}^* = Re(\mathbf{K})$ and $\mathbf{g}^* = Re(\mathbf{g})$, or $\mathbf{K}^* = Im(\mathbf{K})$ and $\mathbf{g}^* = Im(\mathbf{g})$.

For linear and time-invariant data obeying the Kramer-Kronig relationships [210] it may be justified to use either one of real or imaginary part for calculating the DRT. However, especially in the presence of noise, which is practically unavoidable during actual measurements, it is always favourable to use all

information available. Thus, a combined fit taking into account real as well as imaginary part can be obtained by letting:

$$\mathbf{K}^* = \begin{bmatrix} Re(\mathbf{K}) \\ Im(\mathbf{K}) \end{bmatrix} \tag{2.35}$$

as well as:

$$\mathbf{g}^* = \begin{bmatrix} Re(\mathbf{g}) \\ Im(\mathbf{g}) \end{bmatrix} \tag{2.36}$$

Furthermore, the problem stated in Eq. 2.33 has to be rearranged to take a form similar to Eq. 2.32 in order to be passed to the NNLS solver. This is achieved by using:

$$\min \left(\left\| \begin{bmatrix} \mathbf{K}^* \\ \lambda I \end{bmatrix} \mathbf{f} - \begin{bmatrix} \mathbf{g}^* \\ 0 \end{bmatrix} \right\|^2 \right) \tag{2.37}$$

which is equivalent [259] to:

$$\min \left(\|\mathbf{K}^*\mathbf{f} - \mathbf{g}^*\|^2 + \lambda \|\mathbf{If}\|^2 \right) \tag{2.38}$$

After having formulated the optimization problem in a way that is readily utilizable by the NNLS solver (Eq. 2.37), one crucial issue remains: choosing the regularization parameter λ.

The smaller λ, the less regularization will be applied, i.e. for $\lambda = 0$ a completely unregularized solution will be obtained. In this situation of *overfitting*, every outlier and all noise present in the experimental data will be taken into account. Consequently, $\mathbf{f}$ or $\gamma(\tau)$, respectively, will fail to adequately represent the underlying distribution but rather display additional peaks which lack physical justification. Using too large values of λ on the other hand leads to *underfitting*. In this case, distinct features of the true distribution may not be separable as the obtained peaks become very broad and start to overlap. The influence of the regularization parameter on the derived DRTs is illustrated in Fig. 2.12 for three different values of λ. Remarkably, when only judging from the Nyquist plots on the left-hand side of Fig. 2.12, each value seems to yield a more or less acceptable fit to the given data set, especially when comparing to the result of the conventional ECM-fitting presented in Fig. 2.10. However, the obtained DRTs differ drastically. Determining the optimum value of λ, i.e. finding the perfect balance between *under-* and *overfitting* might therefore be considered the fine art of DRT analysis (or of solving ill-posed problems in general, respectively).
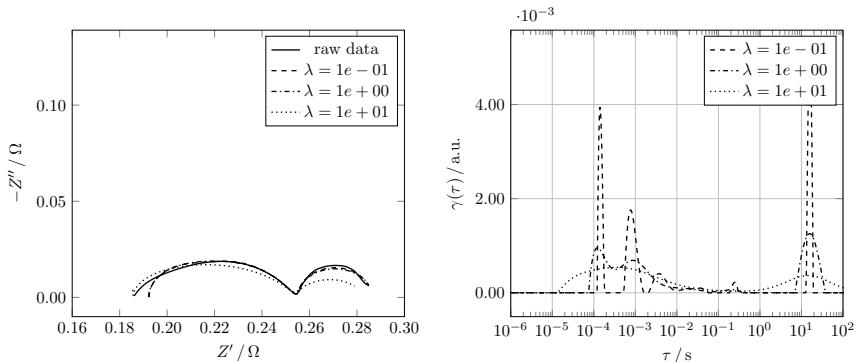
Figure 2.12: Influence of regularization parameter λ. Left: raw data (taken from Fig. 2.10) and obtained fits for three orders of magnitude of λ in Nyquist representation. Right: respective DRT.

Although a vast variety of approaches for optimal parameter choice in regularization of ill-posed problems is at hand [260], none of them appears to be universally accepted. For Tikhonov regularization, one widely used method is the *L-curve* which was first suggested by *Lawson and Hanson* [258] and later on extensively studied by *Hansen* [261–264] and others [265–267]. As can be seen on the left of Fig. 2.13, the characteristic shape of the L-curve is obtained when logarithmically plotting the solution norm $||\mathbf{Mf}||$ over the residual norm $||\mathbf{Kf} - \mathbf{g}||$ upon variation of the regularization parameter λ. The optimal value for the latter is supposedly found in the corner where the curve transitions from a straight vertical line towards a broad plateau region. However, as pointed out by *Hansen* [264], finding this corner point is not as mathematically straightforward as one might be tempted to think and in some cases even advanced algorithms fail to correctly determine it for discrete L-curves. Therefore, throughout this thesis a different but closely related approach was chosen to determine the optimal regularization parameter: the *S-curve* [268, 269], which is depicted on the right side of Fig. 2.13. It consists of a logarithmic plot of the residual norm with respect to the regularization parameter λ. Following this curve in order of ascending λ, the point of onset (where the shape of the curve starts to deviate from being a straight line) marks the transition from
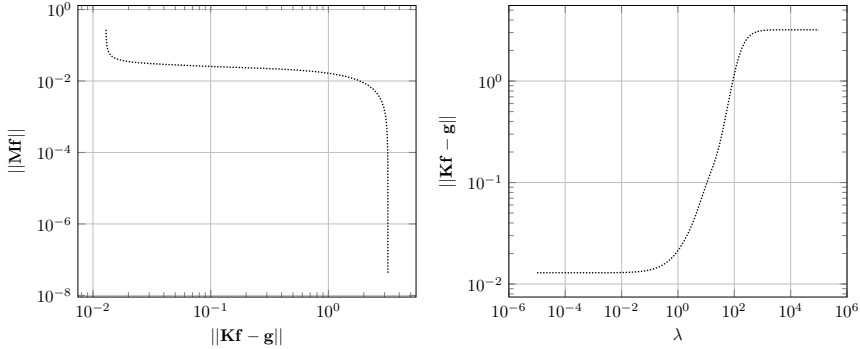
Figure 2.13: Parameter choice in Tikhonov regularization - left: L-curve as logarithmic plot of solution norm with respect to residual norm, right: S-curve as logarithmic plot of residual norm with respect to regularization parameter.

over- to underfitting and can therefore be regarded as the point of optimal λ. As discussed by *Fordham et al.* this λ_{opti} is a highly problem-specific quantity [268], related to the measurement noise level as well as the actual underlying distribution. They therefore introduced an additional parameter TOL, defined as

$$TOL = \frac{d(||\mathbf{Kf} - \mathbf{g}||)}{d(\lambda)} \tag{2.39}$$

and proposed to use $TOL = 0.1$. Since this is, in contrast to λ_{opti}, a data-independent parameter, using a fixed value of TOL allows for comparison of different data sets with the same degree of balancing between under- and overfitting. Another advantage is that accordingly the task of finding λ_{opti} can be fully automated quite easily: the S-curve in Fig. 2.13, which had been calculated for one hundred values of λ between 1×10^{-5} and 1×10^{5}, was first interpolated to one thousand points using a smoothing spline function[6]. For each point, TOL was calculated and the point closest to $TOL = 0.1$ was determined. The corresponding value of λ was taken as λ_{opti} and finally used to calculate the DRT of the EIS data from Fig. 2.10. As shown in Fig. 2.14,

---

[6]to be precisely: the function *InterpolatedUnivariateSpline* of the Python module *scipy.interpolate*

using the obtained value of $\lambda_{\mathrm{opti}} = 0.171$ enables faithful reproduction of the experimental data set. The several apparent features in the DRT representation can be assigned to the respective electrochemical processes occuring in the battery cell by studying their behaviour under varied experimental conditions [241, 243, 270]. Once the assignment is established and verified, it may be used to develop an accurate ECM of the system under study [242]. On the other hand, creating and using an ECM might as well be entirely omitted once the DRT is fully understood. Especially when dealing with degradation processes, the rigid construct of an ECM is likely failing to reflect time-dependent changes in the impedance behaviour. For instance, additional features could evolve or formerly present features could as well disappear as ageing and degradation progress. An ECM created at a fixed point in time is not able to capture such developments. Instead, following the evolution of the DRT over time, e.g. during a prolonged cycling experiment, enables straightforward visualization of degradation processes. That way, electrode degradation in VRFB (or other types of batteries, fuel cells, ...) can be monitored *in operando* once the feature related to the R_{ct} of the respective electrode reaction is identified, as the latter is directly tied to the state-of-health of the electrode itself.
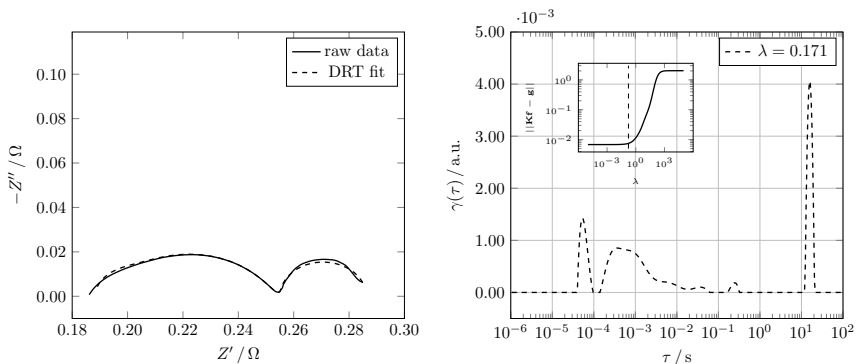

Figure 2.14: DRT fit obtained with optimized regularization parameter. Left: Nyquist plot of measured data and EIS data calculated from obtained DRT, right: respective DRT. The inset shows the corresponding S-curve where $TOL = 0.1$ is indicated by a dashed line.

Chapter 3

Experimental considerations

3.1 Reproducible measurement of ex-situ EIS

Electrode materials for (V)RFB applications are commonly characterized *ex-situ* by means of stationary half-cell measurements before moving on to testing in an actual flow-cell environment (*in-situ*). This preliminary evaluation in a *3-electrode-setup* is particularly popular owing to its ease of implementation and the low time consumption, especially when compared to prolonged charge-discharge cycling of a full RFB cell. Furthermore, it offers the possibility to make use of a wide variety of electrochemical techniques, such as CV, EIS, Chronopotentiometry or -amperometry. However, a few pitfalls exist and should be accounted for when using such a setup for reliable and reproducible measurements.

As depicted in Fig. 3.1, a 3-electrode-setup consists of a working electrode (WE), a counter electrode (CE) and a reference electrode (RE) immersed in an electrolytic cell. During an experiment, the potential of the WE is controlled with respect to the RE. Ideally, the latter behaves as a purely Ohmic resistor with a low resistance value (around $1\,k\Omega$). It is connected to a high impedance lead of the potentiostat in order to prevent any flow of current between the two electrodes. Since for the electrode reaction(s) of interest to occur at the WE some current has to flow within the electrolytic cell, a third electrode
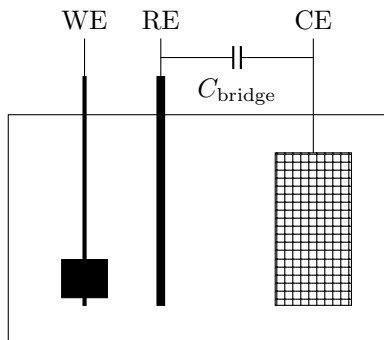
Figure 3.1: Exemplary sketch of a 3-electrode-setup with capacitor bridge.

is used - the CE. The impedance of this electrode has to be insignificantly small compared to that of the WE so the current flow is governed only by the latter. This is often achieved by using electrodes as CE that feature multiples of the (geometrical) area of the WE and are composed of the same material or a Pt mesh. Having a RE incorporated into the experimental setup enables precise control over the potential of the WE as well as arbitrary variations of it. This opens up an enormous space of possibilities to study individual half-cell reactions under stationary, quasi-stationary or dynamic conditions and in different regimes of dominating overpotentials.

On the other hand, improper use of a reference electrode can lead to highly erroneous results as will be discussed in the following. Besides the obvious need for a stable potential of the RE (which should be continously monitored), also the aforementioned prerequisite of low impedance is better not ignored [271]. A clogging of the porous frit or trapped bubbles can lead to a servere increase of RE impedance (Z_{RE}). As this doesn't affect the RE's DC potential, it is usually not an apparent issue with DC measurements. In AC experiments, however, high Z_{RE} will have a worsening effect on the emergence of high frequency artifacts. These artifacts mainly arise since unlike an ideal RE, a real one will always (to some extent) exhibit capacitive contributions to its impedance. Even allegedly small capacitances in the range of pF are enough to form a low-pass filter with the Ohmic resistance of the RE. Exhibiting a time constant of some

ns, such a filter is able to introduce pseudo-features (artifacts) in the MHz range of impedance spectra. In a more elaborate picture, first established by *Fletcher* [272], these high frequency artifacts are explained based on a three-terminal network that yields a better representation of a real electrochemical cell than the most commonly used but oversimplified two-pole circuit (WE vs. RE). As depicted in Fig. 3.2, all three electrodes are coupled by stray
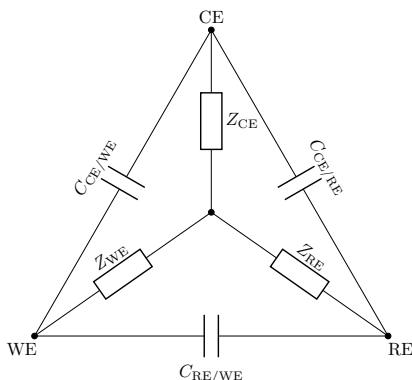

Figure 3.2: Three-terminal equivalent network of a 3-electrode cell according to Fletcher [272].

capacitances which allow for leaking currents at high frequencies. After deriving a two-terminal equivalent representation of the three-terminal network, *Fletcher* concluded that an inductive artifact emerges in series to the WE impedance and is accompanied by another capacitive artifact appearing in parallel to that serial connection. His two-terminal representation was further refined and simplified by *Sadkowski and Diard* [273] to take the form shown in Fig. 3.3. For an experimental electrochemist, however, it is not enough to understand the origins of such artifacts.

Instead, actions have to be undertaken to minimize their effect on measured data as much as possible. These actions should involve optimizing cell geometry [274] and/or use of a capacitor bridge [271]. As already shown in Fig. 3.1, the latter usually comprises a small capacitor that couples RE and CE. The necessary capacitance value typically lies between $100\,\mathrm{pF}$ to $10\,\mathrm{nF}$, has to be
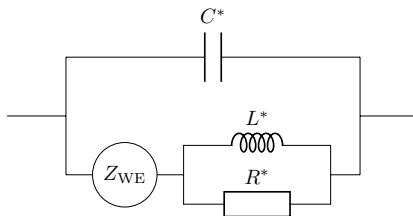
Figure 3.3: Two-terminal equivalent to the three-terminal network presented in Fig. 3.2 according to [273].

manually adjusted by trial and error and differs depending on the combination of potentiostat and electrochemical system. For the dataset shown in Fig. 3.4, using a 220 pF capacitor resulted in sufficient suppression of capacitive artifacts. In this example, the latter only effected data points above $f = 1\,\mathrm{kHz}$, complicating the proper determination of R_{Ohm}. However, in other situations (e.g. due to unfortunate geometrical placement of electrodes) the occurence of such artifacts might expand to even lower frequencies. It is therefore well worth to invest some time in finding a suitably valued capacitor and incorporate it into the 3-electrode-setup in order to maximize precision and quality of EIS results.

Another source of experimental challenges is the WE itself, mainly for two reasons. First, it is common practice to contact carbon felt (or carbon paper, carbon cloth, ...) electrodes by piercing them with a rod of glassy carbon or a pencil mine and connecting the latter with the potentiostat e.g. by means of a crocodile clip. Hence, the number of carbon fibers actually contacted may heavily vary between different samples of electrode. As a consequence, obtained values of R_{Ohm} are hardly ever reproducible. This should be kept in mind, especially when conducting further electrochemical experiments, e.g. using CV or when trying to extract key electrode characteristics like effective capacitance C_{eff} or R_{ct} from CPE parameters [275–277]. The second, and even more serious, challenge associated with carbon-based porous electrodes arises due to the hydrophobic nature of carbon surfaces. Even an electrode surface most densely populated with active sites will exhibit a low ECSA when insufficiently wetted with electrolyte. As was discussed earlier, this would purport poor electrode kinetics since the apparent value of R_{ct} is inversely proportional to
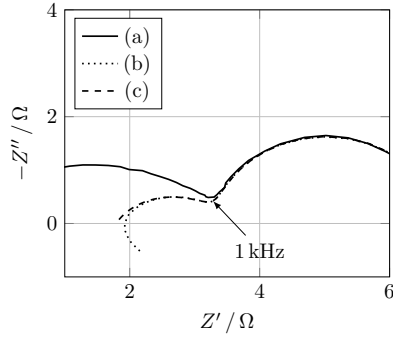
Figure 3.4: High-frequency artifacts in EIS: (a) raw data without capacitor bridge, (b) suppression of capacitive artifact by using $C_{\mathrm{bridge}} = 220\,\mathrm{pF}$ and (c) data of (b) after additional fitting and subtraction of inductive artifact.

ECSA. Inconsistent wetting of electrode samples within measurement series can therefore lead to highly distorted results and possibly false conclusions regarding a comparative kinetic assessment of different electrode materials. *Goulet et al.* have been able to demonstrate how subjecting carbon paper electrodes to short pulses of anodic current prior to actual measurements can increase wetting and enhance perceived kinetic properties of said electrodes [75]. This effect is much likely due to an increase in oxygen-containing functional groups which lead to a more hydrophilic behaviour of the carbon surface. While these findings may serve to explain a lot of discrepancies found in VRFB literature with regard to reaction rates of the vandium redox couples, utilizing such anodic pre-treatments is still of limited use for tackling the core issue related to electrode wetting: poor reproducibility. Known attempts to increase the latter involve e.g. soaking felt electrodes with electrolyte for several hours prior to measurements or enforcing wetting by using cells designed to incorporate electrolyte flow within a three-electrode setup [278].

However, an arguably more reliable way of comparing kinetic properties of electrode materials would be enabled if R_{ct} values normalized with respect to ECSA were taken into consideration. That way, the effect of wetting could be discriminated from actual changes of intrinsic kinetic properties. In a number
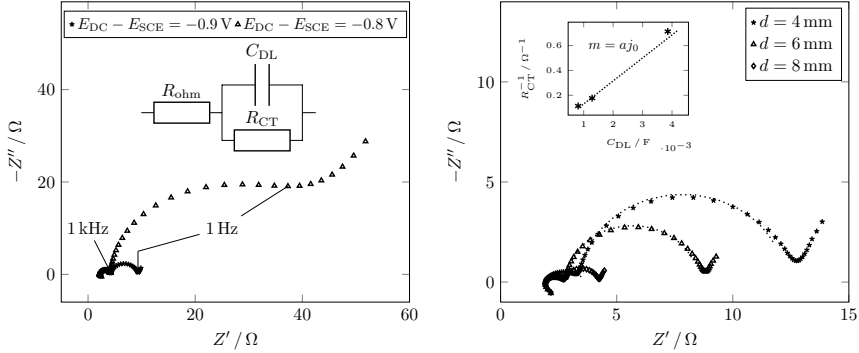
Figure 3.5: Normalization of EIS data.

of publications, *Friedl et al.* have established such a normalization in a rather elegant fashion [58–60]. Elegant, because by rearranging the formula expression of C_{dl} (Eq. 2.22) with respect to A_{wet} and substituting into the expression of R_{ct} (Eq. 2.21) according to

$$R_{CT}^{-1} = \frac{nFt_{DL}}{RT\epsilon_r\epsilon_0}j_0C_{DL} \tag{3.1}$$

they were able to eliminate the need to determine the actual magnitude of A_{wet} ($\widehat{=}$ ECSA), which would otherwise be anything but a straightforward task in case of porous electrodes. According to Eq. 3.1, collecting EIS data of at least three sample pieces (of varying geometrical size) per electrode material and plotting the inverse charge-transfer resistance with respect to double-layer capacitance (both obtained via ECM fitting) will yield a linear correlation. The slope of the resulting best fit straight line is directly proportional to j_0 and can therefore be used synonymously for comparing kinetic properties of electrode materials. As this approach enables to unanimously and reliably quantify electrocatalytic or degradation-induced effects in a straightforward manner, it is of central importance for the work conducted within the framework of the present thesis. The usage of this methodology is illustrated in Fig. 3.5. The left hand side shows Nyquist plots obtained from repeated measurements at one and the same sample of carbon felt under varied DC potential in order to identify the spectral region dominated by R_{ct}. Since the R_{ct} is a function of the potential

difference $\Delta E = E_{\mathrm{DC}} - E_{1/2}$ between applied DC potential E_{DC} and half-wave potential $E_{1/2}$, it will show a strong variation under altered DC conditions. For a reversible reaction with symmetrical energy barrier ($\alpha = 0.5$), R_{ct} will exhibit a minimum at $E_{1/2}$ [149]. In any case, moving away from $E_{1/2}$ will increase R_{ct}, which manifests in a semiarc with growing diameter in the Nyquist plot. Herein, said semiarc manifested between 1 kHz and 1 Hz. Once this region is identified, an ECM $R(R_{\mathrm{ct}}C_{\mathrm{dl}})$ is fitted to respective data points to obtain values of R_{ct} and C_{dl}. This is conducted for three differently sized sample electrodes, measured under otherwise identical experimental conditions (electrolyte composition, DC potential, temperature, ...), as shown at the right hand side of Fig.3.5. The inset contains the final plot of R_{CT}^{-1} versus C_{dl} and the fitted straight line bears a slope $m = aj_0$, where $a = (nFt_{\mathrm{DL}})/(RT\epsilon_{\mathrm{r}}\epsilon_0)$. Comparison of m for different types of electrode materials enables *ex-situ* benchmarking of intrinsic kinetic properties as well as assessing the effects of routines for pretreatment (or activation) of electrodes, of modifying electrode materials with (presumably) electrocatalytic moieties or of degradation processes on said kinetic properties.

3.2   Ensuring stability during in-situ EIS

Precise control and continuous monitoring of state of charge (SOC) is probably one of the key aspects of conducting *in-situ* or even *in operando* characterization of VRFB systems. Not only is a consistent SOC needed in order to assure comparability between consecutive measurement series. Especially in case of EIS experiments, it is imperative to keep a constant SOC throughout the whole duration of data gathering to not violate the stability criterion (cf. Fig. 2.8 on page 31). This has proven to be quite cumbersome when attempting to fully cover the low-frequency region dominated by mass-transport impedance. Even more so when using a DC bias, as will be discussed below.

Given the importance of SOC control in VRFB, the development of reliable methods for real-time monitoring has been an active field of ongoing research. Methods proposed so far have been relying on e.g. UV/Vis [279–281] or IR [282] spectroscopy, ultrasonic probing [283], amperometry [284] or measurements of electrolyte properties such as viscosity [285], density [286] or conductivity [279]. Common disadvantages of these approaches are the need for complex calibration and/or the necessity to integrate additional, often cost-intensive, equipment into the test setup. On the other hand, for a VRFB at its initial stage of life, freshly assembled using pristine components and electrolyte, it is sufficient to rely on the Nernstian relationship between OCP and SOC [33]. Given the logarithmic nature of the Nernst equation, small deviations in active ion concentrations will exhibit only a minor influence on the OCP at a SOC of (or close to) 50%, whereas showing increasingly drastic effects on OCP for SOC tending towards 0% or 100%. It is therefore highly advisable to carry out cell characterization at a SOC of 50% in order to maximize reproducibility between measurements. With ongoing cycle life, due to ion and water crossover as well as parasitic side reactions, the Nernst relation loses validity and values of SOC calculated from measured OCP will increasingly deviate from actual SOC. At the extreme, even actual SOCs found in both half cells might differ from each other, further highlighting the importance of advanced methods for SOC monitoring such as the ones mentioned above. As development and implementation of those have been far beyond the scope of the thesis presented herein, fresh electrolyte of a preset SOC of 50% was supplied to the test setup at all times prior to electrochemical cell characterization. Said electrolyte had been provided by a designated VRFB cell, which served this purpose exclusively. The impedance of this cell was continuously monitored and if it showed a significant increase, the cell would be reassembled using pristine components.

However, reproducibly supplying electrolyte of a predefined SOC may not in all cases be sufficient to guaranty reliable *in-situ* characterization of a VRFB. For instance, depending on the lower frequency limit during an EIS measurement, data acquisition time may span over the range of a few seconds to several minutes. If this limit is extended to lower frequencies in order to cover the regime dominated by mass-transport, experimental duration may further stretch to hours or even days. At such time scales, self-discharge becomes significant when conducting measurements at OCP. Thus, measures have to be taken to assure a constant SOC in order to not violate the stability criterion of EIS. This issue is obviously even more pressing if a charging or discharging DC bias is to be imposed during measurements.

Probably the most straightforward way of ensuring a constant SOC is the *single-pass* experiment [219], in which large quantities of pre-charged electrolyte will be supplied to the cell. However, instead of being recirculated into the storage tanks, the electrolyte will pass the cell only once. Given the resource-intensive nature of this approach, it has not been utilized herein. Alternative approaches involve the *cell-in-series* [220] or the *double half cell (DHC)* [26, 67, 221, 287–289] setup, which both allow for economical electrolyte utilization but on the other hand require for modifications of the test setup. However, these modifications are rather small and straightforward to implement when compared to e.g. the methods for SOC monitoring discussed above.

In contrast to a typical cell stack, where several cells are electrically connected in series and in parallel with respect to electrolyte flow, the *cell-in-series* setup comprises two RFB cells serially linked in terms of electrolyte flow but (ideally) independent of each other regarding electrical connections. With such an arrangement, the cell of interest can be thoroughly characterized or subjected to (accelerated) degradation routines, e.g. prolonged charging at high current densities, while the second cell is used to set and maintain a constant SOC. This is best achieved if the geometrical electrode area of the second cell is large compared to that of the first. In that case, high current densities in the cell of interest translate to absolute currents that require only for low current densities in the second cell to be balanced, therefore inflicting the least possible amount of stress on the components of the latter. One aspect to keep in mind when working with such a setup is that even though the two cells appear to be controlled independently, they are in fact linked by the flow of electrically conducting electrolyte. This might possibly lead to shunt currents which would in turn manifest as artifacts in measured impedance spectra.

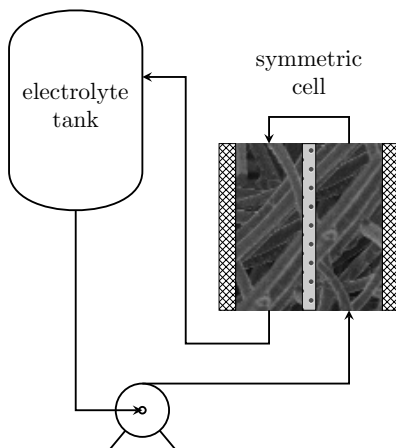Symmetric or double half cell (DHC) operation enables selectively studying

Figure 3.6: Schematic view of a double half cell setup.

one of the individual half cell reactions under realistic conditions of convective electrolyte flow while eliminating the need to install a reference electrode. As depicted in Fig. 3.6, it consists of a full cell fed with only one electrolyte solution supplied by either the negolyte or posolyte tank. The flow is directed consecutively through the electrode spaces in both half cells before being recirculated into the storage tank. That way, the forward reaction occuring in one half cell is directly reversed within the other, effectively conserving the overall SOC. So far, DHC setups have been used to probe the influence of electrode and flow field geometry [26, 287], electrode material [26, 67, 287] or temperature [289] on the redox reactions of V(II)/V(III) and V(IV)/V(V), respectively. Throughout the experimental works carried out in conjunction with the thesis presented herein, such setups e.g. aided the assignment of peaks in the DRT representation of full cell EIS data (cf. section 4.2).

Chapter 4

Discussion of publications included in this thesis

4.1 Degradation Phenomena of Bismuth-Modified Felt Electrodes in VRFB studied by Electrochemical Impedance Spectroscopy

Motivation

Sluggish electrode kinetics and parasitic hydrogen evolution in the negative half cell are among the key obstacles to further development of efficient and durable VRFB systems. Using bismuth as an electrocatalyst has been claimed to tackle both issues by increasing the rate of the $V(II)/V(III)$ redox reaction while at the same time inhibiting the HER. As discussed in section 2.2, it remains unclear wether bismuth acts only via a surface effect (apparently raising i_0 due to improved wetting and thus enlarged ECSA of Bi-modified electrodes) or instead bears intrinsic catalytic activity (actually increasing k^0). Furthermore, as prolonged evolution of hydrogen supposedly causes a passivation of the carbon-based electrodes, modification with bismuth should, based on the above

mentioned claims, lead to a reduced rate of electrode degradation. The first objective of this study was thus to carefully evaluate the electrocatalytic properties of bismuth with regard to the V(II)/V(III) redox reaction. Subsequently, it was to be assessed if and possibly how the presence of bismuth would affect the durability of carbon felt electrodes in a VRFB.

Description and novelties

Carbon felt electrodes (GFD) were decorated with Bi_2O_3 following a simple impregnation route which comprised soaking felts in acidic solution of bismuth nitrate, immersing them in ammonia solution to induce precipitation followed by drying and heat treatment under inert gas atmosphere. Success of this operation was confirmed by SEM coupled with elemental mapping using energy dispersive X-ray spectroscopy (EDX). Subsequently, Bi-modified electrodes (Bi-GFD) were electrochemically characterized in a 3-electrode-setup using CV and EIS and compared to reference samples that had been either untreated (GFD-U), subjected to soaking with acid and ammonia (GFD-Ref) and subsequent heat treatment (GFD-Ref-HT) or only heat treated (GFD-HT). In all cases, Bi-GFD electrodes showed a higher apparent activity towards the examined V(II)/V(III) redox reaction, manifested by increased peak currents and lower peak separation in CV measurements as well as lowest R_{ct} observed during EIS. Interestingly, while all reference samples yielded nearly identical CV curves, impedance results indicated declining charge-transfer resistance R_{ct} in the order of GFD-U > GFD-Ref-HT > GFD-Ref > GFD-HT. This obvious contradiction between results obtained by both measurement techniques underlines the deficiencies of the common approach for assessing electrode kinetics which relies on performing single measurements of CV and/or EIS and discussing thus obtained data without sufficiently taking into account the macroporous and predominantly hydrophobic nature of carbon felt electrodes. Further elaboration on CV results has not been pursued throughout this study, as it would have required for an advanced theoretical framework and sophisticated modelling capabilities which were both unavailable at that time and generally beyond the scope of this thesis. Instead, the focus has been on achieving reproducible and reliable electrode characterization via EIS. This was enabled by the normalization approach discussed previously (cf. section 2.2 and section 3.1). For each type of electrode, three samples of varying size were studied and inverse R_{ct} was plotted with respect to double-layer capacity C_{dl}, both of which were obtained by ECM fitting. From the resulting linear relationship, j_0 (which is directly

proportional to k^0) was infered without having to determine the inherently unknown ECSA. That way, any influence of wetting behaviour was eliminated, allowing to differentiate between apparent and intrinsic electrocatalytic properties. This study marked the first ever attempt to realize such a distinction for metal-based electrocatalysts in VRFB. As it turned out, the above-mentioned decrease in R_{ct} observed for the reference samples during single EIS measurements had only been an apparent enhancement due to increased wettability. No increase in intrinsic electrocatalytic activity compared to GFD-U was found after normalization. On the other hand, the enhanced performance of Bi-GFD has been unambiguously verified to originate from the intrinsic electrocatalytic properties of bismuth.

Following this initial characterization, VRFB cells were assembled using either only GFD-U as electrode material or GFD-U and Bi-GFD in positive and negative half cell, respectively. In both cases, a full cell degradation test was conducted by subjecting the battery cells to 50 cycles of galvanostatic charging and discharging at a current density of $j = 100 \, \text{A cm}^{-2}$ and within voltage limits of $0.80 - 1.65 \, \text{V}$. The cell featuring Bi-GFD exhibited, in comparison to that comprising only GFD-U, slightly increased energy efficiency (EE) as well as higher capacity and lower cell impedance before and after cycling. However, the decline of accessible storage capacity followed a similar trend in both cases. Furthermore, full cell EIS revealed similar extents of electrode passivation as well as identical (relative) losses of ECSA, apparent from increased R_{ct} and decreased C_{dl}, respectively. This indicates that the presence of Bi is neither able to prevent electrode degradation nor to inhibit parasitic HER in VRFB. Additional investigation of negolyte using total reflection X-ray fluorescence (TXRF) spectroscopy strongly indicated that bismuth (oxide) particles not even remained stably on the electrode fibers during cycling but were instead leached into the electrolyte.

Upon completion of the cycling experiment, electrodes had been washed with dilute sulfuric acid and deionised water before being harvested for *ex-situ* postmortem analysis. The latter again consisted of combined SEM/EDX examination followed by electrochemical characterization in a 3-electrode setup. No remaining Bi could be found within electrode samples using EDX elemental mapping. Given this further evidence for the insufficient stability of bismuth in the negative half cell of a VRFB, it appeared plausible to expect similar electrochemical behaviour for both types of electrodes after cycling as both should have been essentially free of electrocatalytically active particles. However, while GFD-U showed the expected loss in activity, the formerly Bi-modified

electrode appeared to be completely passivated after the cycling experiment. This became apparent by the absence of reduction or oxidation peaks in the corresponding CV curve and an exchange current density $j_0 \approx 0$ obtained from normalized EIS results. It was therefore concluded that the presence of bismuth, in contrast to initial assumptions, accelerates the degradation rate of carbon felt electrodes in the negative half cell of a VRFB. As there has been no reasonable explanation at hand for this - somewhat surprising - finding, further investigations were conducted which will be discussed in section 4.4.

Key findings

- Intrinsic electrocatalytic activity of bismuth towards the V(II)/V(III) redox reaction has been unambiguously verified using normalized EIS approach

- For the first time in VRFB research, long-term stability of electrodes modified with metal (oxide) particles has been studied

- Bismuth (oxide) is not stable in the negative half cell of an operating VRFB

- Presence of bismuth apparently accelerates electrode degradation

4.2 Deconvolution of electrochemical impedance data for the monitoring of electrode degradation in VRFB

Motivation

Cost-competitive operation of VRFB as large-scale energy storage solutions is possible if the projected lifetime of more than 20 years can be achieved in real application scenarios. In order to meet this requirement, all ageing phenomena occuring during charging, discharging and even at times of rest have to be thoroughly understood before respective mitigation strategies can be implemented. In that respect, contributions of electrode degradation to overall performance losses should not be neglected. Resolving these contributions for the individual half cell electrodes has so far only been possible by means of postmortem analysis using XPS or by incorporation of reference electrodes into *in-situ* test setups. Both approaches are highly cumbersome and impractical for industrial-scale RFB applications. Analysis of full cell EIS data in terms of a distribution of relaxation times (DRT) could be one possible way to overcome these challenges. Using this concept enables significantly higher resolving capabilities than the commonly employed equivalent circuit modelling and has been successfully utilized for identification and discrimination of processes in fuel cells or Li-ion batteries. Herein, it has been introduced to VRFB research for the first time.

Description and novelties

As has been exhaustively discussed in section 2.3.2, DRT analysis is enabled by subjecting frequency-dependent impedance data to an integral transform (cf. Eq. 2.28 on page 33). In the resulting representation, different processes are visualized as (optimally distinct) peaks centered around their respective characteristic time constants τ_{char} which, in turn, correspond to the frequencies in the source data by $f = \frac{1}{2\pi\tau}$. Upon transformation of a full cell impedance spectrum of a lab-scale single-cell VRFB, 5-7 peaks were observed in the DRT representation, depending on the lower frequency limit chosen during measurements. Experimental conditions have been varied in order to map these peaks to underlying physicochemical processes. This involved manipulating the flow rate of electrolyte, operating the battery in either full cell or symmetric

Table 4.1: Assignment of peaks observed in the DRT representation of full cell EIS data of a single cell VRFB.

peak	frequency range	assignment
P1	$> 10\,\text{kHz}$	distributed Ohmic resistance
P2	$3 - 1\,\text{kHz}$	anion exchange membrane
P3	$500 - 100\,\text{Hz}$	negative half cell kinetics
P4, P5, ...	$< 100\,\text{Hz}$	mass transport

cell mode (cf. section 3.2) and performing several consecutive measurements of EIS while increasing DC bias. Based on the sum of observations thus gathered, as well as a thorough review of pre-existing literature, apparent peaks were finally classified according to table 4.1. For a detailed discussion of the reasoning behind these assignments, the reader is kindly referred to the text of the original publication (cf. section 5).

Remarkably, one of the major contributions (P3) to the full cell impedance was found to originate solely from the kinetic limitations of the negative half cell reaction. None such limitation could be observed for the electrode reaction in the positive half cell. Instead, the latter appears to be dominated by Ohmic resistance and mass transport impedance. These findings imply that kinetic properties of the negative half cell electrode can be readily assessed from full cell impedance spectra without having to adopt complicated setup modifications (e.g incorporation a reference electrode). This capability of DRT analysis was further demonstrated to enable *in-situ* monitoring of electrode degradation in the negative half cell of a VRFB. An accelerated stress test was performed, using a cell-in-series arrangement (cf. section 3.2), in which the cell of interest was constantly charging for two days at both high current density and high SOC. This induced an anticipated and significant increase in P3 while, interestingly, all other peaks remained rather unaffected. As a consequence, for future investigations in that context it might be sufficient to run measurements within a limited frequency range $(500 - 100\,\text{Hz})$ and still be able to extract all necessary information on electrode kinetics. That way, data acquisition time would be effectively shortened to about $10\,\text{s}$.

Another noteworthy aspect is the assignment of P2. It was made based on the assumption of a capacitive contribution to membrane impedance due to the proposed formation of a charge double layer at the membrane/electrode

interface in a VRFB. While this plausible hypothesis served well to explain observed experimental results, it stands in contrast to the prevalent conviction that ion exchange membranes would behave as purely Ohmic resistors. If future studies were able to verify these assumptions, DRT analysis would also enable *in-situ* extraction of additional information regarding SOH of the membrane from full cell impedance spectra.

Key findings

- DRT analysis has been applied to EIS data of a single cell VRFB for the first time

- Apparent peaks were attributed to distributed ohmic resistance of the porous electrodes, capacitive contributions of the anion exchange membrane, charge-transfer kinetics of the negative half cell reaction as well as mass transport

- Negative half cell electrode has been identified as sole source of kinetic limitation, constituting a major contribution to overall cell impedance

- Said limitation increased with ongoing electrode degradation

- DRT analysis has been demonstrated as viable tool for *in-situ* degradation monitoring of negative half cell electrode (and possibly ion exchange membrane as well)

4.3 Rotating ring-disc measurements for the quantitative electrokinetic investigation of the V^{3+}-reduction at modified carbon electrodes

Motivation

An indefinite and evergrowing number of modifications to carbon-based electrode materials have been proposed in order to enhance the kinetics of the V(II)/V(III) redox reaction. However, proper determination of kinetic parameters and thus robust benchmarking of these electrodes is not only impeded by insufficient utilization of electrochemical characterization techniques (cf. previous discussion on page 13) but also by emergence of the parasitic HER. The latter leads to measured electrochemical responses unexceptionally consisting of convoluted contributions of both, parasitic side reaction and desired reduction of V^{3+}. Since no reliable approach for discrimination between the two had been at hand, this study aimed at determining the respective current contributions at well-defined, planar model electrodes using the RRDE technique. Further support of the experimental findings was provided by measurement and simulation of CV as well as employment of EIS with subsequent DRT analysis and ACCV.

Description and novelties

Rotating disk electrode (RDE) investigations are an indespensable tool in fundamental electrochemistry as they allow for detailed examination of model electrodes under controlled conditions of semi-infinite diffusion. The size of the diffusion domain is hereby precisely controlled via the rotation rate of the electrode tip. The rotating ring-disc electrode (RRDE) technique further advances this concept by endowing the latter with an additional ring. Typically, disc and surrounding ring consist of glassy carbon and platinum, respectively, and are independently controlled using two seperate potentiostats (or two channels of an according multi-channel instrument). This opens up enormous possibilities to let the forward reactions occuring at the disc be selectively reversed for certain species upon contacting the ring.

Herein, a commercial RRDE tip was modified by applying a Cu/C coating to the ring, rendering it fully deactivated with respect to the oxidation of hydro-

gen. It was thus ensured that out of H_2 and V^{2+} produced at the disc during a cathodic scan only the V^{2+} would be re-oxidised at the ring. Monitoring the ring current during such an experiment thereby enabled quantifying the amount of V^{3+} reduced at the disc. By subtracting the corresponding current from the overall disc current, the current related to the HER has been determined simultaneously. This marks the first time in VRFB research that a satisfactory distinction between parasitic HER and desired vanadium reduction was achieved. To add further value to this study, the diffusion coefficient of V^{3+} in sulfuric acid solution was (also for the first time) determined to be $D_{V^{3+}} = 3.51 \pm 0.22 \mathrm{cm}^2\,\mathrm{s}^{-1}$.

These insights were put to direct use in the characterization of four different model electrodes comprising carbon black material Vulcan® XC-72 either in its pristine form or etched using H_2O_2, KOH or a mixture of HNO_3 and H_2SO_4 with a molar ratio of 1:1. Those types of etching treatment were chosen since in pre-existing literature they had been claimed to enhance electrode kinetics of the V(II)/V(III) redox reaction at porous carbons. Herein, however, the following trend regarding the rates of V^{3+}-reduction was observed: H_2O_2-XC-72 > pristine XC-72 > KOH-XC-72 $\gg$ HNO_3/H_2SO_4-XC-72. On the other hand, while H_2O_2-etching induced a slightly higher activity towards the vanadium reaction, it as well led to a fourfold increase in the rate of hydrogen evolution. The best trade-off between activity and selectivity towards the reduction of V^{3+} was actually achieved using pristine XC-72. In comparison, treatment with HNO_3/H_2SO_4 led to most severe deactivation of the electrode and the lowest ratio of $k^0(V^{3+})/k^0(H_2)$ among all electrodes studied, attributable to reduced intrinsic electrocatalytic activity. Etching with KOH was found to impair electrode performance mainly by causing a loss in ECSA.

It is worth noting, that all experimental techniques employed herein yielded coherent results regarding the trends discussed above. Considering the aforementioned claims made in previous literature, it appears possible that etching treatments applied to macroporous carbon felts cause increased wettability and mask the herein observed negative effects. Thorough investigation of such materials following the methodology outlined within this study are therefore highly in order. Unfortunately, conducting RRDE measurements is inappropriate for the assessment of macroporous electrodes. Instead, ACCV could constitute a straightforward alternative. This sophisticated technique uses a sine wave superimposed to the triangular potential ramp of a CV experiment to excite higher harmonics of multiple electrode reactions. From the Fourier transform of the overall current response, signals present at integer multiples of the applied

excitation frequency are separately subjected to inverse Fourier transform to obtain the individual current responses to base signal (triangular ramp), fundamental frequency and first, second or higher harmonic(s). As was demonstrated in this study, HER at carbon electrodes constitutes an irreversible process and as such does not contribute to higher harmonics in ACCV experiments. Moreover, intensity of signals was observed to directly correlate with the rates of respective reactions previously obtained. ACCV thus enabled direct visualization of the trends established by elaborate RRDE and CV analysis. Consequently, it offers excellent prospects for application in strongly needed future attempts to distinguish contributions of desired V^{3+}-reduction and parasitic HER at carbon felt electrodes.

Key findings

- Experimental techniques of RRDE and ACCV have been introduced to fundamental VRFB research

- Unanimous distinction and simultaneous quantification of parasitic HER and desired V^{3+}-reduction was achieved

- Diffusion coefficient of V^{3+} in sulfuric acid solution was determined to be $D_{V^{3+}} = 3.51 \pm 0.22 \mathrm{cm}^2\,\mathrm{s}^{-1}$

- Common surface modification approaches didn't lead to anticipated improvements in electrocatalytic activity of carbon electrodes

- Apparent enhancements previously reported for felt electrodes much likely due to misinterpretation of increases in wettability or rate of HER

4.4 On the stability of bismuth in modified carbon felt electrodes for vanadium redox flow batteries: An in-operando X-ray computed tomography study

Motivation

In a previous study discussed in section 4.1, the intrinsic electrocatalytic activity of bismuth towards the V(II)/V(III) redox reaction had been verified. However, Bi-modification of carbon felt electrodes was found to not withstand conditions prevalent in the negative half cell of a VRFB during galvanostatic cycling experiments. Instead, bismuth (oxide) particles were apparently leached into the electrolyte, leaving a completely passivated electrode. One possible explanatory approach for this observed passivating effect, which was only developed after the former study had been published, is based upon current density distribution, which has to be considered an inherent feature of flow cells [17–20]. As the electrolyte is pumped through the battery cell, active species are converted upon passage of the electrodes. This inevitably leads to the emergence of concentration gradients between inlet and outlet of the cell with concentrations being highest at the former and successively decreasing towards the latter. Inhomogeneities of the electrodes might further add to local differences in the concentration of active species by impeding electrolyte flow in regions of higher hydrophobicity. This gives rise to additional local overpotentials, ultimately resulting in a distribution of current densities within the battery. Broadness of this distribution, i.e. local deviations from the average current density have been found to generally increase with higher current densities, lower flow rates and extreme SOC [17, 20]. Insufficient stability of electrode coatings could initiate cyclic dissolution and redeposition of metallic particles upon repeated charging and discharging. It appears to be a reasonable assumption that those particles would be predominantly deposited in regions of higher local current density. Given that the presence of metallic moieties will increase local hydrophilicity of the electrode and possibly catalyse vanadium redox reactions, this would lead to further broadening of the distribution. At the most extreme, the desired conversion of vanadium would take place exclusively at the spots where metal particles had been previously deposited while high overpotentials in the remaining areas of the electrode facilitated the occurence of parasitic side

reactions such as the HER. The aim of this study was to verify the plausibility of this hypothesis by visualizing the spatial distribution of bismuth within the negative half cell electrode of an operating VRFB. For this purpose, an in-house developed cell design, previously employed to study electrolyte distribution [290], was further modified to enable real-time X-ray imaging of the battery while performing actual charging and discharging experiments.

Description and novelties

X-ray radiography is an established experimental technique well-suited for investigating and viualizing distributions of metall (oxide) particles or electrolyte within macroporous carbon electrodes. Applying it to an operating VRFB requires for a dedicated measurement setup featuring a custom flow cell specifically designed for this purpose. This study describes the development of such a cell and discusses the necessary adjustments that had to be made to a typical VRFB test rig in order to enable the envisaged imaging investigations. The high temporal resolution of X-ray radiography facilitated capturing rapid changes of electrolyte or particle distribution within the electrode during operation of the cell. Further utilization of X-ray computed tomography allowed for additional imaging of steady states in superior spatial resolution.

It was demonstrated that bismuth oxide readily dissolves upon electroless contact with the electrolyte, confirming previous suspicions of low stability. However, a redeposition occured during galvanostatic charging with deposited particles remaining stably on the electrode throughout a subsequent charge/discharge cycle. Only after a prolonged period of contact with low SOC electrolyte at OCP conditions, renewed dissolution was observed. These findings indicate that several, supposedly impractical, restrictions to the operation of an industrial-scale VRFB would have to be enacted if Bi-based catalysts were to be employed in such a system. However, feasibility of the latter should be carefully reconsidered given that only negligible effects of bismuth on the electrochemical cell performance were found during galvanostatic cycling experiments within this study.

Furthermore, the influence of electrolyte velocity on the distribution patterns of deposited bismuth particles was evaluated. Expectedly, the penetration depth of the deposition process, and thus the homogeneity of achieved Bi-modification, was enlarged by increasing the pump rates of electrolyte. It might be therefore concluded that following the deposition of metallic particles using X-ray radiography serves well to exemplify the above-mentioned distribution of local

current densities within the electrodes of a VRFB. Although further investigations will be needed to ultimately verify the interplay of local inhomogeneities, metal deposition and supposedly accelerated electrode degradation, the findings presented herein support the plausibility of the initially raised hypothesis.

Key findings

- Advanced cell design enabled *in-operando* radio- and tomographic investigations of a fully functional VRFB

- Bi-modified felt electrodes showed complete dissolution of bismuth upon electroless contact with low SOC electrolyte

- Dissolved bismuth was redeposited and remained stably on the electrode during charging and discharging

- Correlation between deposition patterns and flow rate of electrolyte was demonstrated

Chapter 5

Original Manuscripts

Degradation Phenomena of Bismuth-Modified Felt Electrodes in VRFB studied by Electrochemical Impedance Spectroscopy

J. Schneider [1,*] , E. Bulczak [1] , G. A. El-Nagar [1,2] , M. Gebhard [1] , P. Kubella [3] , M. Schnucklake [1] , A. Fetyan [1] , I. Derr [1] , C. Roth [2]

[1] Institute of Chemistry and Biochemistry, Freie Universität Berlin, Takustr. 3, 14195, Berlin, Germany
[2] Chemistry Department, Faculty of Science, Cairo University, Cairo 12613, Egypt
[3] Department of Physics, Freie Universität Berlin, Arnimallee 14, 14195 Berlin, Germany
[*] corresponding author: J. Schneider

Author	Individual contributions
J. Schneider	Conceptualization, Data Curation, Formal Analysis, Investigation, Methodology, Validation, Visualization, Writing - Original Draft
E. Bulczak	Investigation
G. A. El-Nagar	Formal Analysis, Investigation
M. Gebhard	Investigation
P. Kubella	Investigation
M. Schnucklake	Methodology
A. Fetyan	Methodology
I. Derr	Conceptualization
C. Roth	Conceptualization, Funding Acquisition, Project Administration, Resources, Supervision, Writing - Review and Editing

Degradation Phenomena of Bismuth-Modified Felt Electrodes in VRFB Studied by Electrochemical Impedance Spectroscopy

Jonathan Schneider [1,*] , Eduard Bulczak [1] , Gumaa A. El-Nagar [1,2] , Marcus Gebhard [1] ,
Paul Kubella [3] , Maike Schnucklake [1] , Abdulmonem Fetyan [1] , Igor Derr [1] and
Christina Roth [1]

[1] Institute for Chemistry and Biochemistry, Freie Universität Berlin, Takustr. 3, D-14195 Berlin, Germany;
eduardb@zedat.fu-berlin.de (E.B.); elnagar087@yahoo.com (G.A.E.-N.); marcus.gebhard@fu-berlin.de (M.G.);
maike.schnucklake@fu-berlin.de (M.S.); abdul.fetyan@fu-berlin.de (A.F.); Derr.Ig@schmid-group.com (I.D.);
christina.roth@fu-berlin.de (C.R.)
[2] Chemistry Department, Faculty of Science, Cairo University, Cairo 12613, Egypt
[3] Department of Physics, Freie Universität Berlin, Arnimallee 14, D-14195 Berlin, Germany;
paul.kubella@fu-berlin.de
* Correspondence: jonathan.schneider@fu-berlin.de

Abstract: The performance of all-V redox flow batteries (VRFB) will decrease when they are exposed to dynamic electrochemical cycling, but also when they are in prolonged contact with the acidic electrolyte. These phenomena are especially severe at the negative side, where the parasitic hydrogen evolution reaction (HER) will be increasingly favored over the reduction of V(III) with ongoing degradation of the carbon felt electrode. Bismuth, either added to the electrolyte or deposited onto the felt, has been reported to suppress the HER and therefore to enhance the kinetics of the V(II)/V(III) redox reaction. This study is the first to investigate degradation effects on bismuth-modified electrodes in the negative half-cell of a VRFB. By means of a simple impregnation method, a commercially available carbon felt was decorated with Bi_2O_3, which is supposedly present as Bi(0) under the working conditions at the negative side. Modified and unmodified felts were characterized electrochemically using cyclic voltammetry (CV) and electrochemical impedance spectroscopy (EIS) in a three-electrode setup. Surface morphology of the electrodes and composition of the negative half-cell electrolyte were probed using scanning electron microscopy (SEM) and X-ray fluorescence spectroscopy (TXRF), respectively. This was done before and after the electrodes were subjected to 50 charge-discharge cycles in a battery test bench. Our results suggest that not only the bismuth catalyst is dissolved from the electrode during battery operation, but also that the presence of bismuth in the system has a strong accelerating effect on electrode degradation.

Keywords: vanadium; redox flow battery; degradation; bismuth; electrochemical impedance spectroscopy

1. Introduction

Throughout recent decades, redox flow batteries (RFB) have attracted considerable research interest due to their aptitude for large-scale energy storage applications [1–4]. Probably the most prominent and well-investigated system is the vanadium redox flow battery (VRFB), which was developed in the 1980s by the group of Skyllas-Kazacos [5]. However, high capital costs still impede a deeper market penetration and wider application. Therefore, the components of the VRFB must be further optimized to realize a less expensive overall system. One possible approach is to increase the

power density by enhancing the electrode kinetics for the respective half-cell reactions. This is especially the case for the negative half-cell, where in recent studies the V(II)/V(III) redox reaction was found to limit the overall system performance [6–10]. With ongoing electrode degradation, which manifests in an altered surface composition of the carbon fibers, this limitation becomes even more pronounced, since the kinetics of the V(II)/V(III) redox reaction largely depend on the presence of specific surface functional groups [10–15]. While the nature of this correlation is still under debate, it is evident that an inhibition of the V(II)/V(III) redox reaction will result in the parasitic hydrogen evolution reaction (HER) becoming the preferred reaction in the negative half-cell [16–18]. For this reason, several catalysts have been proposed and studied to enhance the V(II)/V(III) redox reaction [19]. Among others, such as Ce [20], Ti [21,22], Nd [23], Sb [24], Nb [25] and W [26], Bi is considered a promising catalyst [27–33]. Besides low cost and toxicity it shows an enhancing effect on the kinetics of the negative half-cell reaction, while effectively suppressing the HER. Remarkably, this is the case no matter if the bismuth is used as an electrolyte additive [27], deposited onto the electrode [28,29,31–33] or integrated into the carbon fibers via an electrospinning process [30]. Also, the choice of metallic or oxidic particles is of minor importance, since inside the potential window of the negative half-cell, bismuth should be present as Bi^0 [33]. However, while the catalytic effect of bismuth and other metals is obvious from full cell battery tests, many studies still rely on cyclic voltammetry (CV) and electrochemical impedance spectroscopy (EIS) results obtained by stationary half-cell measurements. Since the carbon electrodes used in VRFB are of porous nature, these investigations may not yield robust results if proper and reproducible wetting is not ensured. Any change in electrode hydrophobicity, affecting the wetting behavior, will drastically alter the electrochemical response of the examined electrode, as could be demonstrated lately [34]. It is, therefore, not sufficient to discuss peak separation and peak currents obtained by CV. Likewise, a meaningful interpretation of charge transfer resistances (R_{CT}) extracted from EIS measurements is not possible, if the effectively wetted surface area is not also considered. Since a straightforward determination of this parameter is usually not possible, Friedl and co-workers have proposed a normalization of R_{CT} values by the double layer capacitance (C_{DL}) [35–37], as the latter is directly proportional to the wetted surface area A^{wet}:

$$C_{DL} = \epsilon_r \epsilon_0 \frac{A^{wet}}{t_{DL}} \tag{1}$$

with ϵ_r being the relative dielectric permittivity, ϵ_0 the permittivity of the free space and t_{DL} the thickness of the double layer. The R_{CT} is in turn inversely proportional to the wetted surface area, according to:

$$R_{CT} = \frac{RT}{nFj_0 A^{wet}} \tag{2}$$

with gas constant R, absolute temperature T, number of transferred electrons n, Faraday constant F and exchange current density j_0. Substituting (1) into (2):

$$R_{CT}^{-1} = \frac{nFt_{DL}}{RT\epsilon_r\epsilon_0} j_0 C_{DL} \tag{3}$$

it is apparent that a plot of the inverse R_{CT} over C_{DL} will yield a slope directly proportional to j_0.

In the work presented herein, the kinetics of the V(II)/V(III) redox reaction at Bi-modified electrodes will be carefully evaluated before and after cycling in a battery tester. By following the aforementioned methodology, we can discriminate changes in wetting behavior from actual enhancement of kinetic properties.

2. Results and Discussion

2.1. Catalytic Activity of Bismuth

Carbon felt electrodes were modified with Bi_2O_3 by a simple impregnation route. This involved soaking felts in acidic bismuth nitrate solution, precipitating with ammonia and heat treatment at 300 °C under N_2-atmosphere (Bi-GFD). To relate any observed change in electrochemical activity for the V(II)/V(III) redox reaction only to the presence of bismuth and to rule out any influence of the applied acidic, alkaline and temperature conditions, further felts were prepared as a reference. Felts subjected to first acidic and then alkaline media were labeled as GFD-Ref, felts heat-treated afterwards as GFD-Ref-HT. Felts only heat-treated were labeled GFD-HT, while untreated felts are referred to as GFD-U.

Figure 1 shows scanning electron microscopy (SEM) images of untreated and Bi-modified felts. While for GFD-U (Figure 1a) the fibers exhibit a smooth surface, in the case of Bi-GFD (Figure 1b) they are covered by evenly distributed flakes. The energy dispersive X-ray (EDX) elemental mapping in Figure 1c as well as the according spectrum in Figure 1d clearly show the presence of bismuth in these particles [38]. The chosen impregnation route is therefore well suited for the preparation of Bi-modified carbon felt electrodes.
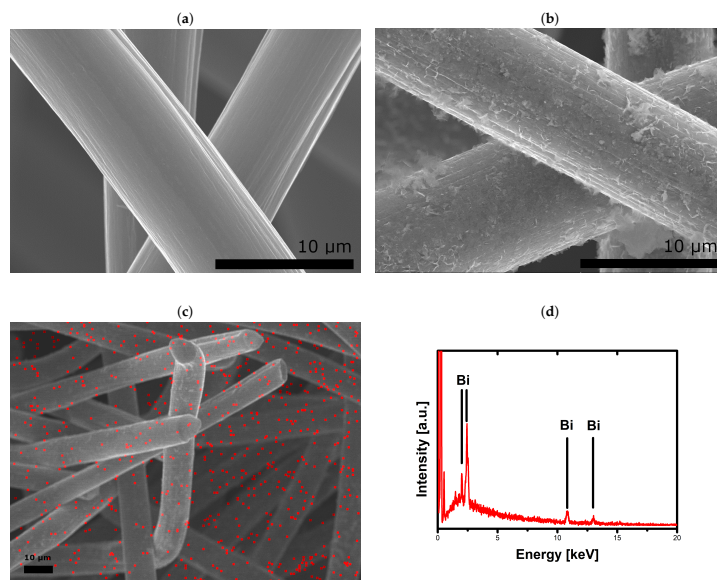

Figure 1. SEM images of fresh carbon felts: (**a**) untreated GFD-U, (**b**) bismuth-modified Bi-GFD and (**c**) elemental mapping for bismuth on Bi-GFD with (**d**) respective EDX spectrum.

Electrochemical activity of modified felt electrodes for the V(II)/V(III) redox reaction was evaluated by CV and EIS. Prior to each measurement, electrode samples have been wetted by

centrifugation to give reproducible results. Reproducibility was checked for GFD-U (results not shown). In the CV measurements (Figure 2a), Bi-GFD shows an enhanced activity compared to GFD-U, which manifests in reduced peak separation and increased peak currents. Also, no significant differences in the CV response of GFD-U and the reference felts GFD-Ref, GFD-Ref-HT and GFD-HT are observed. However, Nyquist plots in Figure 2b indicate enhanced performance not only for Bi-GFD, but (less pronounced) also for all samples subjected to any treatment procedure. This can be seen from reduced diameters of the displayed semicircles, which is similar to reduced R_{CT} values. As was pointed out earlier, a discussion of R_{CT} without taking into account the wetted surface area does not allow for a comparison of electrode kinetics. Since the EIS response of porous carbon electrodes is highly sensitive to any changes of the wetted surface area [34], it must be clarified, whether the displayed differences are due to altered wetting behavior or to altered kinetics. Therefore, EIS was conducted on electrode samples of varying size. In Figure 2c this is shown exemplarily for untreated samples (GFD-U). The diameters of the semicircles displayed in the Nyquist plot expectedly decrease with increasing sample diameter. EIS data were fitted in a frequency range between 10^4–1 Hz using a simple model, consisting of an ohmic resistance R_{ohm} connected in series to a parallel combination of charge transfer resistance R_{CT} and double layer capacity C_{DL}: $R_{ohm} - (R_{CT} | C_{DL})$. Following the aforementioned approach of Friedl and co-workers [35–37], the inverse R_{CT} was plotted over C_{DL} (Figure 2d). Fitting of the curves yields a linear relation for all samples under investigation. As was pointed out earlier, the slopes of the linear fits are direct measures for the exchange current density j_0. Barely any deviation of these slopes was observed for electrodes, which did not contain bismuth. This means that the differences observed in Figure 2b are solely due to changes in wetting behavior and not related to altered kinetic properties. In contrast to that, Bi-GFD shows a significantly higher slope compared to all other samples. This demonstrates not only the catalytic activity of bismuth for the V(II)/V(III) redox reaction, but also shows that any possible performance gains for bismuth-modified electrodes can be attributed exclusively to the presence of bismuth, not to treatment conditions during bismuth deposition.
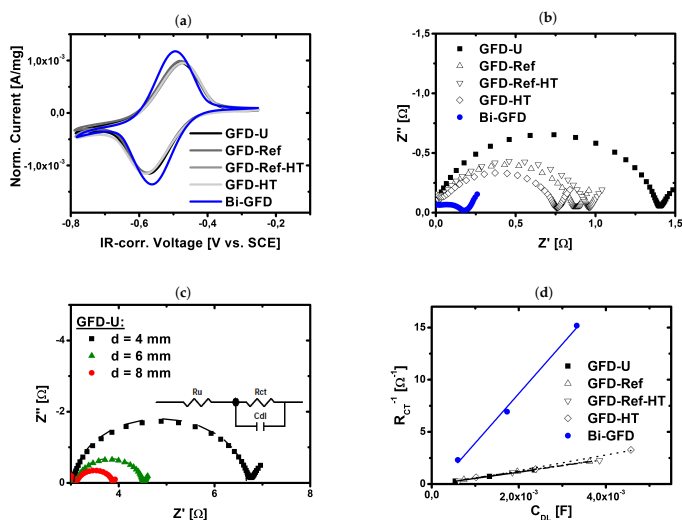
Figure 2. Measurements in three-electrode setup using differently modified carbon felt electrodes: (**a**) IR-corrected CV curves, given currents normalized by electrode weight; (**b**) Nyquist plots of modified carbon felts; (**c**) exemplary Nyquist plots of carbon felt with different diameters; (**d**) inverse charge transfer resistance plotted versus double layer capacity.

2.2. Charge/Discharge Cycling

To study the degradation behavior of bismuth-modified carbon felt electrodes under real working conditions, single cell battery charge/discharge cycling was performed. Cells employing either bismuth-modified (Bi-GFD) or untreated (GFD-U) felts as electrode at the negative half-cell have been cycled 50 times at a current density of 100 mA/cm^2 within the voltage limits of 1.65 V for charging and 0.8 V for discharging, respectively. Over the course of this experiment, in both cases a stable cell performance in terms of energy efficiency (EE) was obtained, as can be seen from Figure 3a. For Bi-GFD, a slightly higher EE (around 70%) was realized compared to GFD-U (around 66%). Also, the achieved capacities (Figure 3b) are permanently higher for Bi-GFD. Based on the results shown in the previous section, this had to be expected. Due to the catalytic activity of Bi, the overpotential for the V(II)/V(III) redox reaction is lowered, resulting in a wider SOC window being accessible during both charging and discharging, before the voltage limits are exceeded. However, over 50 cycles the capacity is fading in a similar fashion as for the cell employing GFD-U. Prior to and subsequent to the cycling, full cell EIS was conducted. The results are shown in Figure 3c. It is apparent that Bi-GFD shows lower impedance than GFD-U both before and after cycling. Fitting the data to a model $R_{ohm} - (R_{CT} \,|\, CPE)$ reveals a similar decrease in C_{DL} of around 38% for both cases (see Table 1). The increase in R_{CT} is also comparable while slightly less distinct for Bi-GFD (77%) than for GFD (88%).
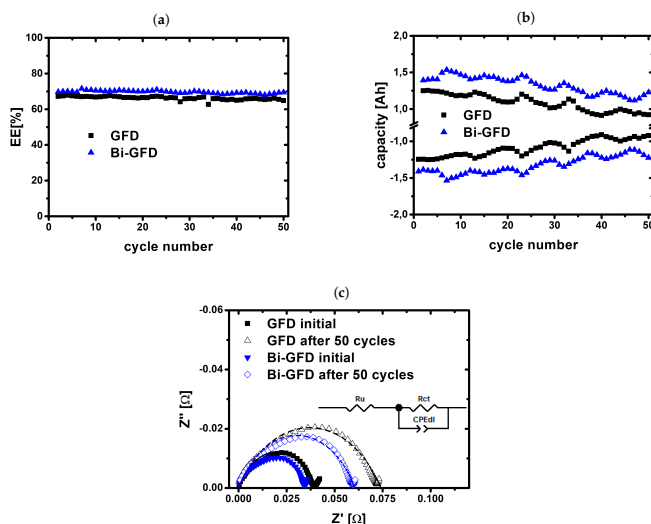
Figure 3. Results of charge/discharge cycling in a battery test system: (**a**) energy efficiency; (**b**) capacity over 50 cycles of charging and discharging at 100 mA cm^{-2}; (**c**) full cell EIS data before and after cycling.

Table 1. Full Cell EIS parameters before and after 50 charge/discharge cycles at 100 mA/cm^2. Values for C_{DL} were obtained by conversion of CPE parameters following Hirschorn et al. [39].

	R_{CT} (mΩ)	C_{DL} (mF)
GFD initial	40.9	5.37
GFD after 50 cycles	76.7	3.35
Bi-GFD initial	31.6	5.94
Bi-GFD after 50 cycles	55.8	3.69

These findings indicate that Bi-modification of carbon felt electrodes is not able to prevent electrode degradation, since the loss of active surface area, manifested in the loss of C_{DL}, is similar for both unmodified and bismuth-modified electrodes. Furthermore, a total reflection X-ray fluorescence (TXRF) spectroscopic investigation of the electrolyte gives strong evidence that bismuth is not stable on the fibers during cycling. After 50 cycles, the bismuth content of the electrolyte in the negative half-cell was determined to be 170 µg/L. It seems therefore very likely that a leaching of catalyst occurred throughout operation of the cell. The nevertheless stable cell performance is in good agreement with Li et al. [27], who found an enhancing effect already, when bismuth was added to the electrolyte.

2.3. Evaluation of Aged Electrodes

Following the cycling experiment, the used electrodes were again evaluated in a similar fashion as before cycling, to study the effect of electrode degradation on the kinetics of the V(II)/V(III) redox reaction in a three-electrode setup. While GFD shows a reduced performance, apparent from reduced peak currents in Figure 4a and a less steep slope in Figure 4b, Bi-GFD seems to be completely deactivated after cycling. The CV shows no apparent redox peaks for Bi-GFD-A and the according

kinetic slope practically equals 0. These results are to a certain extent surprising because even if the bismuth was removed from the fibers during cycling, as implicated by the TXRF results, a remaining performance at least comparable with that of GFD-U would have been expected. This being not the case indicates that a modification of carbon felt electrodes with bismuth may enhance kinetics if bismuth is present in the system, either on the electrode or at least in the electrolyte. However, on the other hand it seems likely that the presence of bismuth has a strong accelerating effect on the degradation of carbon fibers, leaving a completely deactivated electrode as soon as the bismuth is removed from the system. The SEM images in Figure 5 support this assumption. GFD-A (Figure 5a) shows agglomeration of material on the fiber surface with the overall fiber structure still being intact, whereas the fibers of Bi-GFD-A (exemplarily shown in Figure 5b,c) appear heavily corroded with the latter being so damaged that it appears to be split in half. To the best of our knowledge, this is the first time such phenomena have been observed for bismuth-modified electrodes in VRFB. Furthermore, in the EDX spectrum shown in Figure 5d no bismuth could be detected. Instead the spectrum shows peaks that can be attributed to vanadium, sulfur, and oxygen [38], which presumably originate from the electrolyte. The aluminum signal most probably originated from the used sample holder. However, since EDX is a local probe with bulk characteristics, no general conclusion can be drawn from this spectrum. Still, together with the TXRF results it supports the assumption that bismuth is not stable on the fibers during cycling. At the moment, the results presented herein cannot be explained. Further studies are needed to gain a deeper understanding of how the presence of bismuth affects the degradation of the carbon fibers.
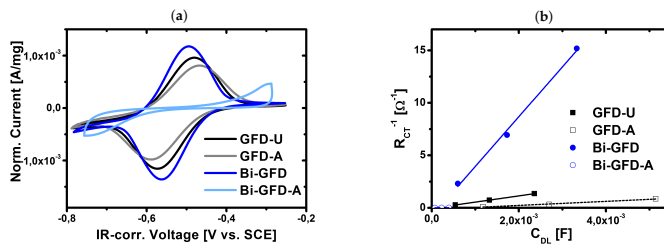

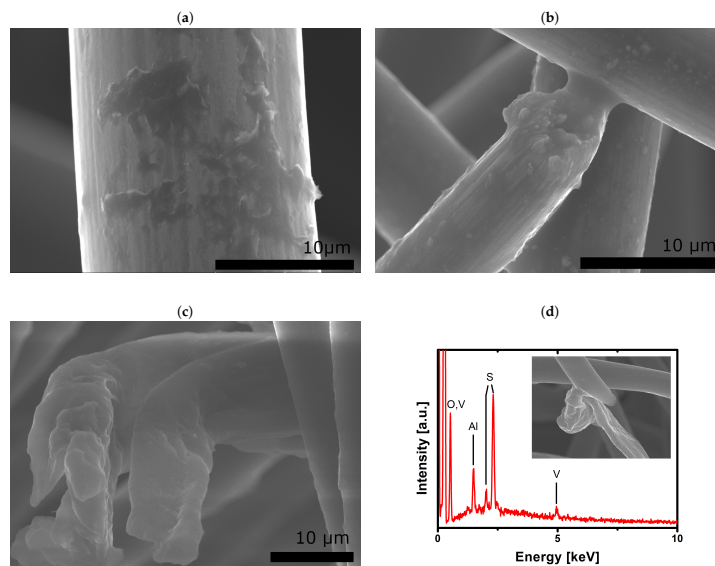**Figure 4.** Evaluation of aged electrodes in three-electrode setup: CV (**a**) and normalized EIS results (**b**).

Figure 5. SEM images of aged carbon felts: (**a**) unmodified GFD-A; (**b**,**c**) Bi-modified Bi-GFD-A; (**d**) EDX spectrum of Bi-GFD-A recorded at the spot shown in the inset.

3. Conclusions

In this study, carbon felt electrodes have been successfully modified with bismuth and studied in the negative half-cell reaction of VRFB. By a normalization of EIS results obtained in a three-electrode setup the catalytic properties of bismuth could be demonstrated. It was possible to attribute enhanced kinetic properties of modified electrodes to bismuth alone and to rule out any possible influence of the applied treatment methods. For the first time, bismuth-modified electrodes have been further subjected to electrochemical stress in a battery tester and afterwards evaluated again in a three-electrode setup. The results indicate that the presence of bismuth may have an accelerating effect on the degradation of carbon fibers even though the activity in the system tests was retained over 50 cycles. Further studies will be needed to explain these unexpected findings.

4. Materials and Methods

Unless otherwise stated, all chemicals were used as-received without any further purification.

4.1. Electrode Preparation

Carbon felts (GFD4.6; SGL Carbon, Meitingen, Germany) were immersed into a solution of 1 g Bismuth(III) nitrate hydrate (99.999% metals basis, Alfa Aesar, Heysham, UK) in 100 mL 5% acetic acid (Fisher Scientific, Loughborough, UK). After two days the soaked felts were removed and placed inside a 1 M aqueous solution of ammonium hydroxide (Carl Roth, Karlsruhe, Germany) for one more day. Subsequently, the impregnated felts were rinsed with deionized water (Merck Millipore, Darmstadt,

Germany), dried over night at 80 °C and finally heat-treated for 3 h at 300 °C under N_2-atmosphere to yield Bi-GFD.

For comparison, further felts underwent a similar preparation procedure, but without the presence of any bismuth salts: GFD-Ref (stored in 5% acetic acid for two days, then in 1 M ammonia for one day, no heat treatment), GFD-Ref-HT (like GFD-Ref, followed by heat treatment for 3 h at 300 °C), GFD-HT (pristine felt, heat-treated under aforementioned conditions). Untreated carbon felts were labeled as GFD-U.

4.2. Electrode Characterization

Surface morphology and composition of the samples have been probed using a HITACHI UHR FE-SEM SU8030 ultrahigh-resolution scanning electron microscope which was operating at 20 kV acceleration voltage and coupled with an EDX spectrometer.

Quantification of bismuth was done by TXRF spectroscopy using a BRUKER S2 PicoFox device. $Ga(NO_3)_3$ (Merck CertiPUR) was added to the sample as an internal standard. A drop of the mixture was applied to a silicon-coated quartz glass sample plate and allowed to dry before initiation of TXRF measurements.

4.3. Electrode Aging

Aging of electrodes was performed by subjecting them to prolonged charge/discharge cycling in a battery test system (857 Redox Flow Cell Test System; Scribner Associates, Southern Pines, NC, USA). A 10 cm^2 flow through Micro Flow Cell (Electrocell A/S, Tarm, Danmark), equipped with an anion exchange membrane (FAP 450; Fumatech, Bietigheim-Bissingen, Germany) and graphite plates (FU 4369 HT; Schunk Kohlenstofftechnik, Heuchelheim, Germany) as current collectors, was used. Electrodes employed at the positive side were GFD-U in all cases. At the negative side either GFD-U or Bi-GFD was used. Upon installation, the electrodes were compressed by 17%. 70 mL commercial 1.6 M vanadium electrolyte (batch-no: 207445; GfE Gesellschaft für Elektrometallurgie mbH, Nürnberg, Germany) per side were pumped at a flow-rate of 25 mL min^{-1}. A constant nitrogen flow was applied to keep the system under inert conditions. Cycling experiments were performed at a constant current density of 100 mA cm^{-2} within the voltage limits of 1.65 V and 0.8 V for charging and discharging, respectively. Each cell was charged and discharged 50 times. Before and after cycling, full cell electrochemical impedance measurements (EIS) were performed at an open circuit potential (OCP) of 1.4 V (corresponding to a SOC of 50% [40,41]), using a potentiostat Reference 3000 (Gamry Instruments, Warminster, PA, USA). An AC voltage of 10 mV was applied in a frequency range from 10^5–10^{-1} Hz.

Following a cycling experiment, the system was drained from electrolyte and washed with 3 M sulfuric acid (Carl Roth). The cell was then disassembled and the electrodes from the negative side were rinsed with deionized water and dried at 80 °C before further assessment in a three-electrode-setup (see below). Aged electrodes obtained this way were labeled as either GFD-A or Bi-GFD-A.

4.4. Three-Electrode Measurements

Measurements in three-electrode setup were performed using a Gamry Reference 600 potentiostat. The electrolyte was a 0.16 M V^{2+}/V^{3+} (SOC 50%) solution obtained by dilution of pre-charged commercial electrolyte with 2 M H_2SO_4. A Pt mesh served as counter electrode while a saturated calomel electrode (SCE) with a potential of +248 mV vs. SHE was used as reference electrode. Carbon felts of three different sizes were studied. From the samples of interest, pieces with 4, 6 or 8 mm diameter were punched out using appropriate punching irons. Prior to measurement, each felt was centrifuged in 5 mL electrolyte for 5 min at 9500 rotations per minute to ensure proper wetting. Afterwards the felt was contacted by piercing it with a glassy carbon (GC) rod and used as the working electrode. The setup was kept under N_2 atmosphere during all measurements.

CV measurements were performed at a scan rate of $1\,\mathrm{mV\,s^{-1}}$ within the scan limits of -0.3 and -0.8 V vs. SCE. Since no stable OCP could be reached, start and end potential were set to be -0.5 V vs. SCE. This is in good agreement with the expected OCP value of a 1:1-mixture of V^{2+} and V^{3+}. Typically, three cycles were measured, from which the second was analyzed.

In the same setup, potentiostatic EIS experiments were conducted in a frequency range of 10^5–10^{-1} Hz using an AC amplitude of 10 mV. The DC potential was set to be -0.5 V vs. SCE and the working electrode was conditioned at this potential for 5 min prior to the measurement.

Author Contributions: Conceptualization, J.S., I.D. and C.R.; Data curation, J.S.; Formal analysis, J.S. and G.A.E.-N.; Funding acquisition, C.R.; Investigation, J.S., E.B., G.A.E.-N., M.G. and P.K.; Methodology, J.S., M.S. and A.F.; Project administration, C.R.; Resources, C.R.; Supervision, C.R.; Validation, J.S.; Visualization, J.S.; Writing—original draft, J.S.; Writing—review & editing, C.R.

Conflicts of Interest: The authors declare no conflict of interest.

List of Symbols

The following symbols are used in this manuscript:

ϵ_0	permittivity of the free space
ϵ_r	relative dielectric permittivity
A^{wet}	wetted surface area
C_{DL}	double layer capacitance
F	Faraday constant
j_0	exchange current density
n	number of electrons
R	gas constant
R_{CT}	charge transfer resistance
T	absolute temperature
Z'	real part of the impedance
Z''	imaginary part of the impedance

References

1. Alotto, P.; Guarnieri, M.; Moro, F. Redox flow batteries for the storage of renewable energy: A review. *Renew. Sustain. Energy Rev.* **2014**, *29*, 325–335. [CrossRef]
2. Pan, F.; Wang, Q. Redox species of redox flow batteries: A review. *Molecules* **2015**, *20*, 20499–20517. [CrossRef] [PubMed]
3. Noack, J.; Roznyatovskaya, N.; Herr, T.; Fischer, P. The Chemistry of Redox-Flow Batteries. *Angew. Chem. Int. Ed.* **2015**, *54*, 9776–9809. [CrossRef]
4. Weber, A.Z.; Mench, M.M.; Meyers, J.P.; Ross, P.N.; Gostick, J.T.; Liu, Q. Redox flow batteries: A review. *J. Appl. Electrochem.* **2011**, *41*, 1137–1164. [CrossRef]
5. Skyllas-Kazacos, M. New All-Vanadium Redox Flow Cell. *J. Electrochem. Soc.* **1986**, *133*, 1057. [CrossRef]
6. Agar, E.; Dennison, C.R.; Knehr, K.W.; Kumbur, E.C. Identification of performance limiting electrode using asymmetric cell configuration in vanadium redox flow batteries. *J. Power Sources* **2013**, *225*, 89–94. [CrossRef]
7. Sun, C.N.; Delnick, F.M.; Aaron, D.S.; Papandrew, A.B.; Mench, M.M.; Zawodzinski, T.A. Probing Electrode Losses in All-Vanadium Redox Flow Batteries with Impedance Spectroscopy. *ECS Electrochem. Lett.* **2013**, *2*, A43–A45. [CrossRef]
8. Langner, J.; Melke, J.; Ehrenberg, H.; Roth, C. Determination of Overpotentials in All Vanadium Redox Flow Batteries. *ECS Trans.* **2014**, *58*, 1–7. [CrossRef]
9. Langner, J.; Bruns, M.; Dixon, D.; Nefedov, A.; Wöll, C.; Scheiba, F.; Ehrenberg, H.; Roth, C.; Melke, J. Surface properties and graphitization of polyacrylonitrile based fiber electrodes affecting the negative half-cell reaction in vanadium redox flow batteries. *J. Power Sources* **2016**, *321*, 210–218. [CrossRef]

10. Derr, I.; Bruns, M.; Langner, J.; Fetyan, A.; Melke, J.; Roth, C. Degradation of all-vanadium redox flow batteries (VRFB) investigated by electrochemical impedance and X-ray photoelectron spectroscopy: Part 2 electrochemical degradation. *J. Power Sources* **2016**, *325*, 351–359. [CrossRef]

11. Noack, J.N.; Vorhauser, L.; Pinkwart, K.; Tuebke, J. Aging Studies of Vanadium Redox Flow Batteries. *ECS Trans.* **2011**, *33*, 3–9. [CrossRef]

12. Pezeshki, A.M.; Sacci, R.L.; Veith, G.M.; Zawodzinski, T.A.; Mench, M.M. The Cell-in-Series Method: A Technique for Accelerated Electrode Degradation in Redox Flow Batteries. *J. Electrochem. Soc.* **2015**, *163*, A5202–A5210. [CrossRef]

13. Derr, I.; Fetyan, A.; Schutjajew, K.; Roth, C. Electrochemical analysis of the performance loss in all vanadium redox flow batteries using different cut-off voltages. *Electrochim. Acta* **2017**, *224*, 9–16. [CrossRef]

14. Derr, I.; Przyrembel, D.; Schweer, J.; Fetyan, A.; Langner, J.; Melke, J.; Weinelt, M.; Roth, C. Electroless chemical aging of carbon felt electrodes for the all-vanadium redox flow battery (VRFB) investigated by Electrochemical Impedance and X-ray Photoelectron Spectroscopy. *Electrochim. Acta* **2017**, *246*, 783–793. [CrossRef]

15. Nibel, O.; Taylor, S.M.; Pătru, A.; Fabbri, E.; Gubler, L.; Schmidt, T.J. Performance of Different Carbon Electrode Materials: Insights into Stability and Degradation under Real Vanadium Redox Flow Battery Operating Conditions. *J. Electrochem. Soc.* **2017**, *164*, A1608–A1615. [CrossRef]

16. Sun, C.N.; Delnick, F.M.; Baggetto, L.; Veith, G.M.; Zawodzinski, T.A., Jr. Hydrogen evolution at the negative electrode of the all-vanadium redox flow batteries. *J. Power Sources* **2014**, *248*, 560–564. [CrossRef]

17. Schweiss, R.; Pritzl, A.; Meiser, C. Parasitic Hydrogen Evolution at Different Carbon Fiber Electrodes in Vanadium Redox Flow Batteries. *J. Electrochem. Soc.* **2016**, *163*, A2089–A2094. [CrossRef]

18. Fetyan, A.; El-Nagar, G.A.; Lauermann, I.; Schnucklake, M.; Schneider, J.; Roth, C. Detrimental role of hydrogen evolution and its temperature-dependent impact on the performance of vanadium redox flow batteries. *J. Energy Chem.* **2018**. [CrossRef]

19. Park, M.; Ryu, J.; Cho, J. Nanostructured Electrocatalysts for All-Vanadium Redox Flow Batteries. *Chem. Asian J.* **2015**, *10*, 2096–2110. [CrossRef]

20. Zhou, H.; Xi, J.; Li, Z.; Zhang, Z.; Yu, L.; Liu, L.; Qiu, X.; Chen, L. CeO2 decorated graphite felt as a high-performance electrode for vanadium redox flow batteries. *RSC Adv.* **2014**, *4*, 61912–61918. [CrossRef]

21. Tseng, T.M.; Huang, R.H.; Huang, C.Y.; Hsueh, K.L.; Shieu, F.S. Improvement of titanium dioxide addition on carbon black composite for negative electrode in vanadium redox flow battery. *J. Electrochem. Soc.* **2013**, *160*, A1269–A1275. [CrossRef]

22. Tseng, T.M.; Huang, R.H.; Huang, C.Y.; Liu, C.C.; Hsueh, K.L.; Shieu, F.S. Carbon Felt Coated with Titanium Dioxide/Carbon Black Composite as Negative Electrode for Vanadium Redox Flow Battery. *J. Electrochem. Soc.* **2014**, *161*, A1132–A1138. [CrossRef]

23. Fetyan, A.; El-Nagar, G.A.; Derr, I.; Kubella, P.; Dau, H.; Roth, C. A neodymium oxide nanoparticle-doped carbon felt as promising electrode for vanadium redox flow batteries. *Electrochim. Acta* **2018**, *268*, 59–65. [CrossRef]

24. Shen, J.; Liu, S.; He, Z.; Shi, L. Influence of antimony ions in negative electrolyte on the electrochemical performance of vanadium redox flow batteries. *Electrochim. Acta* **2015**, *151*, 297–305. [CrossRef]

25. Li, B.; Gu, M.; Nie, Z.; Wei, X.; Wang, C.; Sprenkle, V.; Wang, W. Nanorod Niobium Oxide as Powerful Catalysts for an All Vanadium Redox Flow Battery. *Nano Lett.* **2014**, *14*, 158–165. [CrossRef] [PubMed]

26. Kim, M.; Yoo, H.; Lee, G.; Choi, J. Enhanced VRB electrochemical performance using tungsten as an electrolyte additive. *Electrochim. Acta* **2017**, *246*, 190–196. [CrossRef]

27. Li, B.; Gu, M.; Nie, Z.; Shao, Y.; Luo, Q.; Wei, X.; Li, X.; Xiao, J.; Wang, C.; Sprenkle, V.; Wang, W. Bismuth nanoparticle decorating graphite felt as a high-performance electrode for an all-vanadium redox flow battery. *Nano Lett.* **2013**, *13*, 1330–1335. [CrossRef]

28. Suarez, D.J.; Gonzalez, Z.; Blanco, C.; Granda, M.; Menendez, R.; Santamaria, R. Graphite Felt Modified with Bismuth Nanoparticles as Negative Electrode in a Vanadium Redox Flow Battery. *ChemSusChem* **2014**, *7*, 914–918. [CrossRef]

29. Liu, T.; Li, X.; Nie, H.; Xu, C.; Zhang, H. Investigation on the effect of catalyst on the electrochemical performance of carbon felt and graphite felt for vanadium flow batteries. *J. Power Sources* **2015**, *286*, 73–81. [CrossRef]

30. Wei, G.; Fan, X.; Liu, J.; Yan, C. Electrospun carbon nanofibers/electrocatalyst hybrids as asymmetric electrodes for vanadium redox flow battery. *J. Power Sources* **2015**, *281*, 1–6. [CrossRef]

31. Lv, Y.; Zhang, J.; Lv, Z.; Wu, C.; Liu, Y.; Wang, H.; Lu, S.; Xiang, Y. Enhanced electrochemical activity of carbon felt for V 2+ /V 3+ redox reaction via combining KOH-etched pretreatment with uniform deposition of Bi nanoparticles. *Electrochim. Acta* **2017**, *253*, 78–84. [CrossRef]

32. Yang, X.; Liu, T.; Xu, C.; Zhang, H.; Li, X.; Zhang, H. The catalytic effect of bismuth for VO 2 + /VO 2+ and V 3+ /V 2+ redox couples in vanadium flow batteries. *J. Energy Chem.* **2017**, *26*, 1–7. [CrossRef]

33. Liu, Y.; Liang, F.; Zhao, Y.; Yu, L.; Liu, L.; Xi, J. Broad temperature adaptability of vanadium redox flow battery–part 4: Unraveling wide temperature promotion mechanism of bismuth for V 2+ /V 3+ couple. *J. Energy Chem.* **2018**. [CrossRef]

34. Goulet, M.A.; Skyllas-Kazacos, M.; Kjeang, E. The importance of wetting in carbon paper electrodes for vanadium redox reactions. *Carbon* **2016**, *101*, 390–398. [CrossRef]

35. Friedl, J.; Bauer, C.M.; Rinaldi, A.; Stimming, U. Electron transfer kinetics of the – Reaction on multi-walled carbon nanotubes. *Carbon* **2013**, *63*, 228–239. [CrossRef]

36. Fink, H.; Friedl, J.; Stimming, U. Composition of the Electrode Determines Which Half-Cell's Rate Constant is Higher in a Vanadium Flow Battery. *J. Phys. Chem. C* **2016**, *120*, 15893–15901. [CrossRef]

37. Friedl, J.; Stimming, U. Determining Electron Transfer Kinetics at Porous Electrodes. *Electrochim. Acta* **2017**, *227*, 235–245. [CrossRef]

38. Bruker. *Periodic Table of Elements and X-ray Energies*; Bruker: Billerica, MA, USA, 2018.

39. Hirschorn, B.; Orazem, M.E.; Tribollet, B.; Vivier, V.; Frateur, I.; Musiani, M. Determination of effective capacitance and film thickness from constant-phase-element parameters. *Electrochim. Acta* **2010**, *55*, 6218–6227. [CrossRef]

40. Wei, Z.; Lim, T.M.; Skyllas-Kazacos, M.; Wai, N.; Tseng, K.J. Online state of charge and model parameter co-estimation based on a novel multi-timescale estimator for vanadium redox flow battery. *Appl. Energy* **2016**, *172*, 169–179. [CrossRef]

41. Wei, Z.; Tseng, K.J.; Wai, N.; Lim, T.M.; Skyllas-Kazacos, M. Adaptive estimation of state of charge and capacity with online identified battery model for vanadium redox flow battery. *J. Power Sources* **2016**, *332*, 389–398. [CrossRef]

Deconvolution of electrochemical impedance data for the monitoring of electrode degradation in VRFB

J. Schneider [1,*] , T. Tichter [1] , P. Khadke [2] , R. Zeis [3] , C. Roth [2]

[1] Institute of Chemistry and Biochemistry, Freie Universität Berlin, Arnimallee 22, 14195, Berlin, Germany
[2] Electrochemical Process Engineering, Universität Bayreuth, Universitätsstraße 30, 95447, Bayreuth, Germany
[3] Helmholtz-Institut Ulm, Helmholtzstr. 11, D-89081, Ulm, Germany
* corresponding author: J. Schneider

Author	Individual contributions
J. Schneider	Conceptualization, Methodology, Software, Validation, Formal Analysis, Investigation, Data Curation, Writing - Original Draft, Writing - Editing and Review, Visualization
T. Tichter	Software, Validation, Writing - Editing and Review
P. Khadke	Validation, Writing - Editing and Review
R. Zeis	Conceptualization, Methodology, Writing - Editing and Review
C. Roth	Conceptualization, Resources, Writing - Editing and Review, Supervision, Project Administration, Funding Acquisition

Deconvolution of electrochemical impedance data for the monitoring of electrode degradation in VRFB

Jonathan Schneider [a, *], Tim Tichter [a], Prashant Khadke [b], Roswitha Zeis [c], Christina Roth [b]

[a] Institute for Chemistry and Biochemistry, Freie Universität Berlin, Takustr. 3, D-14195, Berlin, Germany
[b] Chair of Materials Processing, Universität Bayreuth, Universitätsstr. 30, D-95447, Bayreuth, Germany
[c] Helmholtz-Institut Ulm, Helmholtzstr. 11, D-89081, Ulm, Germany

ABSTRACT

Understanding degradation phenomena occurring during the operation of vanadium redox-flow batteries (VRFB) requires a measurement technique which allows for differentiating the overall performance losses into individual performance losses of the cell components. For this purpose, electrochemical impedance spectroscopy (EIS) is a valuable and well established tool. However, the discrimination of processes taking place at similar time scales is challenging since they overlap in the commonly used Nyquist or Bode representation. Distribution of relaxation times (DRT) analysis tackles this issue by deconvoluting EIS data with respect to the time constants of the individual processes. It hence circumvents the necessity of finding a suitable equivalent circuit model and thus allows for data evaluation without any a-priori knowledge of the system under study. For the first time, we herein present the application of DRT transform to EIS data of a VRFB. By varying experimental conditions and employing full cell as well as double half cell operational modes, we are able to identify the faradaic process of the negative half cell. This enables us to visualize the negative half cell's contribution to the overall impedance of a VRFB even in a full cell EIS measurement. By an accelerated degradation experiment we finally demonstrate the great potential of DRT analysis for future application in the monitoring of electrode degradation in VRFB.

© 2020 Elsevier Ltd. All rights reserved.

1. Introduction

Widespread use and deep market penetration of the vanadium redox-flow battery (VRFB) are impeded by the required large capital cost. Whether or not an appealing business plan can be established critically depends on the predicted lifetime of the system. Such estimation of a battery's durability is only possible if the degradation phenomena occurring during operation are well understood. Therefore, the analysis of performance losses in VRFB is attracting a growing research interest. Recent studies have shown that besides ion crossover through the membrane, causing self-discharge and therefore capacity loss, also electrode degradation has to be taken into account [1–8], especially in the negative half cell. Since the V(II)/V(III) redox reaction is highly susceptible to changes in the electrode's surface composition [9–12], it is expected to be strongly affected by electrode degradation. In the long term, this will result in the parasitic hydrogen evolution reaction (HER) becoming kinetically favoured over the reduction of V^{3+} during the charging process [13–15], which will lead to an irreversible capacity loss.

However, at present, the tracking and quantification of electrode degradation is an elaborate process that mostly relies on ex-situ techniques, such as post-mortem X-ray photoelectron spectroscopy (XPS) which can give quite contradictory results [1,4]. On the other hand, in-situ electrochemical measurements, like electrochemical impedance spectroscopy (EIS), can only yield superimposed information about the two half cell electrodes, if no reference electrodes are incorporated into the measurement setup. The use of reference electrodes, however, is not favorable, since it is known to be the source of distortion and artifacts in the high frequency range [16,17].

One possible way to overcome these shortcomings could be the analysis of EIS data in terms of a distribution of relaxation times (DRT). This approach has already been proposed in the 1950s for the analysis of conductive systems [18] and can be interpreted as fitting experimental data to a generalized model made up of a

* Corresponding author.
E-mail address: jonathan.schneider@fu-berlin.de (J. Schneider).

series connection of an arbitrary number of RC-elements (a resistor R and a capacitor C connected in parallel). It could be shown, that such a "measurement model" is able to represent any electrochemical system without inductive behaviour [19,20]. Defining the infinite series connection of RC-elements with relaxation time constant $\tau = R*C$ gives rise to the following fredholm integral-equation of the second kind:

$$Z(\omega) = R_\infty + R_{pol} \int_0^\infty \frac{\gamma(\tau)}{1 + j\omega\tau} d\tau \qquad (1)$$

where ω is the angular frequency, $Z(\omega)$ the experimental dataset, R_∞ the ohmic resistance, R_{pol} the polarization resistance, and $\gamma(\tau)$ the desired DRT-function. Since fitting Eq. (1) to experimental data is a mathematically ill-posed problem, proper regularization of the fit is required in order to obtain physically relevant results. To account for this, a lot of methods are at hand, namely fourier transform [21,22], tikhonov regularization [23–27], maximum entropy [28,29], evolutionary programming [30,31], and the recently introduced m(RQ)-fit [32–34]. A comparison of results obtained by m(RQ)-fit, tikhonov regularization and fourier transform can be found here [35]. For details on these methods the reader is kindly referred to the respective literature, since discussing these would be beyond the scope of this article.

A number of free software solutions for calculation of DRT are available, like *LEVM* [36–38], *DRTtools* [25], *EC-idea* [39] or *Polarographica* [40,41]. The DRT feature implemented in the commercial software *Relaxis* can also be used online for free [42].

Up to now, DRT analysis has found widespread application in the characterisation of electrode materials in solide-oxide fuel cells (SOFC) [22,43–47], lithium-ion batteries [48–51] and proton exchange membrane fuel cells (PEM-FC) [52,53]. However, to the best of our knowledge, there is no study available using DRT analysis in the field of RFB research. We herein present the first application of this concept to the impedance spectrum of a single cell VRFB. We will show that by proper variation of experimental conditions the limiting processes in the battery can be identified unambiguously and we will further explore the suitability of DRT analysis for future use as an online tool for monitoring of degradation processes in VRFB.

2. Experimental

2.1. Measurement setup

Within the present study, two different flow-through cells have been utilized: a) a custom built cell with an active geometrical area of 4cm^2 and b) a commercially available 10cm^2 Micro Flow Cell (Electrocell A/S, Tarm, DK). Both cells have been loaded with GFD 4.6 carbon felt electrodes (SGL Carbon, Meitingen, D) and FAP 450 anion exchange membrane (Fumatech, Bietigheim-Bissingen, D), while graphite plates served as current collectors. As electrolyte, 150 ml of a commercial 1.6 M vanadium solution in 2 M H$_2$SO$_4$/0.015 M H$_3$PO$_4$ (GfE Gesellschaft für Elektrometallurgie mbH, Nürnberg, D) per tank was used. All measurements shown in this work have been conducted at the 4cm^2 cell. Unless otherwise stated, the volumetric flow rate used during experiments was 10 ml/min. With a cross-sectional (geometrical) electrode surface area of 0.8cm^2 this corresponds to a mean linear flow velocity of 0.208 cm/s past the electrode surface.

Full cell galvanostatic EIS measurements were performed at an open circuit potential (OCP) of 1.4 V, corresponding to a state of charge (SOC) of 50%, using a potentiostat/galvanostat Reference 3000 (Gamry Instruments, Warminster, USA). An ac amplitude of

50 mA was applied in a frequency range of 10^5–10^{-2} Hz with ten points per frequency decade. The dc offset was either chosen to be zero or varied between 100, 200, 400 and 600 mA, as specified in the respective figures. The 4cm^2 cell was either used in full cell or symmetrical cell (double half cell) operation, as shown in Fig. 1. Since in a symmetrical cell the same electrolyte (either V^{2+}/V^{3+}or VO^{2+}/VO$_2^+$) is circulated through both half cells, this setup enables studying the respective half cell reactions without the need to incorporate additional reference electrodes [54–59]. Furthermore, the SOC will remain constant, since the forward reaction in one half cell is directly reversed in the other half cell.

The second cell was connected in series to the first cell and operated using an 857 Redox Flow Cell Test System (Scribner Associates, Southern Pines, USA). Its purpose was to set and maintain a constant SOC. Consequently, it was used for the initial charging of the electrolyte and to recharge (or redischarge) after full cell EIS measurements with dc offset > 0 mA. Throughout all EIS measurements in the first cell, the second cell was kept at open circuit.

Furthermore, the second cell was used as a "counter-cell" to perform accelerated stress test (AST) experiments as have been suggested by *Pezeshki* et al. [5]. During AST, the first cell was constantly charging at $I_{charge} = 0.4$ A, corresponding to a current density of $j = 100$mA/cm^2, while the second cell was kept at a discharging current of $I_{discharge} = -I_{charge}$ to maintain a constant overall SOC of 95%.

2.2. Data pretreatment

As DRT analysis requires linearity and time-invariance of the measured EIS data to provide meaningful results, data quality has been checked using linear kramers-kronig transform [60]. Here, the imaginary part of the impedance will be calculated from the real part and vice versa. Stated criteria are assumed to be fulfilled, if the relative residuals between calculated and measured values are below 1%. A typical result of such a test is shown in Fig. 2. In the case of experiments with dc bias larger residuals have been observed in the low frequency range. Here, all spectra have been cut off at 20 Hz and only frequencies > 20 Hz have been analysed by DRT.

2.3. Calculation of DRT

DRT calculations have been performed using a custom python script based on the free Matlab application *DRTtools* [25]. In principle, tikhonov regularization is employed to fit discrete experimental datasets to Eq. (1) in a non-negative least-squares (NNLS) fashion. By incorporation of radial-basis functions (RBF), a continous distribution function can be obtained. Fitting was performed using the real part of the impedance with a regularization parameter of $\lambda = 0.001$ and a gaussian RBF with a FWHM of $\varepsilon = 2.5$.
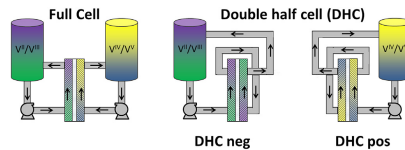

Fig. 1. Illustration of the operational modes used in this work: full cell operation (left) and the two symmetrical cell modes.
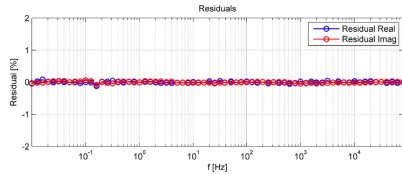
Fig. 2. Data quality assessment using linear kramers-kronig transform.

3. Results and discussion

3.1. Identification of individual half cell processes

In the first instance, the impedance spectrum of a single full cell VRFB has been analysed. As presented in Fig. 3, several peaks are obtained in the DRT representation, which can be categorized according to their time constants τ. Since in impedance spectroscopy data is usually analysed in terms of frequency-dependence, it appears more convenient to also discuss our results with respect to characteristic frequencies f_{char} rather than time constants. With $f_{char} = \frac{1}{2*\pi*\tau}$, we obtained five peaks (P1-5) located in the following four frequency regions: $f_{char,1} > 10$ kHz, 3 kHz $> f_{char,2} > 1$ kHz, 500 Hz $> f_{char,3} > 100$ Hz and $f_{char,4}, f_{char,5} < 100$ Hz. The last two peaks (P4 and P5) are summarized in the same frequency region since we assign them to the same process as will be explained in the following. It is to be expected that the flow rate of a VRFB will only affect the diffusional impedance Z_{Diff}, but neither the charge transfer (R_{CT}), nor the ohmic resistance R_∞ [56]. The occurrence of more than one peak related to mass transport could as well be foreseen, since the DRT of a Warburg element, which is usually used to model Z_{Diff}, should consist of a series of δ-functions, as was derived lately [34]. As Fig. 3 shows, an increase in flow rate leaves peaks 1−3 unaffected, while P4 and P5 are shifted to higher frequencies and also the peak height of P5 is reduced. We therefore attribute both P4 and P5 to mass transport. However, in the following sections we will focus more strongly on the frequency range above 100 Hz, since mass transport in VRFB is
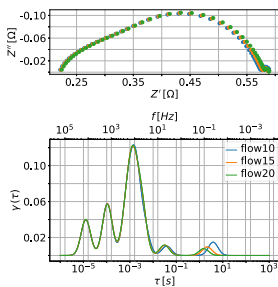
not expected to be changed significantly by electrode degradation.

In our understanding, electrode degradation is best described by a loss in the intrinsic kinetic activity of the electrodes over time. These phenomena should consequently manifest in the behaviour of the R_{CT} measured by EIS. In order to visualize this, we need to focus on the assignment of the peaks P1-3 at frequencies > 100 Hz. To investigate whether one or more of these peaks can be attributed solely to one half cell, we compared our full cell data to EIS results obtained in symmetric double half cell configuration. In this operational mode, only a solution of either V^{2+}/V^{3+}("DHC neg") or VO^{2+}/VO_2^+("DHC pos") is passed through both half cells. This approach has been shown to be very useful for selectively studying only one half cell reaction without having to install reference electrodes [54−59]. Another advantage is that the state of charge (SOC) will remain constant during the experiments, since one half cell reaction is reversed in the other half cell. In Fig. 4 the results of the two double half cell configurations are compared to full cell data. The SOC of the employed electrolyte solutions was 50% in all cases. From the Nyquist plot it can be seen that for DHC neg the impedance is significantly higher than for the other two operational modes. This supports recent studies which identified the negative half cell's electrode as the major source of performance limitation in the full cell [61−63]. Besides that, the DHC pos shows two interesting properties: a) a comparatively high ohmic resistance, as will be discussed in more detail below, and b) the absence of the peak P3 between $500 - 100$ Hz. Consequently, we assign this peak exclusively to a process occurring in the negative half cell.

3.2. Identification of faradaic processes

Considering the previously discussed results, we are able to demonstrate that DRT analysis allows to identify a specific process in the negative half cell. However, at this stage no assumptions can be made about the nature of this process. To provide information on the electrode's kinetic properties and to discuss degradation in terms of a change in these properties, all peaks related to charge transfer processes have to be identified. For that reason we conducted further EIS measurements in symmetrical cell operation at an increasing dc bias. According to Ref. [57], one would expect a progressive mitigation of any R_{CT} contribution caused by such increase.

In fact, this is exactly what is displayed in Fig. 5a. A clear trend can be observed for P3 in the negative double half cell, as this peak's

Fig. 3. Full cell EIS data at different electrolyte flow rates: Nyquist plot (top) and DRT representation (bottom). Flow rates are given in ml/min and correspond to mean linear flow velocities of 0.208/0.313/0.417 cm/s past the electrode surface. EIS measured without dc offset.
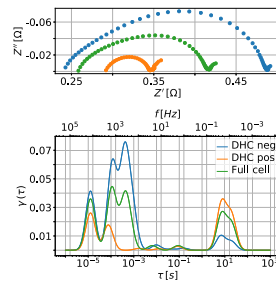

Fig. 4. Comparison of full cell and double half cell operation: Nyquist plot (top) and DRT representation (bottom). SOC was 50% in all cases, no dc offset applied.
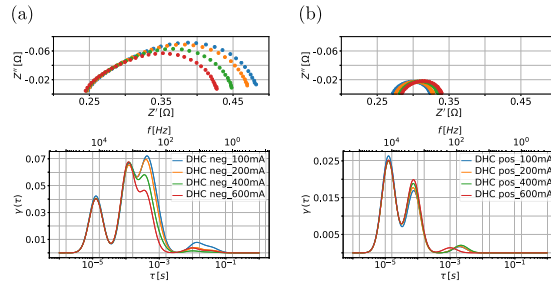
Fig. 5. Impedance of symmetrical cell configurations under applied dc bias - Nyquist plot (top) and DRT representation (bottom). All measurements were conducted at 1.6 M total vanadium concentration, 1:1 mixture of (a) V^{2+}/V^{3+}- "DHC neg" and (b) VO^{2+}/VO_2^+- "DHC pos". Applied dc offsets of 100/200/400/600 mA correspond to current densities of 25/50/100 and 150 mA/cm^2.

height behaves inversely proportional to the applied dc bias. This indicates that P3 can be attributed to the charge transfer process in the negative half cell. Since this peak is not present in DHC pos, by following its evolution, degradation of the negative half cell's electrode can be studied by full cell EIS measurements and subsequent DRT analysis, as will be demonstrated in the next section. On the other hand, no such trend can be observed in DHC pos (Fig. 5b). Here, a decrease in dc bias only leads to an increased R_∞, while the overall polarization resistance remains constant. At the same time, an increase in P2 (3 kHz > $f_{char,2}$ > 1 kHz) is detected in the DRT representation. Since with increasing dc bias this peak shows the same trend as the R_∞, we suppose, it is related to membrane behaviour. While studying the so-called "power drop effect", *Bhattarai* et al. found that anion exchange membranes, like the one used in our present work, will cause the R_∞ to rise with higher concentrations of V(V) [64]. The authors attributed this behaviour to the formation of anionic V(V)-complexes which will block the ion conducting channels of the membrane. With an increased dc bias during EIS measurements more V(V) will be formed over the course of the experiment, which could explain the behaviour of the R_∞ in DHC pos. The displayed trend of P2 is a strong indication for a correlation between this peak and a process occurring at the membrane. To the best of our knowledge, this is the first time ever reported that the membrane shows a contribution to the impedance of a VRFB different from a purely ohmic resistance. Consequently, DRT analysis might also enable the study of membrane degradation in VRFB from single cell EIS measurements in the future. In a recent study, *Reshetenko and Kulikovsky* found that the displayed high frequency impedance features of low-Pt PEM fuel cells are best described by incorporating an "external" capacitance into the model [65]. They argue, that this capacitance represents an electric double layer formed at the carbon/Nafion and carbon/water interface. In the same line of argument, we herein propose the formation of a charge double layer at the membrane/electrode interface in VRFB. Based on this assumption, the trend shown in Fig. 5b can be explained: higher concentrations of V(V) lead to an increased blocking of the membrane channels. This will on one hand cause a rise in R_∞ but on the other hand also a lower capacitance of the interfacial double layer at the membrane. Since a capacitance behaves inversely proportional to its associated impedance, P2 will be enhanced. Due to the absence of blocking vanadium species in DHC neg, no change in R_∞ or capacitance of the membrane/electrode double layer can be observed. Therefore,

P2 is not affected by the increasing dc offset in Fig. 5a.

However, still one peak has remained unassigned so far - the peak P1 at $f > 10$ kHz. By studying the impedance of a symmetrical cell fed with V^{2+}/V^{3+} electrolyte, *Pezeshki* et al. have encountered a feature in the high frequency range that became more distinct for increased thickness of the porous electrode or lower total concentration of vanadium [57]. This so-called distributed ohmic resistance is known to arise from the porous nature of the electrode [66] and can be explained by the interplay of ionic and electronic resistances in solution and solid electrode, respectively [67]. Since for P1 neither peak position, nor height have been significantly sensitive to varied flow conditions (Fig. 3) or applied dc bias (Fig. 5), but to electrolyte composition (Fig. 4), we finally assign this peak to the distributed ohmic resistance of the porous electrodes. Table 1 summarizes all peaks identified by DRT analysis of single cell VRFB impedance spectra. Note, that based on the current results no peak could be attributed to the charge-transfer process of the positive half-cell. Apparently, due to the very fast kinetics of this reaction, it becomes entirely controlled by mass transport at the flow rates used within this study. Further investigations should therefore focus on the influence of mass transport on the impedance of the positive half cell.

3.3. Accelerated stress test

To demonstrate the power of DRT analysis for monitoring electrode degradation, we conducted an accelerated stress test (AST) using a cell-in-series setup as suggested by *Pezeshki* et al. [5]. In this setup, the first cell was constantly charging for two days at a current density of 100mA/cm^2, while a second cell with a much larger geometrical electrode area, connected in series in terms of electrolyte flow, was discharging to maintain an overall SOC of 95%.

Consistency of the SOC is verified by measurement of the OCP before and after the experiment, as depicted in Fig. 6. Before and

Table 1
DRT analysis of a single cell VRFB: Observed peaks and preliminary assignment.

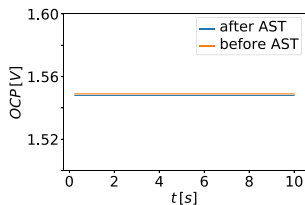| peak	frequency range	assignment
P1	> 10 kHz	distributed ohmic resistance
P2	3 − 1 kHz	anion exchange membrane
P3	500 − 100 Hz	negative half cell kinetics
P4, P5	< 100 Hz	mass transport

Fig. 6. Open circuit potential measured before and after AST, confirming a constant SOC.
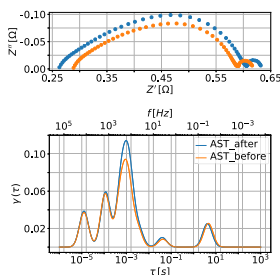

Fig. 7. Full cell impedance before and after AST experiment: Nyquist plot (top) and DRT (bottom). No dc offset applied during EIS measurement.

after this AST, full cell EIS of the first cell was measured at the OCP without dc bias. Since the surface composition of the employed carbon felts is supposed to change throughout such an experiment and the V(II)/V(III) redox reaction is highly susceptible to these changes [9–12], we expect the peak P3 to be strongly affected by AST.

As Fig. 7 shows, P3 is in fact the only peak that shows any significant growth. We have hereby demonstrated that the initial performance limitation arising from the kinetics of the V(II)/V(III) redox reaction is even further aggravated by electrode degradation in the negative half cell. These results underline the significance of studying electrode degradation in the context of performance losses in VRFB.

4. Conclusion and outlook

For the first time, DRT analysis has been applied to EIS data of a single cell VRFB. Our findings can be summarized as follows:

- Apparent peaks in the DRT representation can be attributed to distributed ohmic resistance of the porous electrodes, ion conductivity of the anion exchange membrane, charge-transfer kinetics of the negative half cell reaction and mass transport.
- While the positive half is controlled by mass transport, impedance in the negative half cell is dominated by the kinetics of the V(II)/V(III) redox reaction which appears to be a major source of performance limitation of the full cell.

- This limitation will be aggravated by electrode degradation, as has been demonstrated by a 2 days AST.
- DRT analysis has shown great potential for future use in monitoring degradation processes of the negative half cell electrode and anion exchange membrane from full cell EIS measurements.

Finally, we would like to stress the practical benefits DRT analysis could offer for large-scale, industrial applications of VRFB and other types of RFB as well. This method is easy to implement with nearly no investment cost since it relies on standard equipment that is already present. Required software tools are available under open source licences, meaning they can be easily adapted to specific demands and integrated into existing stack control systems. Time constants for mass transport can be obtained during operation, which will help in optimizing stack design. Given that all unit cells of a stack are accessible for separate electrical contact, flow distributions might as well be obtained directly by EIS measurements and the state-of-health of the different electrodes and membranes could be probed. A real-time monitoring based on EIS/DRT during operation might be challenging, given the time needed to obtain a full spectrum using the frequency sweep of a "classical" EIS experiment. However, this issue could be tackled by conducting measurements in the time domain and thereby reducing acquisition time to few seconds.

CRediT author statement

Jonathan Schneider: Conceptualization, Methodology, Software, Validation, Formal Analysis, Investigation, Data Curation, Writing — Original Draft, Writing — Editing and Review, Visualization. Tim Tichter: Software, Validation, Writing — Editing and Review. Prashant Khadke: Validation, Writing — Editing and Review. Roswitha Zeis: Conceptualization, Methodology, Writing — Editing and Review. Christina Roth: Conceptualization, Resources, Writing — Editing and Review, Supervision, Project Administration, Funding Acquisition.

References

[1] I. Derr, M. Bruns, J. Langner, A. Fetyan, J. Melke, C. Roth, Degradation of all-vanadium redox flow batteries (VRFB) investigated by electrochemical impedance and x-ray photoelectron spectroscopy: part 2 electrochemical degradation, J. Power Sources 325 (2016) 351–359, https://doi.org/10.1016/j.jpowsour.2016.06.040.

[2] I. Derr, A. Fetyan, K. Schutjajew, C. Roth, Electrochemical analysis of the performance loss in all vanadium redox flow batteries using different cut-off voltages, Electrochim. Acta 224 (2017) 9–16, https://doi.org/10.1016/j.electacta.2016.12.043.

[3] I. Derr, D. Przyrembel, J. Schweer, A. Fetyan, J. Langner, J. Melke, M. Weinelt, C. Roth, Electroless chemical aging of carbon felt electrodes for the all-vanadium redox flow battery (VRFB) investigated by electrochemical impedance and x-ray photoelectron spectroscopy, Electrochim. Acta 246 (2017) 783–793, https://doi.org/10.1016/j.electacta.2017.06.050.

[4] O. Nibel, S.M. Taylor, A. Pătru, E. Fabbri, L. Gubler, T.J. Schmidt, Performance of different carbon electrode materials: insights into stability and degradation under real vanadium redox flow battery operating conditions, J. Electrochem. Soc. 164 (7) (2017) A1608–A1615, https://doi.org/10.1149/2.1081707jes.

[5] A.M. Pezeshki, R.L. Sacci, G.M. Veith, T.A. Zawodzinski, M.M. Mench, The cell-in-series method: a technique for accelerated electrode degradation in redox flow batteries, J. Electrochem. Soc. 163 (1) (2015) A5202–A5210, https://doi.org/10.1149/2.0251601jes.

[6] J. Schneider, E. Bulczak, G.A. El-Nagar, M. Gebhard, P. Kubella, M. Schnucklake, A. Fetyan, I. Derr, C. Roth, Degradation phenomena of bismuth-modified felt electrodes in vrfb studied by electrochemical impedance spectroscopy, Batteries 5 (1) (2019) 16, https://doi.org/10.3390/batteries5010016.

[7] C. Choi, S. Kim, R. Kim, J. Lee, J. Heo, H.-T. Kim, In-situ observation of the degradation of all-vanadium redox flow batteries with dynamic hydrogen reference electrode under real operation conditions, J. Ind. Eng. Chem. 70 (2019) 355–362, https://doi.org/10.1016/j.jiec.2018.10.036. Amsterdam, Netherlands.

[8] M. Nourani, B.I. Zackin, D.C. Sabarirajan, R. Taspinar, K. Artyushkova, F. Liu, I.V. Zenyuk, E. Agar, Impact of corrosion conditions on carbon paper electrode morphology and the performance of a vanadium redox flow battery, J. Electrochem. Soc. 166 (2) (2019) A353–A363, https://doi.org/10.1149/2.1041902jes.

[9] P. Chen, M.A. Fryling, R.L. McCreery, Electron transfer kinetics at modified carbon electrode surfaces: the role of specific surface sites, Anal. Chem. 67 (18) (1995) 3115–3122, https://doi.org/10.1021/ac00114a004.

[10] A. Bourke, M.A. Miller, R.P. Lynch, J.S. Wainright, R.F. Savinell, D.N. Buckley, Effect of cathodic and anodic treatments of carbon on the electrode kinetics of V^{IV}/V^V oxidation-reduction, J. Electrochem. Soc. 162 (8) (2015) A1547–A1555, https://doi.org/10.1149/2.0671508jes.

[11] A. Bourke, M.A. Miller, R.P. Lynch, X. Gao, J. Landon, J.S. Wainright, R.F. Savinell, D.N. Buckley, Electrode kinetics of vanadium flow batteries: contrasting responses of V^{II}-V^{III} and V^{IV}-V^V to electrochemical pretreatment of carbon, J. Electrochem. Soc. 163 (1) (2016) A5097–A5105, https://doi.org/10.1149/2.0131601jes.

[12] H. Fink, J. Friedl, U. Stimming, Composition of the electrode determines which half-cell's rate constant is higher in a vanadium flow battery, J. Phys. Chem. C 120 (29) (2016) 15893–15901, https://doi.org/10.1021/acs.jpcc.5b12098.

[13] C.-N. Sun, F.M. Delnick, L. Baggetto, G.M. Veith, Zawodzinski, A. Thomas Jr., Hydrogen evolution at the negative electrode of the all-vanadium redox flow batteries, J. Power Sources 248 (2014) 560–564, https://doi.org/10.1016/j.jpowsour.2013.09.125.

[14] R. Schweiss, A. Pritzl, C. Meiser, Parasitic hydrogen evolution at different carbon fiber electrodes in vanadium redox flow batteries, J. Electrochem. Soc. 163 (9) (2016) A2089–A2094, https://doi.org/10.1149/2.1281609jes.

[15] A. Fetyan, G.A. El-Nagar, I. Lauermann, M. Schnucklake, J. Schneider, C. Roth, Detrimental role of hydrogen evolution and its temperature-dependent impact on the performance of vanadium redox flow batteries, J. Energy Chem. 32 (2019) 57–62, https://doi.org/10.1016/j.jechem.2018.06.010.

[16] A. Battistel, M. Fan, J. Stojadinovic, F. La Mantia, Analysis and mitigation of the artefacts in electrochemical impedance spectroscopy due to three-electrode geometry, Electrochim. Acta 135 (2014) 133–138, https://doi.org/10.1016/j.electacta.2014.05.011.

[17] C.-N. Sun, F.M. Delnick, D.S. Aaron, A.B. Papandrew, M.M. Mench, T.A. Zawodzinski, Probing electrode losses in all-vanadium redox flow batteries with impedance spectroscopy, ECS Electrochem. Lett. 2 (5) (2013) A43–A45, https://doi.org/10.1149/2.001305eel.

[18] J.R. Macdonald, M.K. Brachman, Linear-system integral transform relations, Rev. Mod. Phys. 28 (4) (1956) 393–422, https://doi.org/10.1103/RevModPhys.28.393.

[19] P. Agarwal, M.E. Orazem, L.H. Garci-Rubio, Measurement models for electrochemical impedance spectroscopy. I. demonstration of applicability, J. Electrochem. Soc. 139 (7) (1992) 1917–1927, https://doi.org/10.1149/1.2069522.

[20] M. Schoenleber, E. Ivers-Tiffée, Approximability of impedance spectra by RC elements and implications for impedance analysis, Electrochem. Commun. 58 (2015) 15–19, https://doi.org/10.1016/j.elecom.2015.05.018.

[21] A.D. Franklin, H.J. de Bruin, The fourier analysis of impedance spectra for electroded solid electrolytes, Phys. Status Solidi (a) 75 (2) (1983) 647–656, https://doi.org/10.1002/pssa.2210750240.

[22] H. Schichlein, A.C. Müller, M. Voigts, A. Krügel, E. Ivers-Tiffée, Deconvolution of electrochemical impedance spectra for the identification of electrode reaction mechanisms in solid oxide fuel cells, J. Appl. Electrochem. 32 (8) (2002) 875–882, https://doi.org/10.1023/A:1020599525160.

[23] J. Macutkevic, J. Banys, A.A. Matulis, Determination of the distribution of the relaxation times from dielectric spectra, Nonlinear Anal. Model Control 9 (2004) 75–88. URL, https://pdfs.semanticscholar.org/75c0/10188a55fe27f1706b1727e299ddbf1ffe15.pdf.

[24] M. Saccoccio, T.H. Wan, C. Chen, F. Ciucci, Optimal regularization in distribution of relaxation times applied to electrochemical impedance spectroscopy: ridge and lasso regression methods - a theoretical and experimental study, Electrochim. Acta 147 (2014) 470–482, https://doi.org/10.1016/j.electacta.2014.09.058.

[25] T.H. Wan, M. Saccoccio, C. Chen, F. Ciucci, Influence of the discretization methods on the distribution of relaxation times deconvolution: implementing radial basis functions with DRTtools, Electrochim. Acta 184 (2015) 483–499, https://doi.org/10.1016/j.electacta.2015.09.097.

[26] Y. Zhang, Y. Chen, M. Yan, F. Chen, Reconstruction of relaxation time distribution from linear electrochemical impedance spectroscopy, J. Power Sources 283 (2015) 464–477, https://doi.org/10.1016/j.jpowsour.2015.02.107.

[27] Y. Zhang, Y. Chen, M. Li, M. Yan, M. Ni, C. Xia, A high-precision approach to reconstruct distribution of relaxation times from electrochemical impedance spectroscopy, J. Power Sources 308 (2016) 1–6, https://doi.org/10.1016/j.jpowsour.2016.01.067.

[28] T. Hörlin, Maximum entropy in impedance spectroscopy of non-inductive systems, Solid State Ion. 67 (1) (1993) 85–96, https://doi.org/10.1016/0167-2738(93)90313-R.

[29] T. Hörlin, Deconvolution and maximum entropy in impedance spectroscopy of noninductive systems, Solid State Ion. 107 (3) (1998) 241–253, https://doi.org/10.1016/S0167-2738(98)00008-3.

[30] A.B. Tesler, D.R. Lewin, S. Baltianski, Y. Tsur, Analyzing results of impedance spectroscopy using novel evolutionary programming techniques, J. Electroceram. 24 (4) (2010) 245–260, https://doi.org/10.1007/s10832-009-9565-z.

[31] S. Hershkovitz, S. Baltianski, Y. Tsur, Harnessing evolutionary programming for impedance spectroscopy analysis: a case study of mixed ionic-electronic conductors, Solid State Ion. 188 (1) (2011) 104–109, https://doi.org/10.1016/j.ssi.2010.10.004.

[32] B.A. Boukamp, Fourier transform distribution function of relaxation times; application and limitations, Electrochim. Acta 154 (2015) 35–46, https://doi.org/10.1016/j.electacta.2014.12.059.

[33] B.A. Boukamp, A. Rolle, Analysis and application of distribution of relaxation times in solid state ionics, Solid State Ion. 302 (2017) 12–18, https://doi.org/10.1016/j.ssi.2016.10.009.

[34] B.A. Boukamp, Derivation of a distribution function of relaxation times for the (fractal) finite length warburg, Electrochim. Acta 252 (2017) 154–163, https://doi.org/10.1016/j.electacta.2017.08.154.

[35] B.A. Boukamp, A. Rolle, Use of a distribution function of relaxation times (DFRT) in impedance analysis of SOFC electrodes, Solid State Ion. 314 (2018) 103–111, https://doi.org/10.1016/j.ssi.2017.11.021.

[36] J.R. Macdonald, J. Schoonman, A.P. Lehnen, Three dimensional perspective plotting and fitting of immittance data, Solid State Ion. 5 (1981) 137–140, https://doi.org/10.1016/0167-2738(81)90211-3.

[37] J.R. Macdonald, Impedance spectroscopy: old problems and new developments, Electrochim. Acta 35 (10) (1990) 1483–1492, https://doi.org/10.1016/0013-4686(90)80002-6.

[38] J.R. Macdonald, Exact and approximate nonlinear least–squares inversion of dielectric relaxation spectra, J. Chem. Phys. 102 (15) (1998) 6241, https://doi.org/10.1063/1.469070.

[39] M. Hahn, S. Schindler, L.-C. Triebs, M.A. Danzer, Optimized process parameters for a reproducible distribution of relaxation times analysis of electrochemical systems, Batteries 5 (2) (2019) 43, https://doi.org/10.3390/batteries5020043.

[40] T. Tichter, J. Schneider, Polarographica. https://github.com/Polarographica/Polarographica_program.

[41] T. Tichter, J. Schneider, D. Andrae, M. Gebhard, C. Roth, Universal algorithm for simulating and evaluating cyclic voltammetry at macroporous electrodes by considering random arrays of microelectrodes, ChemPhysChem (2019), https://doi.org/10.1002/cphc.201901113. In press.

[42] rhd instruments, Relaxis drt. https://www.rhd-instruments.de/en/products/software/relaxis/relaxis-drt.

[43] A. Leonide, V. Sonn, A. Weber, E. Ivers-Tiffée, Evaluation and modeling of the cell resistance in anode-supported solid oxide fuel cells, J. Electrochem. Soc. 155 (1) (2007) B36–B41, https://doi.org/10.1149/1.2801372.

[44] V. Sonn, A. Leonide, E. Ivers-Tiffée, Combined deconvolution and CNLS fitting approach applied on the impedance response of technical Ni/8YSZ cermet electrodes, J. Electrochem. Soc. 155 (7) (2008) B675–B679, https://doi.org/10.1149/1.2908860.

[45] H. Sumi, T. Yamaguchi, K. Hamamoto, T. Suzuki, Y. Fujishiro, T. Matsui, K. Eguchi, AC impedance characteristics for anode-supported microtubular solid oxide fuel cells, Electrochim. Acta 67 (2012) 159–165, https://doi.org/10.1016/j.electacta.2012.02.021.

[46] T. Ramos, M. Søgaard, M.B. Mogensen, Electrochemical characterization of Ni/ScYSZ electrodes as SOFC anodes, J. Electrochem. Soc. 161 (4) (2014) F434–F444, https://doi.org/10.1149/2.045404jes.

[47] C. Endler, A. Leonide, A. Weber, F. Tietz, E. Ivers-Tiffée, Time-dependent electrode performance changes in intermediate temperature solid oxide fuel cells, J. Electrochem. Soc. 157 (2) (2010) B292, https://doi.org/10.1149/1.3270047.

[48] J.P. Schmidt, T. Chrobak, M. Ender, J. Illig, D. Klotz, E. Ivers-Tiffée, Studies on LiFePO₄ as cathode material using impedance spectroscopy, J. Power Sources 196 (12) (2011) 5342–5348, https://doi.org/10.1016/j.jpowsour.2010.09.121.

[49] J.P. Schmidt, P. Berg, M. Schönleber, A. Weber, E. Ivers-Tiffée, The distribution of relaxation times as basis for generalized time-domain models for Li-ion batteries, J. Power Sources 221 (2013) 70–77, https://doi.org/10.1016/j.jpowsour.2012.07.100.

[50] J. Illig, J.P. Schmidt, M. Weiss, A. Weber, E. Ivers-Tiffée, Understanding the impedance spectrum of 18650 LiFePO₄-cells, J. Power Sources 239 (2013) 670–679, https://doi.org/10.1016/j.jpowsour.2012.12.020.

[51] M. Schoenleber, E. Ivers-Tiffee, Analyzing capacitive characteristics of lithium-ion batteries using a distribution function of the differential capacity, ECS Trans. 69 (2015) 45–50, https://doi.org/10.1149/06901.0045ecst, 1, Batteries.

[52] A. Weiß, S. Schindler, S. Galbiati, M.A. Danzer, R. Zeis, Distribution of relaxation times analysis of high-temperature PEM fuel cell impedance spectra, Electrochim. Acta 230 (2017) 391–398, https://doi.org/10.1016/j.electacta.2017.02.011.

[53] S. Simon Araya, F. Zhou, S. Lennart Sahlin, S. Thomas, C. Jeppesen, S. Knudsen Kær, Fault characterization of a proton exchange membrane fuel cell stack, Energies 12 (1) (2019) 152, https://doi.org/10.3390/en12010152.

[54] R.M. Darling, M.L. Perry, Half-cell, steady-state flow-battery experiments, ECS Trans. 53 (7) (2013) 31–38, https://doi.org/10.1149/05307.0031ecst.

[55] R.M. Darling, M.L. Perry, The influence of electrode and channel configurations on flow battery performance, J. Electrochem. Soc. 161 (9) (2014) A1381–A1387, https://doi.org/10.1149/2.0941409jes.

[56] C.-N. Sun, F.M. Delnick, D.S. Aaron, A.B. Papandrew, M.M. Mench, T.A. Zawodzinski, Resolving losses at the negative electrode in all-vanadium redox flow batteries using electrochemical impedance spectroscopy, J. Electrochem. Soc. 161 (6) (2014) A981−A988, https://doi.org/10.1149/2.045406jes.

[57] A.M. Pezeshki, R.L. Sacci, F.M. Delnick, D.S. Aaron, M.M. Mench, Elucidating effects of cell architecture, electrode material, and solution composition on overpotentials in redox flow batteries, Electrochim. Acta 229 (2017) 261−270, https://doi.org/10.1016/j.electacta.2017.01.056.

[58] R. Schweiss, C. Meiser, F.W.T. Goh, Steady-state measurements of vanadium redox-flow batteries to study particular influences of carbon felt properties, ChemElectroChem 4 (8) (2017) 1969−1974, https://doi.org/10.1002/celc.201700280.

[59] R. Schweiss, C. Meiser, D. Dan, Effect of operating temperature on individual half-cell reactions in all-vanadium redox flow batteries, Batteries 4 (4) (2018) 55, https://doi.org/10.3390/batteries4040055.

[60] M. Schönleber, D. Klotz, E. Ivers-Tiffée, A method for improving the robustness of linear kramers-kronig validity tests, Electrochim. Acta 131 (2014) 20−27, https://doi.org/10.1016/j.electacta.2014.01.034.

[61] E. Agar, C.R. Dennison, A.R. Kalidindi, K.W. Knehr, E.C. Kumbur, Reaction Kinetics of Vanadium Species on Functionalized Carbon-Felt Electrodes of Vanadium Redox Flow Batteries, American Chemical Society, 2012. ENFL−667.

[62] D. Aaron, C.-N. Sun, M. Bright, A.B. Papandrew, M.M. Mench, T.A. Zawodzinski, In situ kinetics studies in all-vanadium redox flow batteries, ECS Electrochem. Lett. 2 (3) (2013) A29−A31, https://doi.org/10.1149/2.001303eel.

[63] J. Langner, J. Melke, H. Ehrenberg, C. Roth, Determination of overpotentials in all vanadium redox flow batteries, ECS Trans. 58 (37) (2014) 1−7, https://doi.org/10.1149/05837.0001ecst.

[64] A. Bhattarai, A.H. Whitehead, R. Schweiss, G.G. Scherer, M. Skyllas-Kazacos, N. Wai, T.D. Nguyen, P.C. Ghimire, M.O. Oo, H.H. Hng, Anomalous behavior of anion exchange membrane during operation of a vanadium redox flow battery, ACS Appl. Energy Mater. 2 (3) (2019) 1712−1719, https://doi.org/10.1021/acsaem.8b01816.

[65] T. Reshetenko, A. Kulikovsky, On the origin of high frequency impedance feature in a PEM fuel cell, J. Electrochem. Soc. 166 (15) (2019) F1253−F1257, https://doi.org/10.1149/2.1201915jes.

[66] A. Lasia, Electrochemical Impedance Spectroscopy and its Applications, Springer New York, New York, NY, 2014, https://doi.org/10.1007/978-1-4614-8933-7.

[67] G. Paasch, K. Micka, P. Gersdorf, Theory of the electrochemical impedance of macrohomogeneous porous electrodes, Electrochim. Acta 38 (18) (1993) 2653−2662, https://doi.org/10.1016/0013-4686(93)85083-B.

Rotating ring-disc measurements for the quantitative electrokinetic investigation of the V^{3+}-reduction at modified carbon electrodes

T. Tichter [1, *], **J. Schneider** [1], D. Nguyen Viet [1], A. D. Duque [1], C. Roth [2]

[1]   Institute of Chemistry and Biochemistry, Freie Universität Berlin, Arnimallee 22, 14195, Berlin, Germany
[2]   Electrochemical Process Engineering, Universität Bayreuth, Universitätsstraße 30, 95447, Bayreuth, Germany
[*]   corresponding author: T. Tichter

Author	Individual contributions
T. Tichter	Conceptualization, Methodology, Software, Writing – Original Draft, Writing - Review and Editing, Visualization
J. Schneider	Conceptualization, Software, Writing - Review and Editing
D. Nguyen Viet	Investigation, Validation
A. D. Duque	Conceptualization, Writing - Review and Editing, Software
C. Roth	Supervision, Funding Acquisition, Writing - Review and Editing

Contents lists available at ScienceDirect

Journal of Electroanalytical Chemistry

Rotating ring-disc electrode measurements for the quantitative electrokinetic investigation of the V^{3+}-reduction at modified carbon electrodes

Tim Tichter[a,*], Jonathan Schneider[a], Duc Nguyen Viet[a], Alvaro Diaz Duque[a], Christina Roth[b]

[a]Freie Universität Berlin, Takustr. 3, 14195, Germany
[b]Universität Bayreuth, Universitätsstr. 30, Bayreuth 95447, Germany

ARTICLE INFO

ABSTRACT

Thin film rotating-ring disc electrode (RRDE) technique is exploited to quantify the parasitic hydrogen evolution reaction (HER) competing with the desired V^{3+}-reduction at surface modified carbon nanoparticles for application as electrocatalysts in the negative half-cell of vanadium redox-flow batteries (VRFB). Carbon based electrode materials are derived from standard Vulcan XC-72 carbon, treated by chemical surface etching techniques proposed for carbon felt-electrodes in the literature. Additional electrochemical characterization is performed using stationary cyclic voltammetry (CV) followed by fitting of CV data, Fourier-transform alternating-current cyclic voltammetry (FT-ACCV) and electrochemical impedance spectroscopy (EIS) followed by distribution of relaxation times (DRT) analysis. To our knowledge the present paper is the first study using the RRDE technique for separating HER and V^{3+}-reduction reactions. It is demonstrated that the ratio of HER to V^{3+}-reduction significantly depends on the chemical pretreatment of the carbon electrodes and that the V^{3+}-reduction proceeds at an optimum rate at $E - E_{RHE} = -0.45$ V. Separating the HER from the V^{3+}-reduction also allows us to provide highly accurate values for the diffusion coefficient of the V^{3+}-ion in sulfuric acid solutions.

© 2020 Elsevier B.V. All rights reserved.

1. Introduction

In the past decade numerous carbon based materials have been suggested for their possible application as electrocatalysts in vanadium redox-flow batteries. In this context, current research focuses predominantly on enhancing the intrinsic catalytic activity of the carbon electrodes, by a) chemical surface modifications such as alkaline etching [1-4], acidic etching [5,6], surface hydroxylation [7] and surface halogenation [8], b) electrochemical surface oxidation techniques [9,10] and c) surface impregnation techniques with either activated carbon nanoparticles [11-15] or metals and metal oxides such as bismuth [16], iridium [17], niobium [18], titanium nitride [19], titanium carbide [20], titanium oxide [21-23] and zirconia [24]. Also thermal treatments and carbonization techniques for introducing nitrogen doping [25,26] or plasma treatments for introducing oxygen containing functional groups [27,28] were proposed. The electrochemical performance of such modified carbon materials is usually investigated using cyclic voltammetry (CV). Subsequent data evaluation is performed either qualitatively by comparing peak-to-peak separations, peak height and arbitrarily chosen onset potentials of the CV's redox peaks [6-9,14-16,19-21,26,27, 29-38], or quantitatively by applying the Randles-Ševčík relations [3,39,40]. However, it is worth to mention that the peak-to-peak separation and the peak height in a CV are unambiguously linked to the electrode kinetics only for irreversible reactions at planar electrodes in semi-infinite diffusion space [41-44]. Consequently, for different electrode geometries, diffusion domains and for different reaction types, the Randles-Ševčík relations do not apply either. As the majority of electrodes investigated are carbon felts possessing complex internal diffusion domains, significant misinterpretation of the kinetic performance can occur. At the negative side of the vanadium redox-flow cell, data evaluation gets even more complicated, as the desired V^{3+}-reduction is always accompanied by the parasitic hydrogen evolution. Consequently, as the measured current in a CV will always be the sum of the desired and the parasitic reaction, neither kinetic, nor hydrodynamic parameters of the V^{3+}-reduction can be extracted by applying the Randles-Ševčík relations. This might be one of the reasons, why literature values for the diffusion coefficient of the V^{3+}-ion in sulfuric acid solutions (the common electrolyte in vanadium redox-flow batteries) cannot be found.

---

* Corresponding author.
E-mail address: t.tichter@fu-berlin.de (T. Tichter).

In this paper we exploit the rotating ring-disc electrode (RRDE) technique, which is a standard analysis tool in the fuel cell community to quantify undesired side reactions for separating the desired V^{3+}-reduction from the parasitic hydrogen evolution at carbon based electrode materials. To our knowledge this study is the first to apply the RRDE technique in context of vanadium redox-flow systems. In this manner we are able to demonstrate that the V^{3+}-reduction proceeds at an optimum rate at $E - E_{RHE} = -0.45$ V and that more negative potentials cause a significantly increased hydrogen evolution. Furthermore, we are able to quantitatively investigate the influence of surface modification techniques proposed in the literature on the kinetics of the V^{3+}-reduction reaction and to provide accurate values for the diffusion coefficient of the V^{3+}-ion in sulfuric acid solutions. Additional electrochemical characterization is performed via a) standard cyclic voltammetry followed by CV-fitting using our in house developed software tool *Polarographica*, b) via Fourier transform alternating current voltammetry (FT-ACCV) and c) via electrochemical impedance spectroscopy (EIS) followed by distribution of relaxation times (DRT) analysis supporting the RRDE results.

2. Experimental section

2.1. Carbon functionalization

Carbon surface etching was performed starting from Vulcan XC-72. Samples were prepared by adding Vulcan XC-72 (100 mg) to a) hydrogen peroxide (5 mL, 30% suprapura, VWR chemicals), b) a volumetric 2/1 mixture of sulfuric acid (2.5 mL, 96%, Carl Roth) and nitric acid (2.5 mL, 65%, Carl Roth, ROTIPURAN) and c) a KOH solution (2 M, prepared by dissolving KOH 85%, Carl Roth in MilliQ, 18.2 MΩ). Reaction mixtures were stirred at ambient temperature for 20 days. The etching process was stopped by quenching with ultrapure water (100 mL, MilliQ, 18.2 MΩ). Subsequently, carbon nanoparticles were obtained by vacuum filtration (Whatman polycarbonate, 0.1 micron filter), a cleaning by several washing steps with ultrapure water (100 mL, MilliQ, 18.2 MΩ) and drying at 70 °C under air atmosphere. Dried catalyst powders were grinded thoroughly in a mortar. Required amounts of carbon powders were then dispersed ultrasonically in ultrapure water (1 mL, MilliQ, 18.2 MΩ) to give inks with concentrations of $0.5 \mu g_C/L$. As reference, an ink was prepared from pristine Vulcan XC-72.

2.2. Electrode preparation

As electrode a commercial RRDE-tip (glassy carbon disc, platinum ring, Pine Instruments, AFE6R1PT) was used. In order to suppress any hydrogen detection on the Pt-ring, the ring was inactivated electrochemically by depositing copper from a copper(II)-sulfate solution (0.1 M, Carl Roth) in sulfuric acid (2 M, prepared by diluting sulfuric acid, 96%, Carl Roth with ultrapure water Carl Roth, MilliQ, 18.2 MΩ) onto the platinum surface. Subsequently, the glassy carbon disc, the gap between disc and ring as well as the part of the electrode outside of the ring was sealed with duct tape. By dropping Vulcan XC-72 ink on the partially sealed electrode tip, Vulcan XC-72 carbon was coated homogeneously on the copper layer of the ring. After drying of the ink at ambient temperature and removing the duct tape, 20 μL of the respective ink dispersions were applied onto the glassy carbon (GC) disc ($0.196 \, cm^2$ geometrical surface area). A homogenous coating was obtained by evaporating the solvent at ambient temperature.

2.3. Electrochemical measurements

Electrochemical characterization was performed in a three electrode setup consisting of a Pt-mesh counter-, a Ag/AgCl- reference
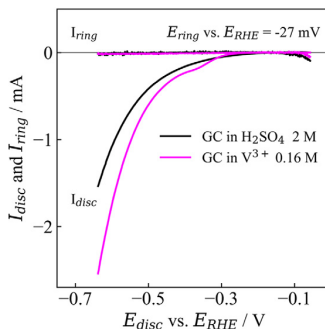

Fig. 1. RRDE measurements performed at a glassy carbon disc in 2 M H_2SO_4-solution (black curves) and in 0.16 M V^{3+}-containing 2 M H_2SO_4-solution (pink curves). In both cases no ring current signal is detected, indicating no V^{3+}-reduction at the glassy carbon disc.

($c_{KCl} = 4.2$ M, sat., $E_{Ref} - E_{SHE} = 198$ mV) and the prepared RRDE as working electrode. Measurements were carried out using a BioLogic potentiostat (VSP-300, Bio-Logic Science Instruments) providing a bipotentiostatic mode.

RRDE measurements were carried out at rotation rates of $\omega = 123, 156, 204$ and 278 rpm between $E_{disc} - E_{Ref} = -0.2$ V and -0.8 V by keeping the ring potential at $E_{ring} - E_{Ref} = -0.19$ V with a potential sweep rate of $\nu = 10$ mV/s. CV measurements were performed in stationary mode between $E_{disc} - E_{Ref} = -0.2$ V and -0.8 V with a potential sweep rate of $\nu = 10$ mV/s. ACCV measurements were performed in the potential window of the classical CV measurements, with the same dc-potential sweep-rate with a modulated excitation frequency of $f = 20$ Hz and an amplitude of $\Delta E = 20$ mV. Electrochemical impedance spectroscopy measurements were performed after conditioning the electrodes at $E_{disc} - E_{Ref} = -0.55$ V for $t = 120$ s in a frequency range from $f_{max} = 5$ kHz to $f_{min} = 0.1$ Hz with an excitation amplitude of $\Delta E = 5$ mV.

3. Results and discussion

3.1. RRDE-measurements

In order to demonstrate the electrochemical inertness of the Cu/C coated Pt-ring of the RRDE for the hydrogen detection, Fig. 1 depicts the disc current I_{disc} as well as the ring current I_{ring} for a potential sweep experiment at a glassy carbon disc in 2 M sulfuric acid as well as in a 2 M sulfuric acid solution containing 0.16 M V^{3+}-ions. It can be seen that the Cu/C coated ring of the electrode does not provide any oxidative current signal in case of the pure 2 M sulfuric acid electrolyte confirming that no hydrogen, which is produced at the uncoated glassy carbon disc, can be oxidized at the ring. It should be noted that also in case of the V^{3+}-containing electrolyte no oxidative ring current is detected, even if the current signal at the glassy carbon electrode gets increased.

This demonstrates that a pure glassy carbon electrode does not catalyze any V^{3+}-reduction, but the presence of V^{3+}-ions in the electrolyte obviously enhances the hydrogen evolution kinetics at the carbon surface.

Fig. 2 depicts the RRDE measurements (A) as well as the corresponding Koutecký-Levich plots (B) of the disc- and ring-current performed for the Vulcan XC-72 as well as for the H_2O_2-modified Vulcan XC-72 coated the glassy carbon disc of the RRDE-tip.

It can be seen that in both cases no well-defined limiting disc-current is reached, even if a plateau is implied around $E_{disc} - E_{RHE} = -0.45\,V$. However, it has to be noted that compared to the uncoated glassy carbon disc a) a ring current can be detected, verifying the reduction of V^{3+}-ions at the coated glassy carbon disc and b) the ring current reaches a maximum at $E_{disc} - E_{RHE} = -0.45\,V$ and decreases, as the disc potential is swept more negative. This can be explained by the assumption that the electrode reaction gets more selective for the parasitic hydrogen evolution reaction at lower potentials and thus a lower amount of vanadium reacts at the disc electrode surface. On a first glance a significant enhancement in the hydrogen evolution rate could also be expected, when considering the absolute value of the disc currents that significantly increases when the disc potential is swept below $E_{disc} - E_{RHE} = -0.5\,V$. However, without using an RRDE the lower selectivity for the V^{3+}-reduction would not be seen. As a consequence it can be concluded that the vanadium reduction kinetics proceed at an optimum at potentials around $E_{disc} - E_{RHE} = -0.45\,V$. Results for the diffusion coefficient calculated from the ring- as well

as from the disc-currents using the Koutecký-Levich equation (Eq. (1)) are shown in Fig. 2B).

$$\frac{1}{I} = \frac{1}{I_{kin}} + \frac{1}{0.201nFAcD^{2/3}\eta^{-1/6}\sqrt{\omega}} \qquad (1)$$

It can be seen that the diffusion coefficient calculated from the disc-current is about twice the diffusion coefficient calculated from the ring current. This can be assigned to the fact, that the disc current consists of the charge generated by the desired V^{3+}-reduction as well as by the parasitic hydrogen evolution reaction. Consequently, calculating the diffusion coefficient of the V^{3+}-ion exclusively from the disc current has to provide wrong results. As the ring current is selectively caused by the re-oxidation of V^{2+}-ions formed at the disc, the diffusion coefficient of the V^{3+}-ion can be estimated from the ring current corrected by the collection efficiency of the RRDE-tip (in the present case 25%, defined by the geometry of the RRDE tip [45]). In this manner the diffusion coefficient of the V^{3+}-ion was calculated to be $D_{V3+} \approx 3.5\ 10^{-6}\ cm^2/s$.

Fig. 3 depicts the disc- and ring currents (A) as well as the corresponding Kouteck-Levich plots (B) for the KOH etched Vulcan XC-72

Fig. 2. A) RRDE measurements performed in 0.16 M V^{3+}-containing 2 M H_2SO_4-solution at a Vulcan XC-72 coated glassy carbon disc (orange curves) and at H_2O_2-etched Vulcan XC-72 coated glassy carbon disc (red curves). B) Koutecký-Levich plots of disc and ring current. The ring current reaches a maximum at $E_{disc} - E_{RHE} = -0.45\,V$, indicating an optimum rate concerning the V^{3+}-reduction. D_{disc} and D_{ring} represent the respective diffusion coefficients calculated from the ring- and disc currents.
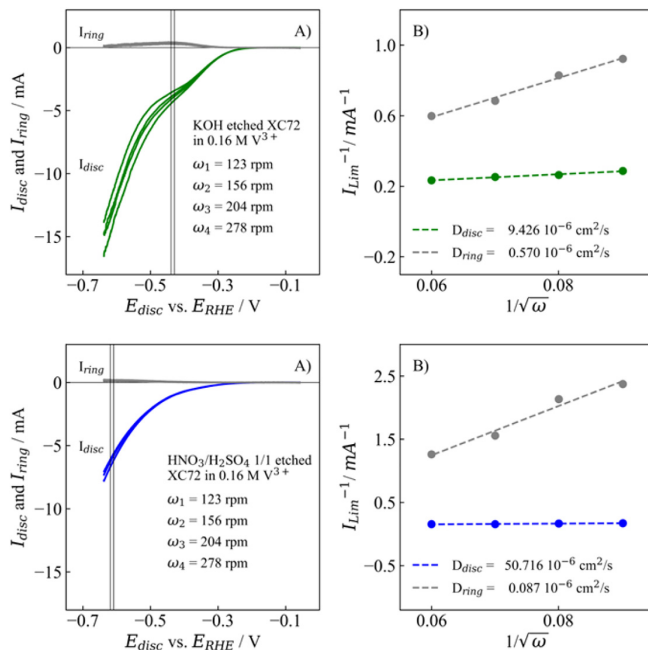
Fig. 3. A) RRDE measurements performed in 0.16 M V^{3+}-containing 2 M H_2SO_4-solution at a KOH-etched Vulcan XC-72 coated glassy carbon disc (green curves) and at a HNO_3/H_2SO_4-etched Vulcan XC-72 coated glassy carbon disc (blue curves). B) Koutecký-Levich plots of disc and ring current. In case of the KOH-etched Vulcan XC-72 a significant increase in the hydrogen evolution rate is detected. The HNO_3/H_2SO_4-etched Vulcan XC-72 shows a significant decrease in the activity concerning V^{3+}-reduction and hydrogen evolution rate. D_{disc} and D_{ring} represent the respective diffusion coefficients calculated from the ring- and disc currents.

as well as for the HNO_3/H_2SO_4-etched Vulcan XC-72, coated on the glassy carbon disc of the RRDE-tip.

From Fig. 3 it can be seen, that in comparison to the pristine- and the H_2O_2-etched Vulcan XC-72 carbon, the KOH-etched sample provides a significant increase in the absolute disc current at more negative potentials. This indicates a strong - and unwanted - enhancement in the parasitic hydrogen evolution. Also the quasi-plateau related to the V^{3+}-reduction becomes less prominent, related to a lower amount of V^{3+} being reacted at the disc surface.

This fact is underlined by the ratio of the V^{3+}-diffusion coefficients calculated from the slope of the Koutecký-Levich lines of disc- and ring currents. There, the diffusion coefficient calculated from the disc current is 1.5 times larger than the diffusion coefficient calculated for the disc currents of Fig. 2. This again confirms an enhanced hydrogen evolution rate at the disc that leads to larger absolute disc current and therefore to a larger apparent diffusion coefficient. In contrast, the diffusion coefficient calculated from the ring current is only 16% of the diffusion coefficient obtained in Fig. 2. This indicates a lower selectivity for the V^{3+}-reduction at the disc in case of the KOH etched Vulcan XC-72 since less V^{2+} is detected as current signal

at the ring and therefore provides a lower apparent diffusion coefficient. However, at this stage it cannot be differentiated whether this decrease is caused by a lowered intrinsic catalytic activity given by the rate constant k^0 or by a loss in active sites of the catalyst material and therefore a lowered active electrode area. These two parameters will be unraveled in Section 3.2.

Surprisingly, Fig. 3 shows that the HNO_3/H_2SO_4-etched Vulcan XC-72 is comparatively inactive with respect to the desired V^{3+}-reduction as indicated by an almost absent ring current. However, in contrast to the KOH-etched Vulcan XC-72 also the rate of the hydrogen evolution reaction is significantly lowered at this sample, as indicated by a strong decrease in the disc current at potentials below $E_{disc} - E_{RHE} = -0.5$ V. As the kinetics of both electrode reactions are significantly slowed down, it is expected that the HNO_3/H_2SO_4-treatment introduces the most significant changes to the electrode surface. Furthermore, as the V^{3+} reduction does not reach any diffusion limitation, calculating the diffusion coefficient for this sample — neither from the disc, nor from the ring current — will provide meaningful values. However, regarding the Kouteck-Levich slope of the disc current it has to be noted that the estimated diffusion coefficient

is in the range of the H^+-ion in aqueous solutions. This indicates, that the main reaction proceeding is hydrogen evolution and, consequently, the V^{3+}-reduction rate is rather negligible. However, it is worth to mention that also for this sample it is not unambiguously clarified whether the lowered reaction rates are introduced by a loss in the electrochemically active surface area or by a decrease in the rate constants of the reactions.

This can be illustrated in the following way. Calculating the diffusion coefficient in Figs. 2 and 3 using Eq. (1) was performed by assuming that the electrochemically active surface area is equal or larger than the geometrical electrode surface area. However, when considering a lower amount of active sites at the electrode surface, such that the active electrode surface is less than the geometric surface area, the lower values for the diffusion coefficients estimated are explained as one divides by an apparently larger value of A. In order to eliminate this uncertainty, the results were complemented by additional cyclic voltammetry keeping the electrode in a stationary mode (no rotation). Considering that the diffusion coefficient scales with the power of $D^{2/3}$ to the current in an R(R)DE measurement and with the power of $D^{1/2}$ in a stationary potential sweep, obtaining the same value for D at an R(R)DE and a stationary electrode (considering the same electrochemical surface area) would provide an unambiguous result.

3.2. Cyclic voltammetry

Since the V^{3+}-reduction is always accompanied by the parasitic hydrogen evolution reaction and the electrode reactions might not be fully irreversible in the electrochemical definition, the classical Randles-Ševčík relations cannot be applied to CV data of the stationary RRDE tip. Consequently, an estimation of the electrode kinetics, the electrode's active surface area or the diffusion coefficient of the electrochemically active species is not possible by simply using the observed peak height. Instead, we performed the data evaluation based on a fitting routine, considering the measured CV as a superposition of the desired vanadium reduction and the parasitic hydrogen evolution. CV fitting was performed using our in-house built software-tool *Polarographica* which has been released as freeware at github [46]. CV fitting is performed by minimizing the standard deviation of simulated to the experimentally acquired data. CV simulations of the vanadium and hydrogen part were performed according to the recurrence relation of Eq. (2).

$$I(i\delta t) = \frac{nFAc\sqrt{D} - 2\sqrt{\frac{\delta t}{\pi}}\sum_{j=0}^{i-1} I(j\delta t)\left(\sqrt{(i-j+1)} - \sqrt{(i-j)}\right)}{\frac{\sqrt{D}}{k^0}\exp\left(\frac{-\alpha nF(E(i\delta t)-E^0)}{RT}\right) + 2\sqrt{\frac{\delta t}{\pi}}\left(1 + \exp\left(\frac{-nF(E(i\delta t)-E^0)}{RT}\right)\right)}$$
(2)

In Eq. (2) the parameters $I, n, F, A, c, D, R, T, E^0$ and k^0 have their usual meaning. The time increment δt was set to 0.0128, corresponding to a resolution of $\delta\xi = 0.01$ in order to provide sufficient accuracy in the calculations [41]. Calculated CV responses minimizing the standard deviation (dots) as well as measured data (solid curves) are depicted in Fig. 4 for all of the four samples investigated.

It can be seen that for all fitted curves the electron transfer coefficient of the V^{3+}-reduction is close to $a = 0.5$, indicating a symmetric activation barrier. However, it should be noted that the rate constant of the V^{3+}-reduction is largest for the H_2O_2-modified Vulcan XC-72 and decreases in the order $k^0(H_2O_2\text{-XC-72}) > k^0$ (pristine XC-72) $> k^0(KOH\text{-XC-72}) \gg k^0(HNO_3/H_2SO_4\text{-XC-72})$. However, regarding the hydrogen evolution reaction, the largest rate constant is obtained for the KOH treated Vulcan XC-72 and decreases in the order of $k^0(KOH\text{-XC-72}) \gg k^0(H_2O_2\text{-XC-72}) > k^0$ (pristine XC-72) $> k^0(HNO_3/H_2SO_4\text{-XC-72})$, confirming the results from the RRDE measurements. Estimated diffusion coefficients for the

V^{3+}-ion are $D(\text{XC-72}) = 3.6 \cdot 10^{-6}$ cm²/s, $D(H_2O_2\text{-XC-72}) = 3.4 \cdot 10^{-6}$ cm²/s, $D(KOH\text{-XC-72}) = 3.5 \cdot 10^{-6}$ cm²/s and $D(HNO_3/H_2SO_4\text{-XC-72}) = 3.5 \cdot 10^{-6}$ cm²/s, being in very good agreement with the results from the RRDE measurements. Estimated active electrode areas are $A(\text{XC-72}) = 0.196$ cm², $A(H_2O_2\text{-XC-72}) = 0.196$ cm², $A(KOH\text{-XC-72}) = 0.08$ cm² and $A(HNO_3/H_2SO_4\text{-XC-72}) = 0.12$ cm². It should be noted that in case of the pure Vulcan XC-72 and the H_2O_2 treated Vulcan-XC-72, the estimated electrochemical surface areas are equal to the geometric electrode area of the glassy carbon surface of the RRDE tip. Consequently, these two samples are the only ones that can provide reasonable values of D in the RRDE measurements, as the required diffusion-convection conditions are fulfilled only for a disc surface active over 100% of its geometrical area. As stated above, since the diffusion coefficients scale in different exponential power to the current at a rotating or a stationary electrode ($I_{RRDE} \propto D^{2/3}$ and $I_{stat} \propto D^{1/2}$), obtaining the same values of D and A at an R(R)DE and a stationary electrode is an unambiguous result. Calculating the mean value and the 3-σ standard deviation of the diffusion coefficients estimated from the stationary CV measurements as well as from the ring currents of the RRDE measurements we obtain $D_{V3+} = (3.51 \pm 0.22) \cdot 10^{-6}$ cm²/s. Consequently, a diffusion coefficient of $D_{V3+} = 3.51 \cdot 10^{-6}$ cm²/s was used for the data evaluation of the KOH-etched and the HNO_3/H_2SO_4-etched Vulcan-XC72-sample.

In case of the KOH-etched sample the lowest active surface area is calculated from the CV fitting. Regarding the value of k^0, only a slight decrease is obtained compared to the pristine Vulcan XC-72 sample. This leads us to the conclusion that the low reaction rate of the KOH etched Vulcan XC-72 is mainly caused by a decrease in the electrode surface area which is active for the desired V^{3+}-reduction. This in turn explains the low value of the diffusion coefficient calculated from the ring current in the RRDE measurements. As the active electrode surface area is less than the geometric surface area, the diffusion-convection conditions of an RRDE are not fulfilled and the ring current signal has to provide misleading results. Regarding the HNO_3/H_2SO_4-treated Vulcan XC-72-sample it has to be noted that the lowest intrinsic catalytic activity (measured by k^0) is obtained. Also the active electrode area is less than the geometric electrode surface for this sample. Consequently, the deviation in the diffusion coefficients calculated from the RRDE measurements is explained as well. Summarizing the results from the RRDE measurements as well as from the CV fitting, we conclude that the highest intrinsic catalytic activity concerning the V^{3+}-reduction can be achieved with the H_2O_2 treated Vulcan-XC-72 sample. However, as this sample also provides an enhanced hydrogen evolution kinetics, the best suited ratio of selectivity and activity is provided by the pristine Vulcan XC-72. Contrarily to the literature, we could demonstrate that a KOH etching and a HNO_3/H_2SO_4 treatment have a negative impact on the electrocatalytic performance of the Vulcan XC-72. In case of KOH etching this effect is mainly caused by a loss in active sites in the electrode surface. In case of the HNO_3/H_2SO_4 treated Vulcan XC-72 the decreased electrode kinetics are mainly due to a loss in the intrinsic catalytic activity governed by the rate constant k^0 of the V^{3+}-reduction reaction. However, it has to be underlined that the electrode materials studied in the literature are carbon felts and not carbon nanoparticles like Vulcan XC-72. Thus, it is possible that the surface etching provides a better wettability of the electrode material, thus an increased electrode surface area and therefore the supposedly increased kinetic performance. It furthermore demonstrates that performing CV measurements in felt electrodes can hardly be used for evaluating the electrokinetic parameters.

3.3. FT-ACCV, EIS and DRT analysis

In order to further investigate the electrokinetic V^{3+}-reduction reaction at the four carbon materials used in this study, Fourier
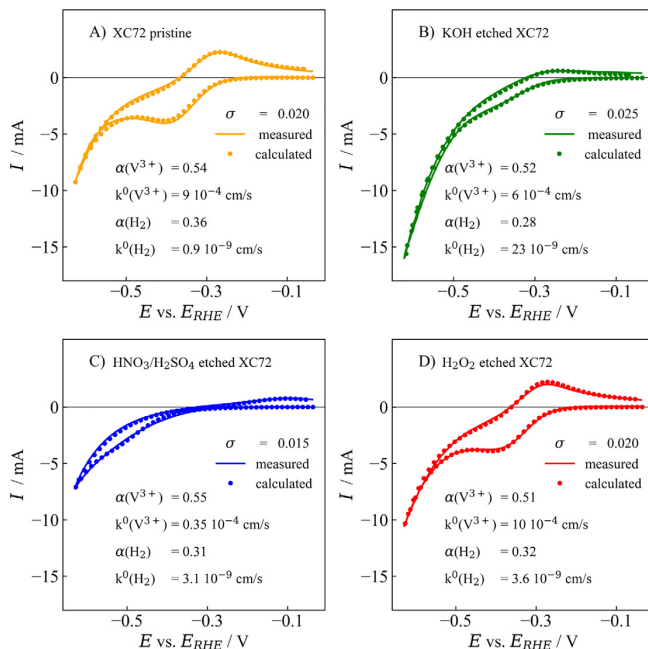
Fig. 4. Measured (solid curves) and fitted (dots) data for the CV measurements at the A) pristine Vulcan XC-72, B) KOH-etched Vulcan XC-72, C) HNO_3/H_2SO_4-etched Vulcan XC-72, and D) H_2O_2-etched Vulcan XC-72. Fitted data was obtained by minimizing the standard deviation of simulated to experimentally acquired data. Simulations were performed by considering a superposition of the desired V^{3+}-reduction and the hydrogen evolution.

transform alternating current cyclic voltammetry (FT-ACCV) and electrochemical impedance spectroscopy (EIS) followed by distribution of relaxation times (DRT) analysis were performed.

FT-ACCV basically uses the triangular potential ramp of a CV experiment with an additional modulated sine-frequency. In this manner, higher harmonics of multiple electrode reactions are excited during the potential sweep. Subsequent Fourier transform of the current signal can be used to separate the different harmonics. Applying inverse Fourier transform of the different harmonics can then be used to calculate the separate current responses of higher harmonic excitations. Since irreversible reactions do not contribute to the higher harmonics in an ACCV experiment [47-49] and as the hydrogen evolution reaction at carbon is an irreversible process (confirmed previously by our RRDE measurements), ACCV appears to be well-suited for differentiating between the V^{3+}-reduction and the parasitic hydrogen evolution. Fig. 5 depicts the current signal obtained from the inverse Fourier transform of A) the base signal (the triangular potential excitation wave), B) the fundamental frequency, C) the first harmonic of the excitation frequency and D) the second harmonic of the excitation frequency.

From the base current signal of Fig. 5A), the classical DC-CV responses are obtained. Again, it can be seen that the H_2O_2-treated

Vulcan XC-72 as well as the pristine Vulcan XC-72 provide similar signals concerning the V^{3+}-reduction and that the H_2O_2-treated Vulcan XC-7 shows an increased hydrogen evolution rate. However, the KOH- as well as the HNO_3/H_2SO_4-etched Vulcan XC-72 sample provide a current signal that is mainly due to hydrogen evolution with no distinct vanadium signal. Regarding the fundamental frequency current response of Fig. 5B), one signal for the V^{3+}-reduction at around $t = 15$ s, one signal for the V^{2+}-re-oxidation around $t = 40$ s as well as one signal for the hydrogen evolution reaction around $t = 30$ s are obtained for the pristine, the H_2O_2-etched and the KOH-etched Vulcan XC-72 samples. However, no vanadium reactions are verified for the HNO_3/H_2SO_4-etched Vulcan XC-72 sample. As the intensities of the signals are proportional to the rates of the respective reactions, the trend of the rate constants obtained from the CV fitting results is confirmed, assigning the highest rate to the H_2O_2-treated Vulcan XC-7 and the lowest reaction rate to the HNO_3/H_2SO_4-etched Vulcan XC-72 sample. The absence of any distinct signal related to vanadium redox-reactions at the HNO_3/H_2SO_4-etched Vulcan XC-72 sample might be assigned to the very low rate of the vanadium reaction, leading to an overlap with the hydrogen evolution current.
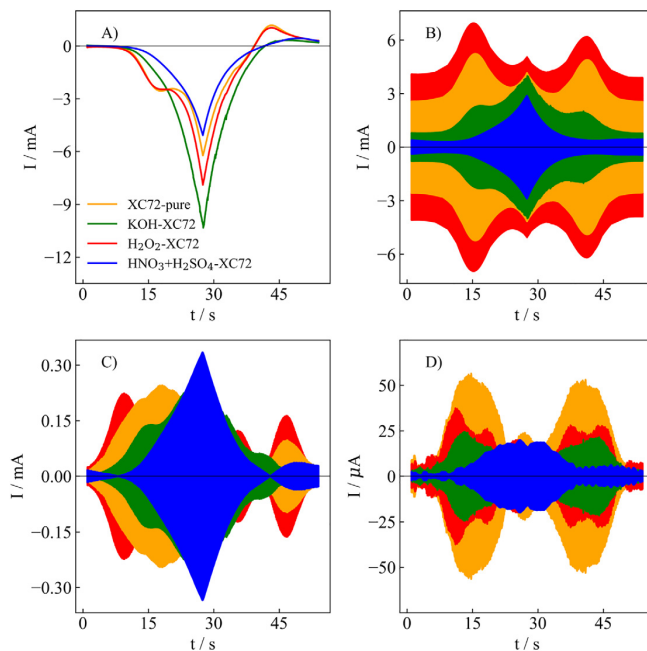
Fig. 5. ACCV signals obtained from inverse Fourier transformation of A) the zero-frequency, B) the fundamental excitation frequency, C) the first harmonic, D) the second harmonic. From panels A)–C) the trend concerning the reaction rates estimated from the CV fitting, i.e. the largest hydrogen evolution rate for the KOH-etched Vulcan XC-72 and the largest reaction rate concerning the V^{3+}-reduction for the H_2O_2-etched Vulcan XC-72 accompanied by an increased hydrogen evolution rate are confirmed. The current signal of the HNO_3/H_2SO_4 treated Vulcan XC-72 in panel D) is assigned to the low V^{3+}-reduction rate, as irreversible reactions, such as the hydrogen evolution at carbon surfaces, do not appear in the second harmonic.

Regarding the first harmonic current signals in Fig. 5C) a qualitative information about the electron transfer coefficient of the reactions can be obtained. By regarding the symmetry of the current signals of the pristine, the H_2O_2-etched and the KOH-etched Vulcan XC-72 samples it can be seen that for the vanadium reaction the signal around $t = 15\,s$ is slightly more intense than the signal around $t = 45\,s$, implying an electron transfer coefficient of α being slightly greater than 0.5. However, in case of the HNO_3/H_2SO_4-etched Vulcan XC-72 sample still no vanadium reactions can be seen. As irreversible reactions like the hydrogen evolution reaction do not contribute to the second harmonic (as well as any other higher harmonics) any signal in Fig. 5D) has to be caused by the desired vanadium reactions. It can be seen that in case of the pristine, the H_2O_2-etched and the KOH-etched Vulcan XC-72 all current signals are equally located around $t = 15\,s$ and $t = 45\,s$. This indicates rather similar rate constants of the processes as it was already suggested from the CV fitting. It is worth to mention that also the HNO_3/H_2SO_4-etched Vulcan XC-72 sample provides a current signal in the second harmonic. This signal has to be related to the V^{3+}-reduction and occurs around $t = 30\,s$ and therefore suggests a significant decrease in the rate constant, when compared to the other three samples. As the intensity

of this signal is comparatively low and its position is equal with the hydrogen evolution signal, the supposed absence of any vanadium reaction in the lower harmonics is explained, as its contribution vanishes in the hydrogen evolution current.

To further support the results obtained via RRDE-, CV- and FT-ACCV measurements, electrochemical impedance spectroscopy (EIS) followed by distribution of relaxation times (DRT) analysis was performed. Fig. 6 depicts A) the obtained Nyquist plots as well as B) the calculated distribution of relaxation times function.

From Fig. 6A) the trend concerning the rate constants of the V^{3+}-reduction obtained from the CV fitting gets confirmed, as the H_2O_2-etched Vulcan XC-72 provides the lowest and the HNO_3/H_2SO_4-etched Vulcan XC-72 the largest charge transfer resistance, indicated by the width of the semi-arc at the real axis. However, as the Nyquist representation provides no information about time constants of the proceeding reactions, data was converted into the DRT representation by using an in-house built modified python translation [46] of the software package DRT-tools [50]. Calculating the DRT function of a certain system is mainly based on approximating the circuit as an infinite series connection of RC-elements (time constants), contributing with different statistical weights to the entire impedance.
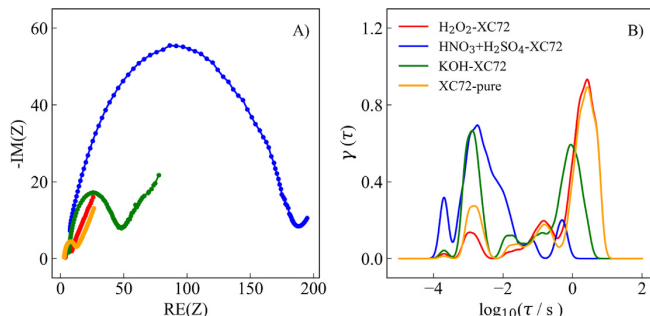
Fig. 6. A) Nyquist- and B) DRT-representation of the electrochemical impedance spectroscopy measurements for the four samples investigated. From panel A) the lowest charge transfer resistance can be assigned to the H_2O_2-treated Vulcan XC-72 and the largest charge transfer resistance to the HNO_3/H_2SO_4-etched Vulcan XC-72 sample, confirming the trend for the reaction rates from the CV fitting process. In panel B), the peak around $log_{10}(\tau) = -3.9$ may be assigned to the contribution of the hydrogen evolution reaction.

Consequently, with $\tau = RC$ and by assuming $C = const.$ and $0 \leq R \leq \infty$, the impedance of the system can be written as

$$Z(\omega) = Z(\infty) + [Z(0) - Z(\infty)] \int_0^\infty \frac{\gamma(\tau)}{1 + j\omega\tau} d\tau \qquad (3)$$

Solving Eq. (3) in terms of $\gamma(\tau)$, a Fredholm integral equation of the first kind, is an ill-posed problem requiring for Tikhonov regularization [51]. For obtaining a smooth and more realistic DRT-function the calculations can be performed by involving a set of radial basis functions (RBF). For theoretical details the reader is referred to ref. [50]. Assuming a gaussian shape of the RBF with an FWHM of $\epsilon = 2.5$ and a Tikhonov regularization parameter of $T = 0.001$, complex non-negative least square fitting was performed to construct the DRT functions shown in Fig. 6. A combined fit of real-and imaginary part of the overall impedance was used. In the DRT representation of Fig. 6B), two main features have to be distinguished. First, the charge-transfer part occurring at low time constants around $log_{10}(\tau) = -4$ to $log_{10}(\tau) = -2.2$ (i.e. a fast process) and second, the diffusive part related to the Warburg element of the impedance occurring at lower time constants around $log_{10}(\tau) = -1.3$ to $log_{10}(\tau) = 1$ (a comparably slower process). The signals between $log_{10}(\tau) = -2.2$ and $log_{10}(\tau) = -1.3$ are numerical artefacts also related to the diffusion part. They occur, since the DRT describes the system investigated as a series connection of RC-elements, that can be illustrated as multiple semi-arcs in the Nyquist representation. As the planar semi-infinite Warburg diffusion, present in this case, leads to a linear slope in the Nyquist plot, the best fit obtained for the DRT provides multiple signals in order to approximate this slope as closely as possible [52]. However, it has to be noted that in case of the pristine as well as for the H_2O_2-treated Vulcan XC-72 sample almost the same diffusion contribution is obtained in the DRT-representation. This can be attributed to the fact that the main reaction proceeding is the V^{3+}-reduction. In case of the KOH-treated and the HNO_3/H_2SO_4-etched Vulcan XC-72 sample much lower signal intensities for the diffusion part were found, that are also shifted towards lower time constants, indicating a faster mass transport. This can be attributed to the fact that a) both reactions are more selective for the hydrogen evolution reaction and the diffusion coefficient of the H^+-ion is much larger than the diffusion coefficient of the V^{3+}-ion and b) the contribution of the

mass transfer part to the overall impedance is comparatively low. Regarding the charge-transfer signal between $log_{10}(\tau) = -4$ to $log_{10}(\tau) = -2.2$ it can be seen that the H_2O_2-treated Vulcan XC-72 sample provides the lowest and the HNO_3/H_2SO_4-etched Vulcan XC-72 sample the highest signal intensity, confirming the results already seen in the Nyquist representation - the H_2O_2-treated Vulcan XC-72 sample possesses the lowest charge transfer resistance. However, it has to be mentioned that the overall charge transfer signal is split up into two subsignals for all samples. One minor signal centered around $log_{10}(\tau) = -3.7$ and a main signal at $log_{10}(\tau) = -2.9$. As the main signal around $log_{10}(\tau) = -2.9$ scales in the inverse trend obtained for the rate constants of the desired V^{3+}-reduction reaction, it can be assigned to the same. However, even if the intensity of the minor signal at $log_{10}(\tau) = -3.7$ follows the same trend as the selectivity of the hydrogen evolution does, it remains questionable whether it can be assigned to this reaction. This is due to the fact that the parasitic hydrogen evolution proceeds at significantly lower rate constants than the vanadium reduction. Consequently, a contribution of the hydrogen evolution reaction would be expected at lower time constants and not at higher ones, as experimentally obtained.

4. Summary and conclusions

In the present paper the thin-film rotating ring-disc electrode technique (RRDE) is first ever used for separating the V^{3+}-reduction reaction from the parasitic hydrogen evolution reaction (HER) at surface modified, carbon based electrode materials for possible application in vanadium redox-flow batteries. Additional electrochemical characterization is performed via stationary cyclic voltammetry (CV) followed by fitting of CV data, Fourier transform alternating current cyclic voltammetry (FT-ACCV) and electrochemical impedance spectroscopy (EIS) followed by distribution of relaxation times (DRT) analysis. Carbon materials investigated are prepared from standard Vulcan XC-72 by surface modification techniques proposed in the literature, namely H_2O_2 etching, HNO_3/H_2SO_4-etching and KOH-etching. Regarding the results from the RRDE measurements we demonstrate that the V^{3+}-reduction proceeds at an optimum potential at around $E - E_{RHE} = -0.45$ V and that at more negative potentials the undesired hydrogen evolution dominates the overall electrode reaction. Combining the results from the RRDE measurements and the stationary CV measurements, we are able

to determine the diffusion coefficient of the V^{3+}-ion in sulfuric acid solution to be $D_{V^{3+}} = 3.51 \pm 0.22\,cm^2/s$. From fitting of CV data we conclude that only the H_2O_2-treatment leads to a slight improvement in the activity of the carbon material concerning the V^{3+}-reduction, but also to a significant increase in the undesired hydrogen evolution rate. In contrast, whereas the HNO_3/H_2SO_4-etching leads to a significant decrease in the catalytic activity of both reactions, the KOH-etching significantly increases the undesired hydrogen evolution and decreases the desired V^{3+}-reduction rate. The results from CV fitting are supported qualitatively by analyzing the data obtained from the ACCV and EIS/DRT measurements, showing the best selectivity concerning the V^{3+}-reduction in case of the pristine- and the lowest catalytic performance for the HNO_3/H_2SO_4-etched Vulcan XC-72. It is proposed that converting EIS-data into the DRT representation might be used to differentiate between the desired V^{3+}-reduction reaction and the parasitic hydrogen evolution reaction. Finally we demonstrate that among all samples investigated in this paper, the best combination of activity and selectivity concerning the V^{3+}-reduction is provided by the pristine Vulcan XC-72. This surprising result can be explained when taking into account that most of the surface modifications proposed in the literature are performed for felt electrodes. Since these electrodes possess highly complex diffusion domains, no quantitative differentiation in desired and parasitic reactions can be made. Consequently, a misinterpretation of kinetic data is likely, especially when simply regarding currents and charge transfer resistances. Alternatively we herein propose to investigate novel carbon based materials via the RRDE technique to characterize the kinetics of desired and parasitic reactions simultaneously.

CRediT authorship contribution statement

Tim Tichter: Conceptualization, Methodology, Software, Writing - original draft, Writing - review & editing, Visualization. **Jonathan Schneider:** Conceptualization, Software, Writing - review & editing. **Duc Nguyen Viet:** Investigation, Validation. **Alvaro Diaz Duque:** Conceptualization, Writing - review & editing, Software. **Christina Roth:** Supervision, Funding acquisition, Writing - review & editing.

Declaration of competing interest

The authors declare that they have no known competing financial interests or personal relationships that could have appeared to influence the work reported in this paper.

Acknowledgements

References

[1] L. Dai, Y. Jiang, W. Meng, H. Zhou, L. Wang, Z. He, Applied surface science improving the electrocatalytic performance of carbon nanotubes for VO^{2+}/VO_2^+ redox reaction by KOH activation, Appl. Surf. Sci. 401 (2017) 106–113. https://doi.org/10.1016/j.apsusc.2017.01.002.

[2] Z. Zhang, J. Xi, H. Zhou, X. Qiu, Electrochimica acta KOH etched graphite felt with improved wettability and activity for vanadium flow batteries, Electrochim. Acta 218 (2016) 15–23. https://doi.org/10.1016/j.electacta.2016.09.099.

[3] C. Flox, M. Skoumal, T. Andreu, J. Ramo, J. Rubio-garc, Thermo chemical treatments based on NH_3/O_2 for improved graphite-based fiber electrodes in vanadium redox flow batteries, Carbon 60 (2013) 280–288. https://doi.org/10.1016/j.carbon.2013.04.038.

[4] T. Wu, K. Huang, S. Liu, S. Zhuang, Hydrothermal ammoniated treatment of PAN-graphite felt for vanadium redox flow battery, J. Solid State Electrochem. 16 (2012) 579–585. https://doi.org/10.1007/s10008-011-1383-y.

[5] Y. Jiang, Z. He, Y. Li, J. Zhu, H. Zhou, W. Meng, L. Wang, L. Dai, Carbon layer-exfoliated, wettability-enhanced, SO_3H-functionalized carbon paper: a superior positive electrode for vanadium redox flow battery, Carbon 127 (2017) 293–304. https://doi.org/10.1016/j.carbon.2017.11.006.

[6] L. Yue, W. Li, F. Sun, Highly hydroxylated carbon fibres as electrode materials of all-vanadium redox flow battery, Carbon 48 (2010) 3079–3090. https://doi.org/10.1016/j.carbon.2010.04.044.

[7] C. Gao, N. Wang, S. Peng, S. Liu, Y. Lei, X. Liang, S. Zeng, H. Zi, Influence of Fenton's reagent treatment on electrochemical properties of graphite felt for all vanadium redox flow battery, Electrochim. Acta 88 (2013) 193–202. https://doi.org/10.1016/j.electacta.2012.10.021.

[8] M. Park, I.-Y. Jeon, J. Ryu, H. Jang, J.-B. Back, J. Cho, Edge-halogenated graphene nanoplatelets with F, Cl, or Br as electrocatalysts for all-vanadium redox flow batteries, Nano Energy 26 (2016) 233–240. https://doi.org/10.1016/j.nanoen.2016.05.027.

[9] Z. He, Y. Jiang, H. Zhou, G. Cheng, W. Meng, L. Wang, Graphite felt electrode modified square wave potential pulse for vanadium redox flow battery, Int. J. Energy Res. 141 (2016) 439–447. https://doi.org/10.1002/er.

[10] A. Bourke, M.A. Miller, R.P. Lynch, X. Gao, J. Landon, J.S. Wainright, Electrode kinetics of vanadium flow batteries: contrasting responses of V(I)I-V(III) and V(IV)-V(V) to electrochemical pretreatment of carbon, J. Electrochem. Soc. 163 (2016) 5097–5105. https://doi.org/10.1149/2.0131601jes.

[11] D.-S. Yang, J. Hee, J. Woo, J. Yong, D.-g. Kim, D. Hack, B. Gak, T.-h. Kim, Y. Taik, Multimodal porous and nitrogen-functionalized electrode based on graphite felt modified with carbonized porous polymer skin layer for all-vanadium redox flow battery, Mater. Today Energy 11 (2019) 159–165. https://doi.org/10.1016/j.mtener.2018.11.003.

[12] K.M. Tenny, V.S. Lakhanpal, R.P.D. Jr, V. Yarlagadda, T.V. Nguyen, Impact of multi-walled carbon nanotube fabrication on carbon cloth electrodes for hydrogen-vanadium reversible fuel cells, J. Am. Chem. Soc. 164 (2017) 2534–2538. https://doi.org/10.1149/2.1151712jes.

[13] L. Wei, T.S. Zhao, G. Zhao, L. An, L. Zeng, A high-performance carbon nanoparticle-decorated graphite felt electrode for vanadium redox flow batteries, Appl. Energy 176 (2016) 74–79. https://doi.org/10.1016/j.apenergy.2016.05.048.

[14] G. Zoraida, C. Flox, C. Blanco, M. Granda, J.R. Morante, M. Rosa, S. Ricardo, Outstanding electrochemical performance of a graphene-modified graphite felt for vanadium redox flow battery application, J. Power Sources 338 (2016) 1–8. https://doi.org/10.1016/j.jpowsour.2016.10.069.

[15] S. Park, H. Kim, Fabrication of nitrogen-doped graphite felts as positive electrodes using polypyrrole as a coating agent in vanadium redox flow batteries, J. Mater. Chem. A 00 (2015) 1–8. https://doi.org/10.1039/C5TA02674A.

[16] D.J. Suarez, Z. Gonzalez, C. Blanco, M. Granda, R. Menendez, Graphite felt modified with bismuth nanoparticles as negative electrode in a vanadium redox flow battery, ChemSusChem 7 (2014) 914–918. https://doi.org/10.1002/cssc.201301045.

[17] H.-M. Tsai, S.-J. Yang, C.-M. Ma, X. Xie, Preparation and electrochemical activities of iridium-decorated graphene as the electrode for all-vanadium redox flow batteries, Electrochim. Acta 77 (2012) 232–236. https://doi.org/10.1016/j.electacta.2012.05.099.

[18] B. Li, M. Gu, Z. Nie, X. Wei, C. Wang, V. Sprenkle, W. Wang, Nanorod niobium oxide as powerful catalysts for an all vanadium redox flow battery, Nano Lett. 14 (2014) 158–165. https://doi.org/10.1021/nl403674a.

[19] C. Yang, H. Wang, S. Lu, C. Wu, Y. Liu, Q. Tan, D. Liang, Y. Xiang, Titanium nitride as an electrocatalyst for V(II)/V(III) redox couples in all-vanadium redox flow batteries, Electrochim. Acta 182 (2015) 834–840. https://doi.org/10.1016/j.electacta.2015.09.155.

[20] P.C. Ghimire, R. Schweiss, N. Wai, T.M. Lim, A. Bhattarai, T.D. Nguyen, Q. Yan, Titanium carbide-decorated graphite felt as high performance negative electrode in vanadium redox fl ow batteries, J. Mater. Chem. A 6 (2018) 6625–6632. https://doi.org/10.1039/C8TA00464A.

[21] Z. He, M. Li, Y. Li, J. Zhu, Y. Jiang, W. Meng, Electrochimica acta flexible electrospun carbon nanofiber embedded with TiO_2 as excellent negative electrode for vanadium redox flow battery, Electrochim. Acta 281 (2018) 601–610. https://doi.org/10.1016/j.electacta.2018.06.011.

[22] T.-M. Tseng, R.-H. Huang, C.-Y. Huang, C.-C. Liu, Carbon felt coated with titanium dioxide/carbon black composite as negative electrode for vanadium redox flow, J. Electrochem. Soc. 161 (2014) 1132–1138. https://doi.org/10.1149/2.102406jes.

[23] T.-M. Tseng, R.-H. Huang, C.-Y. Huang, K.-L. Hsueh, Improvement of titanium dioxide addition on carbon black composite for negative electrode in vanadium redox flow battery, J. Electrochem. Soc. 160 (2013) 1269–1275. https://doi.org/10.1149/2.082308jes.

[24] H. Zhou, Y. Shen, J. Xi, X. Qiu, L. Chen, ZrO_2 Nanoparticle-modified graphite felt: bifunctional effects on vanadium flow batteries, Appl. Mater. Interfaces 24 (2016) 15369–15378. https://doi.org/10.1021/acsami.6b03761.

[25] H. Kabir, I.O. Gyan, I.F. Cheng, Electrochemical modification of a pyrolytic graphite sheet for improved negative electrode performance in the vanadium redox flow battery, J. Power Sources 342 (2017) 31–37. https://doi.org/10.1016/j.jpowsour.2016.12.045.

[26] Y. Shao, X. Wang, M. Engelhard, C. Wang, S. Dai, J. Liu, Z. Yang, Y. Lin, Nitrogen-doped mesoporous carbon for energy storage in vanadium redox flow batteries, J. Power Sources 195 (2010) 4375–4379. https://doi.org/10.1016/j.jpowsour.2010.01.015.

[27] E.-M. Hammer, B. Berger, L. Komsiyska, Improvement of the performance of graphite felt electrodes for vanadium-redox-flow-batteries by plasma treatment, Int. J. Renew. Energy Dev. 3 (2014) 7–12. https://doi.org/10.14710/ijred.3.1.7-12.

[28] D. Dixon, D. Babu, J. Langner, M. Bruns, L. Pfaffmann, A. Bhaskar, J. Schneider, F. Scheiba, H. Ehrenberg, Effect of oxygen plasma treatment on the electrochemical performance of the rayon and polyacrylonitrile based carbon felt for the vanadium redox flow battery application, J. Power Sources 332 (2016) 240–248. https://doi.org/10.1016/j.jpowsour.2016.09.070.

[29] P. Han, H. Wang, Z. Liu, X. Chen, W. Ma, J. Yao, Y. Zhu, Graphene oxide nanoplatelets as excellent electrochemical active materials for VO^{2+}/VO_2^+ and V^{2+}/V_{3+} redox couples for a vanadium redox flow battery, Carbon 49 (2010) 693–700. https://doi.org/10.1016/j.carbon.2010.10.022.

[30] W. Li, J. Liu, C. Yan, Multi-walled carbon nanotubes used as an electrode reaction catalyst for VO^{2+}/VO_2^+ for a vanadium redox flow battery, Carbon 49 (2011) 3463–3470. https://doi.org/10.1016/j.carbon.2011.04.045.

[31] Z. González, C. Botas, P. Álvarez, S. Roldán, C. Blanco, R. Santamaría, M. Granda, R. Menéndez, Thermally reduced graphite oxide as positive electrode in vanadium redox flow batteries, Carbon (2011) 1–7. https://doi.org/10.1016/j.carbon.2011.09.041.

[32] W. Li, J. Liu, C. Yan, The electrochemical catalytic activity of single-walled carbon nanotubes towards VO^{2+}/VO_2^+ and V^{3+}/V^{2+} redox pairs for all vanadium redox flow battery, Electrochim. Acta 79 (2012) 102–108. https://doi.org/10.1016/j.electacta.2012.06.109.

[33] J. Jin, X. Fu, L. Q., Y. Liu, Z. Wei, K. Niu, J. Zhang, Identifying the active site in nitrogen-doped graphene for the VO^{2+}/VO_2^+ redox reaction, ACS Nano 7 (2013) 4764–4773. https://doi.org/10.1021/nn3046709.

[34] W. Li, J. Liu, C. Yan, Reduced graphene oxide with tunable C/O ratio and its activity towards vanadium redox pairs for an all vanadium redox flow battery, Carbon 55 (2013) 313–320. https://doi.org/10.1016/j.carbon.2012.12.069.

[35] M. Park, I.-Y. Jeon, J. Ryu, J.-B. Baek, J. Cho, Exploration of the effective location of surface oxygen defects in graphene-based electrocatalysts for all-vanadium redox-flow batteries, Adv. Energy Materials 5 (2014) 1–7. https://doi.org/10.1002/aenm.201401550.

[36] T. Liu, X. Li, H. Nie, C. Xu, H. Zhang, Investigation on the effect of catalyst on the electrochemical performance of carbon felt and graphite felt for vanadium flow batteries, J. Power Sources 286 (2015) 73–81. https://doi.org/10.1016/j.jpowsour.2015.03.148.

[37] J.J. Park, J.H. Park, O.O. Park, J.H. Yang, Highly porous graphenated graphite felt electrodes with catalytic defects for high-performance vanadium redox flow batteries produced via NiO/Ni redox reactions, Carbon 110 (2016) 17–26. https://doi.org/10.1016/j.carbon.2016.08.094.

[38] Y. Xiang, W.A. Daoud, Investigation of an advanced catalytic effect of cobalt oxide modification on graphite felt as the positive electrode of the vanadium redox flow battery, J. Power Sources 416 (2019) 175–183. https://doi.org/10.1016/j.jpowsour.2019.01.079.

[39] C. Flox, M. Skoumal, J. Rubio-garcia, T. Andreu, J. Ramón, Strategies for enhancing electrochemical activity of carbon-based electrodes for all-vanadium redox flow batteries, Appl. Energy 109 (2013) 344–351. https://doi.org/10.1016/j.apenergy.2013.02.001.

[40] K.J. Kim, S. Lee, J. Kim, M. Park, H. Kim, Y.-J. Kim, M. Skyllas-Kazacos, Superior electrocatalytic activity of a robust carbon-felt electrode with oxygen-rich phosphate groups for all- vanadium redox flow batteries, ChemSusChem 9 (2016) 1329–1338. https://doi.org/10.1002/cssc.201600106.

[41] H. Matsuda, Y. Ayabe, Zur Theorie der Randles-Ševčík'schen Kathodenstrahl-Polarographie, Zeitschrift fuer Elektrochemie 59 (1954) 494–503. https://doi.org/10.1002/bbpc.19550590605.

[42] R.S. Nicholson, I. Shain, Theory of stationary electrode polarography single scan and cyclic methods applied to reversible, irreversible, and kinetic systems, Anal. Chem 36 (1964) 706–723. https://doi.org/10.1021/ac60210a007.

[43] K. Aoki, K. Tokuda, H. Matsuda, Theory of linear sweep voltammetry with finite diffusion space, J. Electroanal. Chem. Interfacial Electrochem. 146 (1983) 417–424. https://doi.org/10.1016/S0022-0728(83)80601-9.

[44] K. Aoki, K. Tokuda, H. Matsuda, Theory of linear sweep voltammetry with finite diffusion space: part II. Totally irreversible and quasi-reversible cases, J. Electroanal. Chem. Interfacial Electrochem. 160 (1984) 33–45. https://doi.org/10.1016/S0022-0728(84)80113-8.

[45] A.J. Bard, L.R. Faulkner, Electrochemical Methods Fundamentals and Applications, Wiley and Sons. 2001, pp. 349–352.

[46] T. Tichter, J. Schneider, Polarographica program, (2019) http://github.com/Polarographica/Polarographica_program.

[47] S. Guo, J. Zhang, D.M. Elton, A.M. Bond, Fourier transform large-amplitude alternating current cyclic voltammetry of surface-bound azurin, Anal. Chem 76 (2004) 166–177. https://doi.org/10.1021/ac034901c.

[48] J. Zhang, S.-X. Guo, A.M. Bond, Large-amplitude Fourier transformed high-harmonic alternating current cyclic voltammetry: kinetic discrimination of interfering Faradaic processes at glassy carbon and at boron-doped diamond electrodes, Anal. Chem. 76 (2004) 3619–3629. https://doi.org/10.1021/ac049744b.

[49] H. Adamson, A.M. Bond, A. Parkin, Probing biological redox chemistry with large amplitude Fourier transformed AC voltammetry, Chem. Commun. 53 (2017) 9519–9533. https://doi.org/10.1039/c7cc03870d.

[50] T.H. Wan, M. Saccoccioa, C. Chena, F. Ciuccia, Influence of the discretization methods on the distribution of relaxation times deconvolution: implementing radial basis functions with DRTtools, Electrochim. Acta 184 (2015) 483–499. https://doi.org/10.1016/j.electacta.2015.09.097.

[51] A. Lasia, Electrochemical Impedance Spectroscopy and Its Applications, Springer. 2014, pp. 196–198. https://doi.org/10.1007/978-1-4614-8933-7.

[52] B.A. Boukamp, Derivation of a distribution function of relaxation times for the (fractal) finite length Warburg, Electrochim. Acta 252 (2017) 154–163. https://doi.org/10.1016/j.electacta.2017.08.154.

On the stability of bismuth in modified carbon felt electrodes for vanadium redox flow batteries: An in-operando X-ray computed tomography study

M. Gebhard [1, *], T. Tichter [2], **J. Schneider** [2], J. Mayer [2], A. Hilger [3], M. Osenberg [3], M. Rahn [3], I. Manke [3], C. Roth [1]

[1]   Electrochemical Process Engineering, Universität Bayreuth, Universitätsstraße 30, 95447, Bayreuth, Germany
[2]   Institute of Chemistry and Biochemistry, Freie Universität Berlin, Arnimallee 22, 14195, Berlin, Germany
[3]   Institute of Applied Materials, Helmholtz-Zentrum Berlin für Materialien und Energie GmbH, Hahn-Meitner-Platz 1, 14109, Berlin, Germany
[*]   corresponding author: M. Gebhard

Author	Individual contributions
M. Gebhard	Writing - Original Draft, Conceptualization, Methodology, Design and Realization of Cells and Test Bench, Preparation of Electrodes, Investigation (Electrochemistry), Supervision of Radiography Setup and Experiments, Coordination of Experiments
T. Tichter	Writing - Original Draft, Scientific Discussion, Data Interpretation (Electrochemistry)
J. Schneider	Conceptualization, Scientific Discussion and Consultancy (VRFB), Data Evaluation (Electrochemistry)
J. Mayer	Preparation of Electrodes, Investigation, Data Evaluation (Electrochemistry)
A. Hilger	Supervision of Radiography Setup, Data Evaluation (Radiography), Scientific Discussion and Supervision (Radiography)
M. Osenberg	Supervision of Radiography Setup, Data Evaluation (Radiography)
M. Rahn	Supervision of Radiography Setup, Data Evaluation (Radiography)
I. Manke	Funding Acquisition, Project Coordination
C. Roth	Project Coordination, Funding Acquisition, Writing - Review and Editing, Scientific Supervision

Perspective

On the stability of bismuth in modified carbon felt electrodes for vanadium redox flow batteries: An in-operando X-ray computed tomography study

Marcus Gebhard [a, *], Tim Tichter [b], Jonathan Schneider [b], Jacob Mayer [b], André Hilger [c], Markus Osenberg [c], Mirko Rahn [c], Ingo Manke [c], Christina Roth [a]

[a] Electrochemical Process Engineering, Universität Bayreuth, Universitätsstraße 30, 95447, Bayreuth, Germany
[b] Institute of Chemistry and Biochemistry, Freie Universität Berlin, Arnimallee 22, 14195, Berlin, Germany
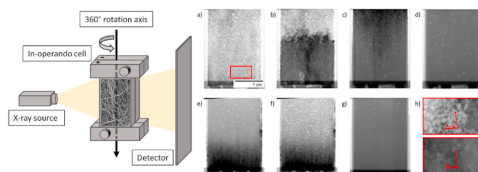[c] Institute of Applied Materials, Helmholtz-Zentrum Berlin für Materialien und Energie GmbH, Hahn-Meitner-Platz 1, 14109, Berlin, Germany

HIGHLIGHTS

- X-ray imaging of bismuth/bismuth oxide stability for vanadium redox flow batteries.
- In-operando cell design allows for X-ray imaging during electrochemical operation.
- Strong influence of metal content/electrolyte flow rate on deposition pattern .

GRAPHICAL ABSTRACT

ARTICLE INFO

ABSTRACT

Decorating carbon felt electrodes with bismuth and bismuth oxide nanoparticles is proposed to be a promising strategy for enhancing the sluggish electron transfer kinetics of the negative half-cell reaction in vanadium redox flow batteries. However, regarding the highly corrosive electrolyte solution, major concerns on the stability of the solid bismuth phase and thus on the local catalyst distribution and catalyst functionality emerge. With this study we present a novel in-operando cell design allowing for X-ray imaging during battery tests in laboratory scale dimensions. In this manner, we verify a dissolution of the bismuth/bismuth oxide particles in open circuit potential condition at SOC = 0 (SOC: state of charge) as well as a re-deposition during the charging process of the battery. No dissolution during the discharging process can be detected. With this knowledge, the effect of the bismuth/bismuth oxide distribution on the electrochemical performance of the battery is investigated. By performing the deposition during the charging process at different electrolyte flow rates, different deposition patterns are obtained. However, independent of the deposition pattern, similar cell performances are achieved that put the enhancement effect by bismuth as heterogeneous catalyst into question.

1. Introduction

In the past decade numerous approaches on improving the performance of the vanadium redox flow battery (VRFB) system were presented. The majority of these studies is dedicated to an enhancement of the sluggish electron transfer kinetics of the vanadium redox reactions at the negative and the positive electrode of the VRFB, respectively. The storyline of most of these publications can be summarized as follows: a) take a commercial carbon material, b) somehow modify its surface and c) measure an improved electrocatalytic performance. In this context, chemical etching [1–5] or plasma treatments [6,7] are proposed to be an appropriate way to achieve an overall improved electrode performance, either due to a better electrode wetting or due to an enrichment of oxygen functional groups that act as active sites for the desired vanadium redox reactions. More recently, impregnation techniques, decorating the felt electrodes with either activated carbon nanoparticles [8–14] or literally any kind of metals and metal compounds (Bi [15–19], Ti [20–22], Nb [23], Mn [24] and Zr [25,26], this list is far from being exhaustive) have become popular. Targeting the V^{2+}/V^{3+}-conversion reaction at the negative VRFB half-cell, in particular an incorporation of the element bismuth [13,16–18] is proposed to be a promising approach. Solid bismuth/bismuth oxide nanoparticles are postulated to increase the heterogeneous electron transfer kinetics of the V^{2+}/V^{3+} redox reaction and to suppress the parasitic hydrogen evolution reaction simultaneously. However, the catalytic effect of solid bismuth/bismuth oxide (as well as of the other metals and metal compounds stated above) can be put to question when taking a look at the corresponding Pourbaix-diagrams [27,28]. Since bismuth turns out to be thermodynamically unstable in presence of the highly corrosive electrolyte solution and the potential window applied in a VRFB, the solid bismuth catalysts should dissolve. Therefore it appears important to investigate possible dissolution and deposition phenomena i.e. by X-ray radiography and tomography. Such X-ray imaging techniques are valuable and well established methods to investigate electrolyte distribution and catalyst dissolution in fuel cells and electrolyzers [29–31]. Consequently, it is somewhat surprising that they are not yet widely applied in recent VRFB studies to validate the hypothesis on the electrocatalytic effect of bismuth. To the best of our knowledge the only studies exploiting X-ray imaging techniques in context of the VRFB system are the following ones focusing on the electrolyte and metal free carbon felt electrode behaviour [32–35].

In this work, we present the further development of a previously published cell design [36] by which we were able to accomplish electrochemical battery testing and in-operando X-ray imaging simultaneously. This particular cell design allows for the monitoring of dissolution and re-/deposition phenomena of the solid bismuth phase with a sufficient resolution in time and space in laboratory scale dimensions with laboratory micro-computed tomography (CT) or synchrotron X-ray radiation. Furthermore, steady states of the electrodes can be investigated by tomography imaging to resolve spatial distribution of elements in the felt electrodes. In this set-up, two different bismuth modified carbon felts serving as the negative VRFB electrodes are investigated and compared to their conventional bismuth free analogue. We demonstrate that the stability of the Bi phase significantly depends on the state of charge (SOC) of the electrolyte showing a non-faradaic dissolution at SOC = 0. Under similar conditions electrochemically re-/deposited bismuth/bismuth oxide turns out to be more stable, however, also gets dissolved over a sufficiently long period of time. By performing the electrochemical deposition during the charging process of the VRFB at different electrolyte flow rates and bismuth concentrations, different deposition patterns are obtained revealing a more homogeneous distribution at higher electrolyte flow rates. Since similar cell performances are obtained independent of the quantity and distribution of deposited bismuth oxide or the amount of bismuth dissolved in the electrolyte, we finally suggest to carefully rethink the recently reported role of bismuth as heterogeneous catalyst.

2. Experimental section

2.1. Electrode materials and electrode preparation

Pristine carbon felt electrodes (GFD 4.6) from SIGRACELL battery electrodes (SGL Carbon SE, Germany) were used as-received and further denoted as GFD-UT (untreated). Bismuth modified electrodes were prepared by an impregnation of the carbon felts with bismuth (III)oxide (99.9%, Bi_2O_3, Sigma Aldrich, U.S.A.) similar to the procedure described in Ref. [37]. The mass of bismuth oxide applied to the electrodes was calculated to achieve a total loading of 2 wt% and 10 wt% of pure bismuth metal (samples were named Bi2-GFD and Bi10-GFD, respectively). The bismuth oxide was dispersed in ethanol (>99.8%, Carl Roth, Germany) and applied to the felt electrode. Subsequently, the felts were dried at 80 °C for 12 h, followed by a heat treatment. Electrodes were placed in a tube furnace (Carbolite Gero GmbH & Co. KG, Germany) under air atmosphere and heated at 5 K min^{-1} up to 300 °C, where the temperature was maintained for 12 h. Reference felts were prepared with the same heat treatment, however, leaving out the impregnation of bismuth and are named as GFD. Heat treated carbon felts were also used in an additional experiment in which bismuth oxide was dissolved in the electrolyte at concentrations corresponding to a relative loading of 2 wt % and 10 wt% of the felt, respectively (samples were named Bi2ext-GFD and Bi10ext-GFD).

2.2. In-operando cell design

X-ray in-operando imaging of the electrodes was carried out using an in-house built flow-cell set-up. The flow-cell was designed to allow for imaging of the whole operating battery cell with X-ray radiation. Thus, the cell was constructed aiming for a reduced impairment by radiation absorbing materials. For this purpose, polyether ether ketone (PEEK) endplates with a high material strength and stability against chemical degradation and radiation corrosion [38] were used to replace the conventional metal endplates. Graphite plates (FU 4369 HT, Schunk, Germany) were used as current collectors. Polycarbonate (PC) spacers were manufactured to form the flow field in a flow through geometry with an active electrode area of 2×3 cm. The PC spacers were used in a thickness of 3 mm (+1 mm gasket, Viton®, DuPont, U.S.A.) providing a compression of the felt electrodes to 87% [36]. The cell set-up was assembled as shown in Fig. 1 with an anion exchange membrane (FAP 450, Fumatech, Germany).

2.3. Operation of the in-situ cell for battery tests and imaging experiments

This subsection is divided into two parts. Part 2.3.1 is dedicated to the in-operando imaging of bismuth dissolution and re-/deposition behaviour at the negative electrode during selected electrochemical procedures. Subsequently, part 2.3.2 focuses on the electrochemical characterization of the effect of bismuth on the performance of the negative electrodes. Since all experiments are dedicated to the negative side of the VRFB only, the same type of positive electrode material (here GFD-UT) was used in all experiments to allow for a straight-forward comparison.

2.3.1. In-operando imaging experiments

Imaging experiments were conducted at the Helmholtz Zentrum Berlin micro-CT facility. As shown in Fig. 1, the tomography set-up consisted of a cone beam generating Hamamatsu X-ray tube (L8121-03, tungsten anode, Hamamatsu Photonics K-K., Hamamatsu, Japan), a Hamamatsu flat panel detector (C7942SK-05, Hamamatsu Photonics K-K., Hamamatsu, Japan) and the in-operando cell in between. For all experiments the acceleration voltage of the source was kept constant at 60 kV with a current of 166 µA and a spot size of 7 µm. The source object distance was 75 mm and the source detector distance was 250 mm. The nominal pixel size of the detector system was 50 µm. For the
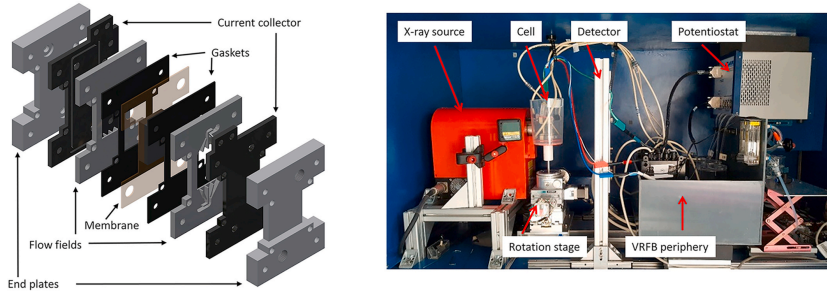
Fig. 1. Cell setup configuration without gaskets and tube connections (left), complete micro-CT set-up as operated similar to Ref. [36] (right).

radiographies the frames were 5 times multi exposed resulting in a temporal resolution of 4.3 s. The effective pixel size of the setup was 15 μm. For the tomographies the frames were 3 times multi exposed and 1200 radiographies over 360° have been taken. The voxel size for the tomographies was 15 μm. The radiographies have been normalized and analysed using Fiji (v1.5.2) [39]. Tomographies have been reconstructed using Octopus (v8.9.4) [40] and visualized using VGStudio MAX (Volume Graphics, Germany).

The VRFB test station consisting of the in-operando flow cell, a Gamry 3000 potentiostat (Gamry Instruments, U.S.A.) and two electrolyte tanks (positive and negative electrolyte) with corresponding pumps (Dosaflex, Germany) was assembled in the micro-CT housing as shown in Fig. 1. The material and periphery were adapted to allow a full 360° rotation of the cell while being connected to the electrolyte tanks, pumps and potentiostat. Prior to operation, the electrolyte tanks were purged with argon (99,999%, Linde, Ireland) and filled with 35 ml commercial vanadium electrolyte (1.6 M Vanadium, in 2 M H_2SO_4 and 0.05 M H_3PO_4, SOC = 0, batch-no: 207445, Gesellschaft für Elektrometallurgie, Germany) each. Radiography was performed during the initial flooding process of the cell as well as during electrochemical operation. Electrochemical test protocols consisted of open circuit potential (OCP), electrochemical impedance spectroscopy measurements and galvanostatic charge or discharge with 100 mA cm^{-2} within the voltage limits of 1.65 V and 0.8 V at a flow rate of 15 ml min^{-1}. Tomography of steady states was performed for the dry cell as well as for the flooded cell prior to and after the galvanostatic charging process. The charging was carried out at 100 mA cm^{-2} at the flow rates given in Table 1. However, during the tomography measurements the electrolyte flow was interrupted and the cell was kept at OCP conditions.

2.3.2. Battery testing

To assess the electrochemical performance of the cell, a battery test system (857 Redox Flow Cell Test System, Scribner Associates) was

Table 1
Sample names of negative electrodes and flow rates applied during the galvanostatic experiments between the individual tomography measurements.

Negative electrode	Sample description	Flow rate ml min^{-1}
GFD	heat treated carbon felt	15
Bi2-GFD	heat treated carbon felt +2 wt% Bi	15
Bi10-GFD	heat treated carbon felt +10 wt% Bi	5,15,25
Bi10ext-GFD	heat treated carbon felt +10 wt% Bi added to the electrolyte	15

used. The in-operando cell was equipped with unmodified and bismuth modified felt electrodes. In analogy to subsection 2.3.1, 35 ml of commercial vanadium electrolyte (1.6 M Vanadium, in 2 M H_2SO_4 and 0.05 M H_3PO_4, batch-no: 207445, Gesellschaft für Elektrometallurgie, Germany) were cycled at a flow-rate of 15 or 25 ml min^{-1} under an inert argon atmosphere. In case of Bi2ext-GFD a respective amount of bismuth oxide was dissolved in the electrolyte prior to operation. For the assessment of the cell performances all presented configurations were tested in a single measurement with galvanostatic cycling within the voltage limits of 1.65 V and 0.8 V at current densities of 25/37.5/50/ 62.5/75/87.5/100 mA cm^{-2} for 5 cycles, respectively. The presented values represent the mean value of the obtained results for each current density.

3. Results and discussion

In analogy to the experimental section the results part is divided into two sub-paragraphs. At first, the most representative results of the X-ray imaging experiments are provided. For the sake of completeness, the respective tomography results are shifted to the supporting information. Subsequently, the electrochemical characterization of unmodified and bismuth modified electrodes is provided.

3.1. X-ray radiography and tomography

3.1.1. GFD reference sample

To assess the influence of bismuth on the VRFB cell performance and to evaluate the distribution of bismuth inside the electrode, the heat treated GFD material was used as reference for battery testing and imaging first. Fig. 2 a depicts the cell with the already flooded positive half cell and the dry negative half cell. The respective flooding process of the negative half cell is shown in Fig. 2 b-d. The electrolyte entering the felt electrode is detected as a dark contrast showing a uniform wetting process. Fig. 2 d depicts the flooded cell prior to the electrochemical testing procedure. Incompletely filled pore volume can be detected as bright spots. However, at this stage it is not possible to distinguish whether the unfilled pore volume is located on the positive or the negative electrode of the cell, which is why tomography was performed (cf. Supplementary information SI 1). It can be seen that a different degree of flooding of the negative electrode (heat treated felt) and the positive electrode (untreated GFD felt) is obtained, being in agreement with our previous findings [36]. Fig. 2 e and f show the cell after galvanostatic charging and discharging at 100 mA cm^{-2}, respectively. No changes in the flooding state of the pore volume can be detected after charging/discharging of the cell.
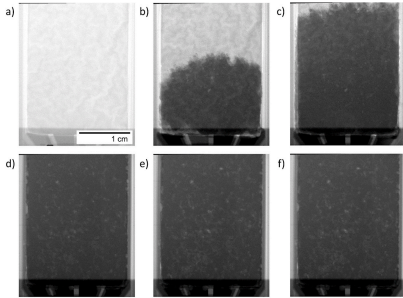
Fig. 2. Reference radiography of GFD at a flow rate of 15 ml min^{-1}; a-c) non-faradaic electrolyte flooding process, d) before galvanostatic charging, e) after galvanostatic charging, f) after galvanostatic discharging at 100 mA cm^{-2}, respectively.

3.1.2. Bismuth containing GFD samples

To identify the role of bismuth in the cell performance it is crucial to detect and localize the bismuth during VRFB operation. Hence, bismuth containing electrodes were characterized at different stages of operation and compared to the reference material. Since the bismuth has a higher absorption of X-ray radiation it is therefore expected to show more intense contrast in the respective radiography than the felt alone. Indeed, the radiography of Bi2-GFD reveals small dark spots which are hardly seen in Fig. 3 a, and which can be attributed to the bismuth oxide deposited inside the felt. With the electrolyte front entering (Fig. 3 b-c) the majority of these particles vanish, suggesting that they are getting dissolved. However, some of these particles even seem to get detached and eluted. These can be spotted as an accumulation of dark spots, which are transported with the rising electrolyte front (cf. the highlighted section of Fig. 3 a and b, shown in a higher magnification in Fig. 3 h). Finally, after a few seconds of purging electrolyte through the cell, no solid bismuth oxide is detected anymore (cf. Fig. 3 d). After 3 min of charging, a complete re-deposition of bismuth (dark domains)

can be detected at the entrance of the cell (cf. Fig. 3 e). This can be explained by the fact that the highest concentration of bismuth will be maintained at the cell entrance where the electrolyte encounters the electrode first. Since a progressing electrolyte front entering the electrode will correlate with an increased contact time and therefore with a decreasing bismuth concentration, the amount of bismuth deposited will get less for larger distances from the entrance, explaining the gradient observed in the radiography images. Consequently, once the deposition is completed, no change during further charging and discharging can be detected. However, bright areas indicate a less flooded state of the electrode after discharging (cf. Fig. 3 f). Due to experimental restrictions in radiography set-up it is again not possible to evaluate whether the less filled pore volume exists at the positive or negative side of the cell or at both sides simultaneously. After pumping the electrolyte at a flow rate of 15 ml min^{-1} for 7 h under OCP conditions at SOC = 0, the deposited bismuth got dissolved again and the fraction of less filled pore volume decreases (cf. Fig. 3 g).

To improve the contrast in the radiography experiments, an electrode containing 10 wt% Bi was operated under the same conditions as the Bi2-GFD (shown in Fig. 4). The respective flooding process of the cell is presented in Fig. 4 a-c. Again the intruding electrolyte (Fig. 4 b-c) dissolves the majority of the bismuth particles and causes their detachment and even flush-out of a minor fraction. This process is depicted in a higher magnification in Fig. 4 h. The accumulation of bismuth in the electrolyte front significantly enhances the contrast (electrolyte front appears darker). After the felt was completely filled (Fig. 4 c), still some bismuth oxide was left which, however, got dissolved completely within 30 s (cf. Fig. 4 d). During the subsequent charging process, again most of the bismuth got deposited at the entrance of the cell forming a gradient with proceeding penetration depth, whitin the first 7 min. However, the increased metal content provides a significantly enhanced contrast when compared to Fig. 3. Again, no dissolution of bismuth could be detected during the discharging process. After discharging and while subsequently pumping the electrolyte at OCP conditions at SOC = 0, the deposited bismuth is dissolved within 9 h (cf. Fig. 4 g). However, in contrast to Fig. 3 the unflooded pore volume gets filled to a larger extent (compare Fig. 3 g and Fig. 4 g).

However, since radiography does not provide any information on the three-dimensional electrode structure, all images depicted in Fig. 4 represent the integral absorption contrast in beam direction only and do

Fig. 3. Radiography of Bi2-GFD at a flow rate of 15 ml min^{-1}; a-c) non-faradaic electrolyte flooding process, d) before galvanostatic charging, e) after galvanostatic charging, f) after galvanostatic discharging at 100 mA cm^{-2}, respectively, g) after electrolyte pumping at 15 ml min^{-1} for 7 h under OCP conditions at SOC = 0, h) high magnification of marked sections of Fig. a/b shows bismuth oxide particles.
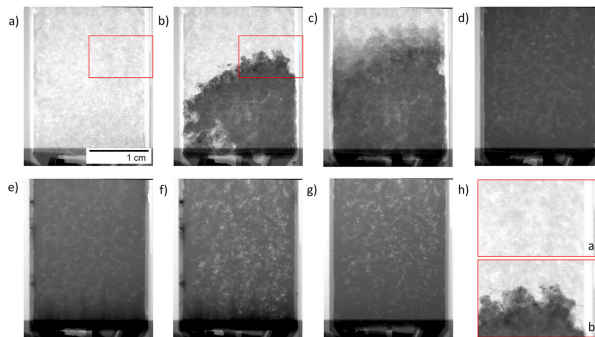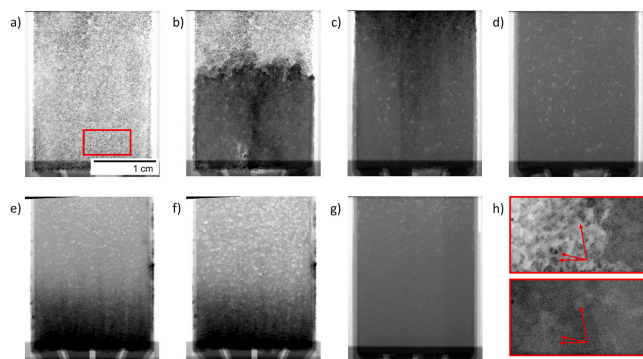
Fig. 4. Radiography of Bi10-GFD at a flow rate of 15 ml min^{-1}; a-c) non-faradaic electrolyte flooding process, d) before galvanostatic charging, e) after galvanostatic charging, f) after galvanostatic discharging at 100 mA cm^{-2}, respectively, g) after electrolyte pumping at 15 ml min^{-1} for 9 h under OCP conditions at SOC = 0, h) high magnification of marked section in panel a) showing the dissolution of bismuth oxide particles.

not allow us to draw conclusions on the spatial distribution. In order to assess the three-dimensional distribution of bismuth deposited into the electrode, X-ray computed tomography was performed for the particular steady states 4 a (dry electrode), 4 d (flooded electrode) and 4 e (after charging). Thereby, 1200 radiographies are recorded during a 360° rotation of the cell and subsequently reconstructed to a three-dimensional model of the cell. These data is provided exemplary in Fig. 5 and in the supporting information as Fig. SI 2 and SI 3, respectively. For the sake of completeness the respective states are also provided for the Bi2-GFD sample as SI 4, SI 5 and SI 7.

In this manner, it can be seen in Fig. 5 that in the dry state of Bi10-GFD all bismuth oxide particles (white spots) were distributed homogenously over the entire electrode area (red xz-plane) prior to operation. However, the projections in blue xy- and green yz-plane reveal that the impregnation of the electrode with bismuth oxide does not penetrate throughout the whole volume of the felt. Consequently, it could be shown that the impregnation method was not suitable to deposit the bismuth oxide particles homogeneously over the entire electrode volume.

Additionally to finding out more about the local distribution of bismuth, the tomography is used to gather three-dimensional information about the unfilled pore volume depicted in Fig. 4 d. Fig. SI 2 reveals a difference in the degree of flooding of the Bi10-GFD (negative electrode) and untreated GFD-UT (positive electrode) felt (the untreated felt is
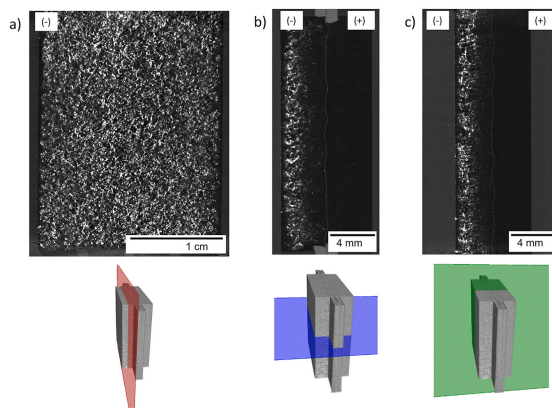

Fig. 5. 3D reconstructed tomography of dry Bi10-GFD cell with corresponding sections, a) red xz-plane, b) blue xy-plane and c) green yz-plane. (For interpretation of the references to colour in this figure legend, the reader is referred to the Web version of this article.)

flooded to a lower degree). Finally, the tomography of the Bi10-GFD (Fig. SI 3) could reveal further insights in the distribution of bismuth, deposited during the galvanostatic charging process as the reconstruction of the three-dimensional representation of the felt electrode allows for a localization of bismuth with high resolution in all spatial dimensions. Thereby, individual domains with a high bismuth content can be resolved and correlated to the carbon felt structure. However, in analogy to Fig. 4 e, Fig. SI 3 confirms that most of the bismuth got deposited at the entrance of the cell and furthermore closer to the current collector with proceeding penetration depth. The same qualitative results could be obtained for the Bi2-GFD sample.

Since bismuth is shown to get readily dissolved and re-deposited, an additional experiment, in which the bismuth oxide was added to the electrolyte and deposited electrochemically, was performed in order to assess the necessity of the pre-testing chemical impregnation step. The flooding process of the respective felt electrode, which did not contain any bismuth, is depicted in Fig. 6 a-c). It can be seen that the flooding occurs homogeneously and nearly no unfilled pore volume is detected in Fig. 6 c. Subsequently to the charging the deposited bismuth is clearly visible (cf. Fig. 6 d). On the right hand side of the cell, darker areas indicate bismuth unintentionally deposited, caused by a flow-by of electrolyte. In analogy to Figs. 3 and 4 (Bi2 und Bi10) a similar behaviour of Bi10ext-GFD during discharging and the following OCP phase is observed. From this perspective, no difference in the electrochemical behaviour would be expected between pre-testing chemically impregnated bismuth and electrochemically deposited bismuth samples. This would render a precipitation or impregnation of bismuth onto the felt material before operation in the cell obsolete.

3.2. Influence of electrolyte flow rate

As presented in Figs. 3 and 4, the radiography imaging of the bismuth re-deposition shows a different distribution pattern for the samples Bi2-GFD and Bi10-GFD. At a higher metal content the bismuth is a) deposited in a thicker layer at the entrance of the cell and b) pushed deeper into the electrode felt. This can be attributed to the 5 times larger metal quantity as compared to Bi2-GFD which allows to maintain the active concentration for a longer time and therefore allows the bismuth to enter deeper inside the electrode. This gives rise to the question whether an increased flow rate will also cause a more homogeneous distribution of the bismuth inside the electrode. For this purpose, Fig. 7 depicts the comparison of the bismuth distribution with respect to different electrolyte flow rates. The respective radiography/tomography results are processed by subtraction of the initial bismuth free cell state from the
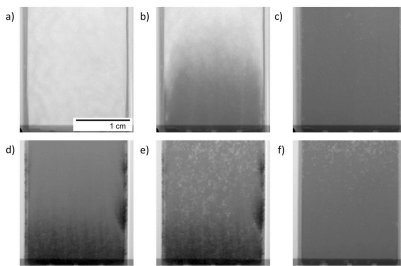

Fig. 6. Radiography of Bi10ext-GFD at a flow rate of 15 ml min^{-1}; a-c) nonfaradaic electrolyte flooding process, d) after galvanostatic charging at 100 mA cm^{-2}, e) after galvanostatic discharging, f) after electrolyte pumping at 15 ml min^{-1} for 7 h under OCP conditions at SOC = 0.

image obtained after the deposition step, in order to show exclusively the deposited bismuth. Furthermore only the concentration of 10 wt% bismuth was investigated in order to provide a sufficiently strong contrast. It can be seen that at a flow rate of 5 ml min^{-1} all bismuth is deposited close to the entrance of the cell (Fig. 7 a). At a flow rate of 15 ml min^{-1} bismuth gets distributed more homogeneously into the felt electrode (Fig. 7 b). Indeed, the most homogeneous distribution was detected by applying a flow rate of 25 ml min^{-1} (Fig. 7 c). The observed influence of the flow rate on the distribution of deposited bismuth can be explained as follows. During the charging process the dissolved bismuth will be electrochemically deposited at the first contact with the electrode. An increased flow rate causes a shorter retention time of electrolyte in the cell. Hence, dissolved bismuth can enter deeper into the electrode before it gets deposited. Consequently, it can be concluded that if bismuth provides any heterogeneous catalytic effect for the V^{2+}/V^{3+} conversion, this influence should be most prominent for the 10 wt% Bi deposited at 25 ml min^{-1}, as this case provides the highest surface area of the felt covered with the desired bismuth particles/deposits.

3.3. Battery testing

Electrochemical characterization of unmodified and bismuth modified electrodes was performed in order to assess the influence of bismuth on the cell performance. The results for each sample are shown in Fig. 8.

The coulombic efficiencies of all samples investigated are similar, regardless of the modification with bismuth or the flow rate. All samples show the same trend, with coulombic efficiencies of 96–96.5% at 25 mA cm^{-2}, increasing to about 99% at current densities of 100 mA cm^{-2} with a maximum deviation of 0.5%, only. Regarding the energy efficiency, at a flow rate of 15 ml min^{-1} an insignificant enhancement is observed for the 2 wt% bismuth containing sample when compared to the unmodified electrode. However, this slight improvement decreases with an increasing current density and vanishes at 100 mA cm^{-2}. In contrast to the bismuth content, increasing the flow rate from 15 ml min^{-1} to 25 ml min^{-1} results in an energy efficiency increase by 0.5% at 25 mA cm^{-2} and up to 5.5% at 100 mA cm^{-2}, respectively. The Bi2-GFD and the Bi2ext-GFD samples show an energy efficiency similar to the pure GFD sample from 25 mA cm^{-2} to 62.5 mA cm^{-2}. However, at larger current densities the energy efficiency of these samples decreases and becomes lower than the one of the unmodified sample. Nevertheless, in case of the Bi2ext-GFD sample, the energy efficiency increases again at a current density of 100 mA cm^{-2} and becomes similar to the unmodified GFD electrode.

The evaluation of discharge power density (Fig. 8 b) reveals the same trend as observed for the energy efficiencies. A difference between the cells operated at different flow rates can be detected at current densities above 62.5 mA cm^{-2}. These differences become more prominent with increasing current density. Samples operated at 15 ml min^{-1} reveal similar discharge power densities. Samples operated at 25 ml min^{-1} flow rate show a discharge power density increased by 5–9 mW cm^{-2} at 100 mA cm^{-2}. However, in all cases the bismuth containing samples do not show a significant improvement in the discharge power densities.

As we could show, X-ray tomography is a powerful tool to investigate the distribution and stability of metal catalysts proposed for application in VRFBs. These investigations can be performed with our presented cell design under various operation conditions. By the combination of results from the X-ray computed radiography/tomography and results obtained from the electrochemical testing, it is now possible to investigate the heterogeneous catalytic effect of different metals in more detail, as shown for the bismuth/bismuth oxide on the V^{2+}/V^{3+} conversion. However, we were not able to detect a significant catalytic effect of bismuth regardless of the deposition pattern, which puts the catalytic effect proposed in the literature into question. Since bismuth/bismuth oxide was demonstrated to be unstable under certain electrochemical conditions but can be, however, re-deposited in the felt electrode during the charging of the cell, we question the necessity of the pre-testing
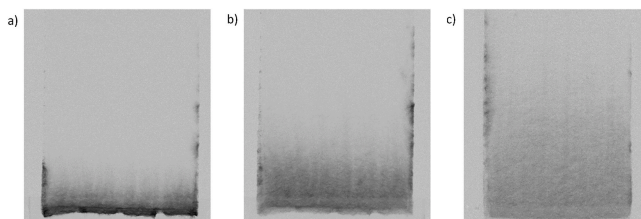
Fig. 7. Influence of flow rate on the deposition pattern of 10 wt% bismuth obtained at a) 5 ml min^{-1}, b) 15 ml min^{-1} and c) 25 ml min^{-1}.
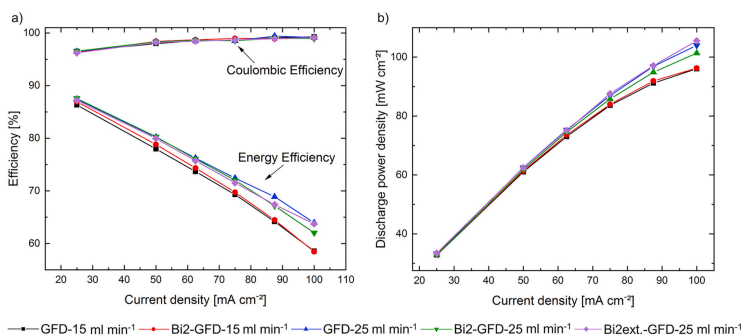

Fig. 8. Comparison of electrochemical battery test results of unmodified and Bi-modified cell configurations a) coulombic and energy efficiency, b) discharge power density, (cf. SI 8 for version with calculated standard deviation).

chemical impregnation steps for felt electrodes applied in the VRFB. Furthermore, the dissolution and re-deposition of bismuth have to be considered when electrochemical tests with electrodes containing bismuth are performed and compared. In this study it is shown that already parameters such as bismuth content or electrolyte flow rate and probably many more (e.g. current density applied during deposition) can have a strong influence on the distribution of catalyst on the felt electrode.

However, these results are not restricted to bismuth only. A comparison of electrodes containing different amounts of catalyst has to consider all mentioned processes. For example a higher catalyst content of a certain material is proposed to lead to a higher VRFB performance. The higher amount of material leads to a different distribution of catalyst that could be the decisive reason for the improved performance. However, the desired reaction surface could be achieved as well by a deposition of less material at a higher electrolyte flow rate. As a result, we suggest to utilize X-ray computed tomography for investigation and determination of the role of suitable catalysts in VRFBs, as many operation parameters strongly affect the resulting cell performance. In that way, it is also possible to evaluate the stability of a proposed catalyst during operation and as a consequence to determine potentially unfavourable operation conditions as it is proposed in a similar manner for lithium-ion batteries [41–43].

4. Summary and conclusions

The distribution and utilization of heterogeneous catalysts are key factors for the improvement of the performance of vanadium redox flow batteries. The in-operando cell design presented in this work successfully demonstrates the capability to determine the catalyst distribution during electrochemical operation, in particular the distribution of bismuth/bismuth oxide during a start-up procedure and a subsequent galvanostatic charging and discharging. In this manner, a dissolution of bismuth oxide decorated onto the felt electrodes was observed. During a subsequent charging process a redeposition was detected. The bismuth distribution pattern remained unchanged during discharging. Subsequently, the redeposited bismuth was dissolved during an OCP phase at SOC = 0. With respect to these results, the requirement for an impregnation pre-treatment of electrodes with bismuth/bismuth oxide has to be questioned, since a similar bismuth distribution could be observed by dissolving the respective amount of bismuth in the electrolyte prior to operation followed by a charging step. Additionally, different distribution patterns for a fixed bismuth concentration could be observed by a variation of the flow rate during deposition. However, these substantially different modes of bismuth distribution were found to not affect the electrochemical performance of the VRFB cell at all. Consequently, we propose to carefully rethink the recently proposed electrocatalytic effect of bismuth. Our results finally underline the necessity of applying imaging techniques, such as radiography and tomography, when the catalytic effect of certain species such as bismuth is discussed and

proposed for application in VRFB systems.

CRediT authorship contribution statement

Marcus Gebhard: Conceptualization, Methodology, Validation, Investigation, Writing - original draft, Visualization, Supervision. **Tim Tichter:** Writing - original draft. **Jonathan Schneider:** Conceptualization. **Jacob Mayer:** Investigation, Formal analysis. **André Hilger:** Software, Validation, Formal analysis, Data curation, Visualization, Supervision. **Markus Osenberg:** Software, Formal analysis, Data curation, Visualization. **Mirko Rahn:** Formal analysis, Visualization. **Ingo Manke:** Project administration, Funding acquisition. **Christina Roth:** Conceptualization, Project administration, Funding acquisition.

Declaration of competing interest

The authors declare that they have no known competing financial interests or personal relationships that could have appeared to influence the work reported in this paper.

Appendix A. Supplementary data

Supplementary data to this article can be found online at https://doi.org/10.1016/j.jpowsour.2020.228695.

References

[1] Z. Zhang, J. Xi, H. Zhou, X. Qiu, KOH etched graphite felt with improved wettability and activity for vanadium flow batteries, Electrochim. Acta 218 (2016) 15–23, https://doi.org/10.1016/j.electacta.2016.09.099.

[2] C. Flox, M. Skoumal, T. Andreu, J. Ramo, J. Rubio-garci, Thermo – chemical treatments based on NH₃/O₂ for improved graphite-based fiber electrodes in vanadium redox flow batteries, Carbon 60 (2013) 280–288, https://doi.org/10.1016/j.carbon.2013.04.038.

[3] T. Wu, K. Huang, S. Liu, S. Zhuang, Hydrothermal ammoniated treatment of PAN-graphite felt for vanadium redox flow battery, J. Solid State Electrochem. 16 (2012) 579–585, https://doi.org/10.1007/s10008-011-1383-y.

[4] L. Yue, W. Li, F. Sun, Highly hydroxylated carbon fibres as electrode materials of all-vanadium redox flow battery, Carbon 48 (2010) 3079–3090, https://doi.org/10.1016/j.carbon.2010.04.044.

[5] C. Gao, N. Wang, S. Peng, S. Liu, Y. Lei, X. Liang, S. Zeng, H. Zi, Influence of Fenton's reagent treatment on electrochemical properties of graphite felt for all vanadium redox flow battery, Electrochim. Acta 88 (2013) 193–202, https://doi.org/10.1016/j.electacta.2012.10.021.

[6] E.-M. Hammer, B. Berger, L. Komsiyska, Improvement of the performance of graphite felt electrodes for vanadium-redox-flow-batteries by plasma treatment, Int. J. Renew. Energy Dev. 3 (2014) 7–12, https://doi.org/10.14710/ijred.3.1.7-12.

[7] D. Dixon, D. Babu, J. Langner, M. Bruns, L. Pfaffmann, A. Bhaskar, J. Schneider, F. Scheiba, H. Ehrenberg, Effect of oxygen plasma treatment on the electrochemical performance of the rayon and polyacrylonitrile based carbon felt for the vanadium redox flow battery application, J. Power Sources 332 (2016) 240–248, https://doi.org/10.1016/j.jpowsour.2016.09.070.

[8] D.-S. Yang, J. Hee, J. Woo, J. Yong, D.-g. Kim, D. Hack, B. Gak, T.-h. Kim, Y. Taik, Multimodal porous and nitrogen-functionalized electrode based on graphite felt modified with carbonized porous polymer skin layer for all-vanadium redox flow battery, Mater, Today Energy 11 (2019) 159–165, https://doi.org/10.1016/j.mtener.2018.11.003.

[9] K.M. Tenny, V.S. Lakhanpal, R.P.D. Jr, V. Yarlagadda, T.V. Nguyen, Impact of multi-walled carbon nanotube fabrication on carbon cloth electrodes for hydrogen-vanadium reversible fuel cells, J. Am. Chem. Soc. 164 (2017) 2534–2538, https://doi.org/10.1149/2.1151712jes.

[10] L. Wei, T.S. Zhao, G. Zhao, L. An, L. Zeng, A high-performance carbon nanoparticle-decorated graphite felt electrode for vanadium redox flow batteries, Appl. Energy 176 (2016) 74–79, https://doi.org/10.1016/j.apenergy.2016.05.048.

[11] G. Zoraida, C. Flox, C. Blanco, M. Granda, J.R. Morante, M. Rosa, S. Ricardo, Outstanding electrochemical performance of a graphene-modified graphite felt for vanadium redox flow battery application, J. Power Sources 338 (2016) 155–162, https://doi.org/10.1016/j.jpowsour.2016.10.069.

[12] S. Park, H. Kim, Fabrication of nitrogen-doped graphite felts as positive electrodes using polypyrrole as a coating agent in vanadium redox flow batteries, J. Mater. Chem. (2015) 12276–12283, https://doi.org/10.1039/C5TA02674A, 03.

[13] W. Li, J. Liu, C. Yan, Reduced graphene oxide with tunable C/O ratio and its activity towards vanadium redox pairs for an all vanadium redox flow battery, Carbon 55 (2013) 313–320, https://doi.org/10.1016/j.carbon.2012.12.069.

[14] L. Xia, Q. Zhang, C. Wu, Y. Liu, M. Ding, J. Ye, Y. Cheng, C. Jia, Graphene coated carbon felt as a high-performance electrode for all vanadium redox flow batteries, Surf. Coating. Technol. 358 (2019) 153–158, https://doi.org/10.1016/j.surfcoat.2018.11.024.

[15] B. Li, Z. Nie, Y. Shao, Q. Luo, X. Wei, X. Li, J. Xiao, C. Wang, V. Sprenkle, W. Wang, Bismuth nanoparticle decorating graphite felt as a high-performance electrode for an all-vanadium redox flow battery, Nano Lett. 13 (2013) 1330–1335, https://doi.org/10.1021/nl400223v.

[16] D.J. Suarez, Z. Gonzalez, C. Blanco, M. Granda, R. Menendez, Graphite felt modified with bismuth nanoparticles as negative electrode in a vanadium redox flow battery, ChemSusChem 7 (2014) 914–918, https://doi.org/10.1002/cssc.201301045.

[17] H.R. Jiang, Y.K. Zeng, M.C. Wu, W. Shyy, T.S. Zhao, A uniformly distributed bismuth nanoparticle-modified carbon cloth electrode for vanadium redox flow batteries, Appl. Energy 240 (2019) 226–235, https://doi.org/10.1016/j.apenergy.2019.02.051.

[18] S. Moon, B.W. Kwon, Y. Chung, Y. Kwon, Effect of bismuth sulfate coated on acidified CNT on performance of vanadium redox flow battery, J. Electrochem. Soc. 12 (2019) A2602–A2609, https://doi.org/10.1149/2.1181912jes.

[19] X. Yang, T. Liu, C. Xu, H. Zhang, X. Li, H. Zhang, The catalytic effect of bismuth for VO₂⁺/VO²⁺ and V³⁺/V²⁺ redox couples in vanadium flow batteries, J. Energy Chem. 26 (2017) 1–7, https://doi.org/10.1016/j.jechem.2016.09.007.

[20] Z. He, M. Li, Y. Li, J. Zhu, Y. Jiang, W. Meng, Electrochimica Acta Flexible electrospun carbon nanofiber embedded with TiO₂ as excellent negative electrode for vanadium redox flow battery, Electrochim. Acta 281 (2018) 601–610, https://doi.org/10.1016/j.electacta.2018.06.011.

[21] T.-M. Tseng, R.-H. Huang, C.-Y. Huang, C.-C. Liu, Carbon felt coated with titanium dioxide/carbon black composite as negative electrode for vanadium redox flow, J. Electrochem. Soc. 161 (2014) 1132–1138, https://doi.org/10.1149/2.102406jes.

[22] P.C. Ghimire, R. Schweiss, N. Wai, T.M. Lim, A. Bhattarai, T.D. Nguyen, Q. Yan, Titanium carbide-decorated graphite felt as high performance negative electrode in vanadium redox flo w batteries, J. Mater. Chem. 6 (2018) 6625–6632, https://doi.org/10.1039/C8TA00464A.

[23] B. Li, M. Gu, Z. Nie, X. Wei, C. Wang, V. Sprenkle, W. Wang, Nanorod niobium oxide as powerful catalysts for an all vanadium redox flow battery, Nano Lett. 14 (2014) 158–165, https://doi.org/10.1021/nl403674a.

[24] Y. Jiang, X. Feng, G. Cheng, C. Li, Y. Li, Z. He, J. Zhu, W. Meng, H. Zhou, L. Dai, L. Wang, Electrocatalytic activity of Mno₂ nanosheet array-decorated carbon paper as superior negative electrode for vanadium redox flow batteries, Electrochim. Acta 322 (2019) 134754, https://doi.org/10.1016/j.electacta.2019.134754.

[25] H. Zhou, Y. Shen, J. Xi, X. Qiu, L. Chen, ZrO₂ - nanoparticle-modified graphite felt: bifunctional effects on vanadium flow batteries, ACS Appl. Mater. Interfaces 24 (2016) 15369–15378, https://doi.org/10.1021/acsami.6b03761.

[26] L. Yu, F. Lin, W. Xiao, L. Xu, J. Xi, Achieving efficient and inexpensive vanadium flow battery by combining CexZr1-xO₂ electrocatalyst and hydrocarbon membrane, Chem. Eng. J. 356 (2019) 622–631, https://doi.org/10.1016/j.cej.2018.09.069.

[27] P. Delahay, M. Pourbaix, P. van rysselberghe, Potential-pH diagrams, J. Chem. Educ. 12 (1950) 683, https://doi.org/10.1021/ed027p683.

[28] N. Takeno, Atlas of eh-ph diagrams, URL, https://www.nrc.gov/docs/ML1808/ML18089A638.pdf, 2005.

[29] J. Banhart, Advanced Tomographic Methods in Materials Research and Engineering, Oxford University Press, Oxford (NY) U.S.A., 2008.

[30] S.R. Stock, Recent advances in X-ray microtomography applied to materials, Int. Mater. Rev. 3 (2008) 129–181, https://doi.org/10.1179/174328008X277803.

[31] E. Maire, P. Withers, Quantitative X-ray tomography, Int. Mater. Rev. 1 (2014) 1–43, https://doi.org/10.1179/1743280413Y.000000023.

[32] R. Banerjee, N. Bevilacqua, A. M, B. Wiedermann, F. Wilhelm, J. Scholta, R. Zeis, Carbon felt electrodes for redox flow battery: impact of compression on transport properties, J. Energy Storage 26 (2019) 100997, https://doi.org/10.1016/j.est.2019.100997.

[33] N. Bevilacqua, L. Eifert, R. Banerjee, K. Köble, T. Farago, M. Zuber, A. Bazylak, R. Zeis, Visualization of electrolyte flow in vanadium redox flow batteries using synchrotron X-ray radiograph and tomography - impact of electrolyte species and electrode compression, J. Power Sources 439 (2019) 227071, https://doi.org/10.1016/j.jpowsour.2019227071.

[34] R. Jervis, L.D. Brown, T.P. Neville, J. Millichamp, D.P. Finegan, T.M.M. Heenan, D. J.L. Brett, P.R. Shearing, Design of a miniature flow cell for in-situ x-ray imaging of

redox flow batteries, J. Phys. D Appl. Phys. 49 (2016) 434002, https://doi.org/10.1088/0022-3727/49/43/434002.

[35] P. Trogadas, O. Taiwo, B. Tjaden, T. Neville, S. Yun, J. Parrondo, V. Ramani, M. Coppens, D. Brett, P. Shearing, X-ray micro-tomography as a diagnostic tool for the electrode degradation in vanadium redox flow batteries, Electrochem. Commun. 48 (2014) 155–159, https://doi.org/10.1016/j.elecom.2014.09.010.

[36] M. Gebhard, M. Schnucklake, A. Hilger, M. Röhe, M. Osenberg, U. Krewer, I. Manke, C. Roth, X-ray computed radiography and tomography study of electrolyte invasion and distribution inside pristin and heat-treated carbon felts for redox flow batteries, Energy Technol. 3 (2020) 1901214, https://doi.org/10.1002/ente.201901214.

[37] J. Schneider, E. Bulczak, G. El-Nagar, M. Gebhard, P. Kubella, M. Schnucklake, A. Fetyan, I. Derr, C. Roth, Degradation phenomena of bismuth-modified felt electrodes in VRFB studied by electrochemical impedance spectroscopy, Batteries 5 (2019) 16, https://doi.org/10.3390/batteries5010016.

[38] K. Heiland, D.J.T. Hill, J.H. O'Donnell, P.J. Pomery, Radiation degradation of Poly (arylene ether ketone)s, Polym, Adv. Met. Technol. 2 (1994) 116–121, https://doi.org/10.1002/pat.1994.220050206.

[39] J. Schindelin, I. Arganda-Carreras, E. Frise, V. Kaynig, M. Longair, T. Pietzsch, S. Preibisch, C. Rueden, S. Saalfeld, B. Schmid, J.-Y. Tinevez, D.J. White,

V. Hartenstein, K. Eliceiri, P. Tomancak, A. Cordana, Fiji: an open-source platform for biological-image analysis, Nat. Methods 7 (2012) 676–682, https://doi.org/10.1038/nmeth.2019.

[40] J. Vlassenbroeck, M. Dierick, B. Masschaele, V. Cnudde, L. van Hoorebeke, P. Jacobs, Software tools for quantification of X-ray microtomography at the UGCT, Nucl. Instrum. Methods Phys. Res., Sect. A 1 (2007) 442–445, https://doi.org/10.1016/j.nima.2007.05.073.

[41] R. Hausbrand, G. Cherkashinin, H. Ehrenberg, M. Gröting, K. Albe, C. Hess, W. Jaegermann, Fundamental degradation mechanism of layered oxide Li-ion battery cathode materials: Methodology, insights and novel approaches, Mater. Sci. Eng., B 192 (2015) 3–25, https://doi.org/10.1016/j.mseb.2014.11.014.

[42] S. Tippmann, D. Walper, L. Balboa, B. Spier, W.G. Bessler, Low-temperature charging of lithium-ion cells part I: electrochemical modeling and experimental investigation of degradation behavior, J. Power Sources 252 (2014) 305–316, https://doi.org/10.1016/j.powsour.2013.12.022.

[43] F. Martel, Y. Dubé, S. Kelouwani, J. Jaguemont, K. Agbossou, Long-term assessment of economic plug-in hybrid electric vehicle battery lifetime degradation management through near optimal fuel cell load sharing, J. Power Sources 318 (2016) 270–282, https://doi.org/10.1016/j.powsour.2016.04.029.

Chapter 6

Conclusion and Outlook

Within this thesis, a sound foundation for robust determination of electrode kinetics in the context of VRFB research has been established by exploring the manifold capabilities of sophisticated, mainly EIS-based, electrochemical concepts, providing the necessary theoretical background as well as discussing experimental pitfalls and related mitigation strategies. The threefold challenge successfully addressed in the process consisted of: discriminating effects of wetting from actual changes in k^0, assessing long-term stability of electrode materials or modifications made thereto and separating contributions of desired electrode processes from those of parasitic side reactions.

It was demonstrated how applying a normalization approach enables gathering valid and reproducible results from *ex-situ* EIS. During an exemplary study of Bi-modified carbon felt electrodes, the intrinsic electrocatalytic activity of bismuth towards the V(II)/V(III) redox reaction was thus verified while eliminating any interference caused by altered wetting behaviour. However, further results indicated poor stability of bismuth particles and, related to that, a possibly accelerating effect on electrode degradation. Using complementary imaging techniques, the dissolution of bismuth upon electroless contact with electrolyte was confirmed. The observed redeposition during a subsequent charge/discharge cycle appeared to be governed by the current density distribution across the electrode area. It was proposed that said distribution, mainly caused by con-

centration gradients inherently present in any type of flow cell, constitutes a significant root of electrode degradation in VRFB. Further activities to verify this proposition had been launched, featuring a novel flow cell designed to accommodate deliberately narrow but long pieces of carbon felt in order to enlarge aforementioned concentration gradients. However, albeit yielding encouraging initial results, those studies couldn't be advanced to completion within the given time frame.

The capabilities of EIS regarding *in-situ* characterization of VRFB electrodes were significantly enhanced by introducing the concept of DRT analysis. Employing the latter allowed for indiscriminately determining the kinetic contribution of the negative half cell electrode to the overall cell impedance. At least with the combination of materials and operational conditions used herein, said electrode was verified to be the sole source of kinetic limitation. This insight was used to selectively monitor its degradation during operation of a VRFB without the need to make any modifications to the test setup. Having established the use of DRT analysis and demonstrated how to take advantage of this powerful approach in the context of VRFB research opens up immense possibilities for follow-up studies. Future applications involve e.g. benchmarking kinetic properties of different carbon-based electrode materials under realistic operating conditions, comparing effects of chemical aging and electrochemical degradation or characterizing entire cell stacks. Full impedance spectra could be obtained within few seconds by employing time domain measurements, effectively enabling real time DRT analysis of a VRFB (or any other electrochemical system) during operation. Another possible scenario is the utilization of segmented cells to determine a locally resolved DRT which would ultimately allow for studying the interplay of current density distribution and electrode degradation in the most elegant way. Investigations in all of those directions had been initiated, however, time proved once again to be the limiting factor.

It should be pointed out that throughout this thesis, EIS has been considered only in its classical form. That is to say, experimental excitation amplitudes were kept sufficiently small to exclusively study linear system behaviour, meaning that any response to higher harmonics of the excitation frequency was omitted. However, the exploration of such non-linear responses, although beyond the scope of this work, bears enormous potential to yield valuable insights in the near future. This was hinted at by the use of ACCV during investigation of V^{3+}-reduction and simultaneous HER at different model electrodes. Therefore, further application of this technique is expected to offer great advantages for the study of practically relevant carbon felt electrodes as well.

Bibliography

[1] UNITED NATIONS FRAMEWORK CONVENTION ON CLIMATE CHANGE, What is the Kyoto Protocol?, `https://unfccc.int/kyoto_protocol` (visited on 12/16/2022).

[2] UNITED NATIONS FRAMEWORK CONVENTION ON CLIMATE CHANGE, The Paris Agreement, `https://unfccc.int/process-and-meetings/the-paris-agreement/the-paris-agreement` (visited on 12/16/2022).

[3] STATISTA, Verteilung der Treibhausgasemissionen weltweit nach Quellgruppe im Jahr 2019, `https://de.statista.com/statistik/daten/studie/168588/umfrage/verteilung-der-emissionen-von-treibhausgasen-nach-sektoren-weltweit/` (visited on 12/16/2022).

[4] EUROPEAN PARLIAMENT, Greenhouse gas emissions by country and sector, `https://www.europarl.europa.eu/news/en/headlines/society/20180301STO98928/greenhouse-gas-emissions-by-country-and-sector-infographic` (visited on 12/16/2022).

[5] FRAUNHOFER ISE, Nettostromerzeugung in Deutschland 2021, `https://www.ise.fraunhofer.de/de/presse-und-medien/news/2022/nettostromerzeugung-in-deutschland-2021-erneuerbare-energien-witterungsbedingt-schwaecher.html` (visited on 12/16/2022).

[6] BUNDESMINISTERIUM FÜR WIRTSCHAFT UND KLIMASCHUTZ, Klimaschutzplan 2050, `https://www.bmwk.de/Redaktion/DE/Artikel/Industrie/klimaschutz-klimaschutzplan-2050.html` (visited on 12/16/2022).

[7] S. Hameer, J. L. van Niekerk, *Int. J. Energy Res.* **2015**, 39, 1179–1195, DOI `10.1002/er.3294`.

[8] T. M. Gür, *Energy Environ. Sci.* **2018**, 11, 2696–2767, DOI `10.1039/C8EE01419A`.

[9] Pacific Northwest National Laboratory, 2020 Grid Energy Storage Technology Cost and Performance Assessment, **2020**, `https://www.energy.gov/energy-storage-grand-challenge/downloads/2020-grid-energy-storage-technology-cost-and-performance` (visited on 12/16/2022).

[10] P. Alotto, M. Guarnieri, F. Moro, *Renewable Sustainable Energy Rev.* **2014**, 29, 325–335, DOI `10.1016/j.rser.2013.08.001`.

[11] V. Viswanathan, A. Crawford, D. Stephenson, S. Kim, W. Wang, B. Li, G. Coffey, E. Thomsen, G. Graff, P. Balducci, M. Kintner-Meyer, V. Sprenkle, *J. Power Sources* **2014**, 247, 1040–1051, DOI `10.1016/j.jpowsour.2012.12.023`.

[12] W. Kangro, *German pat.*, DE914264C, **1954**.

[13] M.-A. Goulet, E. Kjeang, *J. Power Sources* **2014**, 260, 186–196, DOI `10.1016/j.jpowsour.2014.03.009`.

[14] S. Weber, J. F. Peters, M. Baumann, M. Weil, *Environ. Sci. Technol.* **2018**, 52, 10864–10873, DOI `10.1021/acs.est.8b02073`.

[15] C. Minke, U. Kunz, T. Turek, *J. Power Sources* **2017**, 361, 105–114, DOI `10.1016/j.jpowsour.2017.06.066`.

[16] D. Dueerkop, H. Widdecke, C. Schilde, U. Kunz, A. Schmiemann, *Membranes* **2021**, 11, 214, DOI `10.3390/membranes11030214`.

[17] J. T. Clement, D. S. Aaron, M. M. Mench, *J. Electrochem. Soc.* **2016**, 163, A5220–A5228, DOI `10.1149/2.0241601jes`.

[18] N. Gurieff, D. F. Keogh, V. Timchenko, C. Menictas, *Molecules* **2019**, 24, DOI `10.3390/molecules24213877`.

[19] N. Gurieff, D. F. Keogh, M. Baldry, V. Timchenko, D. Green, I. Koskinen, C. Menictas, *Appl. Sci.* **2020**, 10, 2801, DOI `10.3390/app10082801`.

[20] T. Gerber, P. Fischer, K. Pinkwart, J. Tübke, *Batteries* **2019**, 5, 38, DOI `10.3390/batteries5020038`.

[21] X. Ke, J. M. Prahl, J. I. D. Alexander, R. F. Savinell, *Electrochim. Acta* **2017**, 223, 124–134, DOI `10.1016/j.electacta.2016.12.017`.

[22] S. Kumar, S. Jayanti, *J. Power Sources* **2016**, 307, 782–787, DOI `10.1016/j.jpowsour.2016.01.048`.

[23] S. Maurya, P. T. Nguyen, Y. S. Kim, Q. Kang, R. Mukundan, *J. Power Sources* **2018**, 404, 20–27, DOI `10.1016/j.jpowsour.2018.09.093`.

[24] C. R. Dennison, E. Agar, B. Akuzum, E. C. Kumbur, *J. Electrochem. Soc.* **2016**, 163, A5163–A5169, DOI `10.1149/2.0231601jes`.

[25] J. Houser, A. Pezeshki, J. T. Clement, D. Aaron, M. M. Mench, *J. Power Sources* **2017**, 351, 96–105, DOI `10.1016/j.jpowsour.2017.03.083`.

[26] A. M. Pezeshki, R. L. Sacci, F. M. Delnick, D. S. Aaron, M. M. Mench, *Electrochim. Acta* **2017**, 229, 261–270, DOI `10.1016/j.electacta.2017.01.056`.

[27] J. Noack, N. Roznyatovskaya, T. Herr, P. Fischer, *Angew. Chem. Int. Ed.* **2015**, 54, 9776–9809, DOI `10.1002/anie.201410823`.

[28] F. Pan, Q. Wang, *Molecules* **2015**, 20, 20499–20517, DOI `10.3390/molecules201119711`.

[29] Y. A. Gandomi, D. S. Aaron, J. R. Houser, M. C. Daugherty, J. T. Clement, A. M. Pezeshki, T. Y. Ertugrul, D. P. Moseley, M. M. Mench, *J. Electrochem. Soc.* **2018**, 165, A970–A1010, DOI `10.1149/2.0601805JES`.

[30] Vanitec, Global VRFB Installations Database & Map, `https://vanitec.org/vanadium/map` (visited on 12/16/2022).

[31] I. Todorović, Vanadium flow megabattery comes online in China, `https://balkangreenenergynews.com/vanadium-flow-megabattery-comes-online-in-china/` (visited on 12/16/2022).

[32] M. Skyllas-Kazacos, *J. Electrochem. Soc.* **1986**, 133, 1057, DOI `10.1149/1.2108706`.

[33] K. W. Knehr, E. C. Kumbur, *Electrochem. Commun.* **2011**, 13, 342–345, DOI `10.1016/j.elecom.2011.01.020`.

[34] R. M. Wittman, M. L. Perry, T. N. Lambert, B. R. Chalamala, Y. Preger, *J. Electrochem. Soc.* **2020**, 167, 090545, DOI 10.1149/1945-7111/ab9406.

[35] S. Roe, C. Menictas, M. Skyllas-Kazacos, *J. Electrochem. Soc.* **2015**, 163, 5023–5028, DOI 10.1149/2.0041601jes.

[36] M. V. Holland-Cunz, F. Cording, J. Friedl, U. Stimming, *Front. Energy* **2018**, 12, 198–224, DOI 10.1007/s11708-018-0552-4.

[37] M. Vijayakumar, L. Li, G. Graff, J. Liu, H. Zhang, Z. Yang, J. Z. Hu, *J. Power Sources* **2011**, 196, 3669–3672, DOI 10.1016/j.jpowsour.2010.11.126.

[38] M. Skyllas-Kazacos, L. Cao, M. Kazacos, N. Kausar, A. Mousa, *ChemSusChem* **2016**, 9, 1521–1543, DOI 10.1002/cssc.201600102.

[39] C. Choi, S. Kim, R. Kim, Y. Choi, S. Kim, H.-y. Jung, J. H. Yang, H.-T. Kim, *Renewable Sustainable Energy Rev.* **2017**, 69, 263–274, DOI 10.1016/j.rser.2016.11.188.

[40] A. A. Shah, H. Al-Fetlawi, F. C. Walsh, *Electrochim. Acta* **2010**, 55, 1125–1139, DOI 10.1016/j.electacta.2009.10.022.

[41] C.-N. Sun, F. M. Delnick, L. Baggetto, G. M. Veith, Zawodzinski, Thomas A., Jr., *J. Power Sources* **2014**, 248, 560–564, DOI 10.1016/j.jpowsour.2013.09.125.

[42] R. Schweiss, A. Pritzl, C. Meiser, *J. Electrochem. Soc.* **2016**, 163, A2089–A2094, DOI 10.1149/2.1281609jes.

[43] A. Fetyan, G. A. El-Nagar, I. Lauermann, M. Schnucklake, J. Schneider, C. Roth, *J. Energy Chem.* **2019**, 32, 57–62, DOI 10.1016/j.jechem.2018.06.010.

[44] T. Tichter, J. Schneider, D. Nguyen Viet, A. Diaz Duque, C. Roth, *J. Electroanal. Chem.* **2020**, 859, 113843, DOI 10.1016/j.jelechem.2020.113843.

[45] M. P. J. Brennan, O. R. Brown, *J. Appl. Electrochem.* **1972**, 2, 43, DOI 10.1007/bf00615191.

[46] T. Janoschka, N. Martin, M. D. Hager, U. S. Schubert, *Angew. Chem. Int. Ed.* **2016**, 55, 14427–14430, DOI 10.1002/anie.201606472.

[47] T. Janoschka, C. Friebe, M. D. Hager, U. S. Schubert, N. Martin, *ChemistryOpen* **2017**, 6, 216–220.

[48] B. Hu, C. DeBruler, Z. Rhodes, T. L. Liu, *J. Am. Chem. Soc.* **2017**, 139, 1207–1214, DOI 10.1021/jacs.6b10984.

[49] Y. Ding, G. Yu, *Angew. Chem. Int. Ed.* **2017**, 56, 8614–8616, DOI 10.1002/anie.201701254.

[50] S. Gentil, D. Reynard, H. H. Girault, *Curr. Opin. Electrochem.* **2020**, 21, 7–13, DOI 10.1016/j.coelec.2019.12.006.

[51] F. R. Brushett, M. J. Aziz, K. E. Rodby, *ACS Energy Lett.* **2020**, 5, 879–884, DOI 10.1021/acsenergylett.0c00140.

[52] J. Wu, X. Z. Yuan, H. Wang, M. Blanco, J. J. Martin, J. Zhang, *Int. J. Hydrogen Energy* **2008**, 33, 1735–1746, DOI 10.1016/j.ijhydene.2008.01.013.

[53] D. Aaron, Z. Tang, A. B. Papandrew, T. A. Zawodzinski, *J. Appl. Electrochem.* **2011**, 41, 1175, DOI 10.1007/s10800-011-0335-7.

[54] J. A. V. Butler, *Trans. Faraday Soc.* **1924**, 19, 729–733, DOI 10.1039/TF9241900729.

[55] T. Erdey-Grúz, M. Volmer, *Z. Phys. Chem.* **1930**, 150A, 203–213, DOI 10.1515/zpch-1930-15020.

[56] A. J. Bard, L. R. Faulkner, *Electrochemical methods: Fundamentals and applications*, 2nd Edition, Wiley, Hoboken, NJ, **2001**.

[57] J. H. Lehman, M. Terrones, E. Mansfield, K. E. Hurst, V. Meunier, *Carbon* **2011**, 49, 2581–2602, DOI 10.1016/j.carbon.2011.03.028.

[58] H. Fink, J. Friedl, U. Stimming, *J. Phys. Chem. C* **2016**, 120, 15893–15901, DOI 10.1021/acs.jpcc.5b12098.

[59] J. Friedl, C. M. Bauer, A. Rinaldi, U. Stimming, *Carbon* **2013**, 63, 228–239, DOI 10.1016/j.carbon.2013.06.076.

[60] J. Friedl, U. Stimming, *Electrochim. Acta* **2017**, 227, 235–245, DOI 10.1016/j.electacta.2017.01.010.

[61] M. Ulaganathan, V. Aravindan, Q. Yan, S. Madhavi, M. Skyllas-Kazacos, T. M. Lim, *Adv. Mater. Interfaces* **2016**, 3, DOI 10.1002/admi.201500309.

[62] M. Ulaganathan, A. Jain, V. Aravindan, S. Jayaraman, W. C. Ling, T. M. Lim, M. P. Srinivasan, Q. Yan, S. Madhavi, *J. Power Sources* **2015**, 274, 846–850, DOI 10.1016/j.jpowsour.2014.10.176.

[63] M. Maharjan, A. Bhattarai, M. Ulaganathan, N. Wai, M. O. Oo, J.-Y. Wang, T. M. Lim, *J. Power Sources* **2017**, 362, 50–56, DOI `10.1016/j.jpowsour.2017.07.020`.

[64] Y. Jiang, Y. Li, J. Zhu, Z. He, W. Meng, H. Zhou, L. Wang, L. Dai, *J. Electrochem. Soc.* **2018**, 165, A1813–A1821, DOI `10.1149/2.1221809jes`.

[65] V. Krikstolaityte, O. Joshua, A. Veksha, N. Wai, G. Lisak, T. Lim, *Batteries* **2018**, 4, 56, DOI `10.3390/batteries4040056`.

[66] H. Song, H. Li, H. Wang, J. Key, S. Ji, X. Mao, R. Wang, *Electrochim. Acta* **2014**, 147, 520–526, DOI `10.1016/j.electacta.2014.09.146`.

[67] R. Schweiss, C. Meiser, F. W. T. Goh, *ChemElectroChem* **2017**, 4, 1969–1974, DOI `10.1002/celc.201700280`.

[68] J.-B. Donnet, *Carbon fibers*, 3rd Edition, M. Dekker, New York, **1998**.

[69] S.-J. Park, *Carbon fibers*, Springer, Dordrecht, **2015**.

[70] F. Liu, H. Wang, L. Xue, L. Fan, Z. Zhu, *J. Mater. Sci.* **2008**, 43, 4316–4322, DOI `10.1007/s10853-008-2633-y`.

[71] R. L. McCreery, *Chem. Rev.* **2008**, 108, 2646–2687, DOI `10.1021/cr068076m`.

[72] W. Yuan, Y. Zhou, Y. Li, C. Li, H. Peng, J. Zhang, Z. Liu, L. Dai, G. Shi, *Sci. Rep.* **2013**, 3, 2248, DOI `10.1038/srep02248`.

[73] N. Pour, D. G. Kwabi, T. Carney, R. M. Darling, M. L. Perry, Y. Shao-Horn, *J. Phys. Chem. C* **2015**, 119, 5311–5318, DOI `10.1021/jp5116806`.

[74] G. Wei, W. Su, Z. Wei, X. Fan, J. Liu, C. Yan, *Electrochim. Acta* **2016**, 204, 263–269, DOI `10.1016/j.electacta.2016.04.081`.

[75] M.-A. Goulet, M. Skyllas-Kazacos, E. Kjeang, *Carbon* **2016**, 101, 390–398, DOI `10.1016/j.carbon.2016.02.011`.

[76] B. Sun, M. Skyllas-Kazacos, *Electrochim. Acta* **1992**, 37, 1253–1260, DOI `10.1016/0013-4686(92)85064-R`.

[77] B. Sun, M. Skyllas-Kazacos, *Electrochim. Acta* **1992**, 37, 2459–2465, DOI `10.1016/0013-4686(92)87084-D`.

[78] P. Mazúr, J. Mrlík, J. Beneš, J. Pocedič, J. Vrána, J. Dundálek, J. Kosek, *J. Power Sources* **2018**, 380, 105–114, DOI `10.1016/j.jpowsour.2018.01.079`.

[79] A. Bourke, M. A. Miller, R. P. Lynch, J. S. Wainright, R. F. Savinell, D. N. Buckley, *J. Electrochem. Soc.* **2015**, 162, A1547–A1555, DOI `10.1149/2.0671508jes`.

[80] A. Bourke, M. A. Miller, R. P. Lynch, X. Gao, J. Landon, J. S. Wainright, R. F. Savinell, D. N. Buckley, *J. Electrochem. Soc.* **2016**, 163, A5097–A5105, DOI `10.1149/2.0131601jes`.

[81] D. N. Buckley, A. Bourke, R. P. Lynch, N. Quill, M. A. Miller, J. S. Wainright, R. F. Savinell, *MRS Adv.* **2017**, 2, 1131–1142, DOI `10.1557/adv.2017.176`.

[82] L. Yue, W. Li, F. Sun, L. Zhao, L. Xing, *Carbon* **2010**, 48, 3079–3090, DOI `10.1016/j.carbon.2010.04.044`.

[83] A. Di Blasi, O. Di Blasi, N. Briguglio, A. S. Aricò, D. Sebastián, M. J. Lázaro, G. Monforte, V. Antonucci, *J. Power Sources* **2013**, 227, 15–23, DOI `10.1016/j.jpowsour.2012.10.098`.

[84] C. Flox, J. Rubio-García, M. Skoumal, T. Andreu, J. R. Morante, *Carbon* **2013**, 60, 280–288, DOI `10.1016/j.carbon.2013.04.038`.

[85] Z. Zhang, J. Xi, H. Zhou, X. Qiu, *Electrochim. Acta* **2016**, 218, 15–23, DOI `10.1016/j.electacta.2016.09.099`.

[86] L. Dai, Y. Jiang, W. Meng, H. Zhou, L. Wang, Z. He, *Appl. Surf. Sci.* **2017**, 401, 106–113, DOI `10.1016/j.apsusc.2017.01.002`.

[87] E.-M. Hammer, B. Berger, L. Komsiyska, *Int. J. Renew. Energy Dev.* **2014**, 3, 7–12, DOI `10.14710/ijred.3.1.7-12`.

[88] D. Dixon, D. J. Babu, J. Langner, M. Bruns, L. Pfaffmann, A. Bhaskar, J. J. Schneider, F. Scheiba, H. Ehrenberg, *J. Power Sources* **2016**, 332, 240–248, DOI `10.1016/j.jpowsour.2016.09.070`.

[89] M. Park, I.-Y. Jeon, J. Ryu, H. Jang, J.-B. Back, J. Cho, *Nano Energy* **2016**, 26, 233–240, DOI `10.1016/j.nanoen.2016.05.027`.

[90] Y. Shao, X. Wang, M. Engelhard, C. Wang, S. Dai, J. Liu, Z. Yang, Y. Lin, *J. Power Sources* **2010**, 195, 4375–4379, DOI `10.1016/j.jpowsour.2010.01.015`.

[91]   D. Dixon, D. J. Babu, A. Bhaskar, H.-M. Bruns, J. J. Schneider, F. Scheiba, H. Ehrenberg, *Beilstein J. Nanotechnol.* **2019**, 10, 1698–1706, DOI 10.3762/bjnano.10.165.

[92]   K. R. Kneten, R. L. McCreery, *Anal. Chem.* **1992**, 64, 2518–2524, DOI 10.1021/ac00045a011.

[93]   C. A. McDermott, *J. Electrochem. Soc.* **1993**, 140, 2593, DOI 10.1149/1.2220868.

[94]   P. Chen, M. A. Fryling, R. L. McCreery, *Anal. Chem.* **1995**, 67, 3115–3122, DOI 10.1021/ac00114a004.

[95]   L. Zeng, T. Zhao, L. Wei, *Adv. Sustainable Syst.* **2018**, 2, 1–9, DOI 10.1002/adsu.201700148.

[96]   M. A. Miller, A. Bourke, N. Quill, J. S. Wainright, R. P. Lynch, D. N. Buckley, R. F. Savinell, *J. Electrochem. Soc.* **2016**, 163, A2095–A2102, DOI 10.1149/2.1091609jes.

[97]   X.-W. Wu, T. Yamamura, S. Ohta, Q.-X. Zhang, F.-C. Lv, C.-M. Liu, K. Shirasaki, I. Satoh, T. Shikama, D. Lu, S.-Q. Liu, *J. Appl. Electrochem.* **2011**, 41, 1183–1190, DOI 10.1007/s10800-011-0343-7.

[98]   W. Zhang, J. Xi, Z. Li, H. Zhou, Le Liu, Z. Wu, X. Qiu, *Electrochim. Acta* **2013**, 89, 429–435, DOI 10.1016/j.electacta.2012.11.072.

[99]   M. Wu, K. Binnemans, J. Fransaer, *Electrochim. Acta* **2014**, 147, 451–459, DOI 10.1016/j.electacta.2014.08.111.

[100] Y. Huang, Q. Deng, X. Wu, S. Wang, *Int. J. Hydrogen Energy* **2017**, 42, 7177–7185, DOI 10.1016/j.ijhydene.2016.04.004.

[101] S. Jeong, S. Kim, Y. Kwon, *Electrochim. Acta* **2013**, 114, 439–447, DOI 10.1016/j.electacta.2013.10.011.

[102] Z. Gonzalez, A. Sanchez, C. Blanco, M. Granda, R. Menendez, R. Santamaria, *Electrochem. Commun.* **2011**, 13, 1379–1382, DOI 10.1016/j.elecom.2011.08.017.

[103] E. Agar, C. R. Dennison, K. W. Knehr, E. C. Kumbur, *J. Power Sources* **2013**, 225, 89–94, DOI 10.1016/j.jpowsour.2012.10.016.

[104] D. Aaron, C.-N. Sun, M. Bright, A. B. Papandrew, M. M. Mench, T. A. Zawodzinski, *ECS Electrochem. Lett.* **2013**, 2, A29–A31, DOI 10.1149/2.001303eel.

[105] J. LANGNER, J. MELKE, H. EHRENBERG, C. ROTH, *ECS Trans.* **2014**, 58, 1–7, DOI 10.1149/05837.0001ecst.

[106] J. LANGNER, M. BRUNS, D. DIXON, A. NEFEDOV, C. WÖLL, F. SCHEIBA, H. EHRENBERG, C. ROTH, J. MELKE, *J. Power Sources* **2016**, 321, 210–218, DOI 10.1016/j.jpowsour.2016.04.128.

[107] I. DERR, M. BRUNS, J. LANGNER, A. FETYAN, J. MELKE, C. ROTH, *J. Power Sources* **2016**, 325, 351–359, DOI 10.1016/j.jpowsour.2016.06.040.

[108] M. V. HOLLAND-CUNZ, J. FRIEDL, U. STIMMING, *J. Electroanal. Chem.* **2018**, 819, 306–311, DOI 10.1016/j.jelechem.2017.10.061.

[109] H. AGARWAL, J. FLORIAN, B. R. GOLDSMITH, N. SINGH, *ACS Energy Lett.* **2019**, 2368–2377, DOI 10.1021/acsenergylett.9b01423.

[110] M. PUMERA, Y. MIYAHARA, *Nanoscale* **2009**, 1, 260–265, DOI 10.1039/b9nr00071b.

[111] M. PUMERA, A. AMBROSI, E. L. K. CHNG, *Chem. Sci.* **2012**, 3, 3347–3355, DOI 10.1039/c2sc21374e.

[112] L. CAO, M. SKYLLAS-KAZACOS, C. MENICTAS, J. NOACK, *J. Energy Chem.* **2018**, 27, 1269–1291, DOI 10.1016/j.jechem.2018.04.007.

[113] N. ROZNYATOVSKAYA, J. NOACK, K. PINKWART, J. TÜBKE, *Curr. Opin. Electrochem.* **2020**, 19, 42–48, DOI 10.1016/j.coelec.2019.10.003.

[114] B. SUN, M. SKYLLAS-KAZAKOS, *Electrochim. Acta* **1991**, 36, 513–517, DOI 10.1016/0013-4686(91)85135-T.

[115] K. AMINI, J. GOSTICK, M. D. PRITZKER, *Adv. Funct. Mater.* **2020**, 30, 1910564, DOI 10.1002/adfm.201910564.

[116] K. J. KIM, M.-S. PARK, Y.-J. KIM, J. H. KIM, S. X. DOU, M. SKYLLAS-KAZACOS, *J. Mater. Chem. A* **2015**, 3, 16913–16933, DOI 10.1039/C5TA02613J.

[117] T. LIU, X. LI, H. NIE, C. XU, H. ZHANG, *J. Power Sources* **2015**, 286, 73–81, DOI 10.1016/j.jpowsour.2015.03.148.

[118] B. LIU, S. LIU, Z. HE, K. ZHAO, J. LI, X. WEI, R. HUANG, Y. YANG, *Ionics* **2019**, 25, 4231–4241, DOI 10.1007/s11581-019-02988-5.

[119] D. J. SUAREZ, Z. GONZALEZ, C. BLANCO, M. GRANDA, R. MENENDEZ, R. SANTAMARIA, *ChemSusChem* **2014**, 7, 914–918, DOI 10.1002/cssc.201301045.

[120] G. Wei, X. Fan, J. Liu, C. Yan, *J. Power Sources* **2015**, 281, 1–6, DOI 10.1016/j.jpowsour.2015.01.161.

[121] B. Li, M. Gu, Z. Nie, Y. Shao, Q. Luo, X. Wei, X. Li, J. Xiao, C. Wang, V. Sprenkle, W. Wang, *Nano Lett.* **2013**, 13, 1330–1335, DOI 10.1021/nl400223v.

[122] Y. Liu, F. Liang, Y. Zhao, L. Yu, Le Liu, J. Xi, *J. Energy Chem.* **2018**, DOI 10.1016/j.jechem.2018.01.028.

[123] Y. Wu, R. Holze, *Batteries* **2018**, 4, 47, DOI 10.3390/batteries 4030047.

[124] H. Zhou, J. Xi, Z. Li, Z. Zhang, L. Yu, Le Liu, X. Qiu, L. Chen, *RSC Adv.* **2014**, 4, 61912–61918, DOI 10.1039/C4RA12339E.

[125] Y. Xiang, W. A. Daoud, *J. Electrochem. Soc.* **2017**, 164, A2256–A2261, DOI 10.1149/2.0061712jes.

[126] A. W. Bayeh, D. M. Kabtamu, Y.-C. Chang, G.-C. Chen, H.-Y. Chen, G.-Y. Lin, T.-R. Liu, T. H. Wondimu, K.-C. Wang, C.-H. Wang, *ACS Sustainable Chem. Eng.* **2018**, 6, 3019–3028, DOI 10.1021/acssuschemeng.7b02752.

[127] X. Feng, S. Ren, K. Li, R. Zhang, J. Chen, Y. Li, Y. Jiang, Z. He, J. Zhu, W. Meng, L. Dai, H. Zhou, L. Wang, *J. Electrochem. Soc.* **2020**, 167, 100522, DOI 10.1149/1945-7111/ab9460.

[128] L. Cao, M. Skyllas-Kazacos, D.-W. Wang, *ChemElectroChem* **2017**, 4, 1836–1839, DOI 10.1002/celc.201700376.

[129] J. Shen, S. Liu, Z. He, L. Shi, *Electrochim. Acta* **2015**, 151, 297–305, DOI 10.1016/j.electacta.2014.11.060.

[130] M. Kim, H. Yoo, G. Lee, J. Choi, *Electrochim. Acta* **2017**, 246, 190–196, DOI 10.1016/j.electacta.2017.05.203.

[131] S. Cherevko, N. Kulyk, K. J. J. Mayrhofer, *Nano Energy* **2016**, 29, 275–298, DOI 10.1016/j.nanoen.2016.03.005.

[132] L. Dubau, L. Castanheira, F. Maillard, M. Chatenet, O. Lottin, G. Maranzana, J. Dillet, A. Lamibrac, J.-C. Perrin, E. Moukheiber, A. ElKaddouri, G. de Moor, C. Bas, L. Flandin, N. Caque, *Wiley Interdiscip. Rev.: Energy Environ.* **2014**, 3, 540–560, DOI 10.1002/wene.113.

[133] A. Sorrentino, K. Sundmacher, T. Vidakovic-Koch, *Energies* **2020**, 13, 5825, DOI 10.3390/en13215825.

[134] X.-Z. Yuan, C. Song, A. Platt, N. Zhao, H. Wang, H. Li, K. Fatih, D. Jang, *Int. J. Energy Res.* **2019**, DOI 10.1002/er.4607.

[135] N. Roznyatovskaya, T. Herr, M. Küttinger, M. Fühl, J. Noack, K. Pinkwart, J. Tübke, *J. Power Sources* **2016**, 302, 79–83, DOI 10.1016/j.jpowsour.2015.10.021.

[136] H. Liu, Q. Xu, C. Yan, Y. Qiao, *Electrochim. Acta* **2011**, 56, 8783–8790, DOI 10.1016/j.electacta.2011.07.083.

[137] F. Mohammadi, P. Timbrell, S. Zhong, C. Padeste, M. Skyllas-Kazacos, *J. Power Sources* **1994**, 52, 61–68, DOI 10.1016/0378-7753(94)01938-X.

[138] C. Sun, J. Chen, H. Zhang, X. Han, Q. Luo, *J. Power Sources* **2010**, 195, 890–897, DOI 10.1016/j.jpowsour.2009.08.041.

[139] H. Liu, Q. Xu, C. Yan, *Electrochem. Commun.* **2013**, 28, 58–62, DOI 10.1016/j.elecom.2012.12.011.

[140] L. Eifert, Z. Jusys, R. J. Behm, R. Zeis, *Carbon* **2020**, 158, 580–587, DOI 10.1016/j.carbon.2019.11.029.

[141] O. Nibel, S. M. Taylor, A. Pătru, E. Fabbri, L. Gubler, T. J. Schmidt, *J. Electrochem. Soc.* **2017**, 164, A1608–A1615, DOI 10.1149/2.1081707jes.

[142] J. Melke, P. Jakes, J. Langner, L. Riekehr, U. Kunz, Z. Zhao-Karger, A. Nefedov, H. Sezen, C. Wöll, H. Ehrenberg, C. Roth, *Carbon* **2014**, 78, 220–230, DOI 10.1016/j.carbon.2014.06.075.

[143] I. Derr, A. Fetyan, K. Schutjajew, C. Roth, *Electrochim. Acta* **2017**, 224, 9–16, DOI 10.1016/j.electacta.2016.12.043.

[144] F. Chen, J. Liu, H. Chen, C. Yan, *Int. J. Electrochem. Sci.* **2012**, 7, 3750–3764.

[145] C.-N. Sun, F. M. Delnick, D. S. Aaron, A. B. Papandrew, M. M. Mench, T. A. Zawodzinski, *ECS Electrochem. Lett.* **2013**, 2, A43–A45, DOI 10.1149/2.001305eel.

[146] P. Mazur, J. Mrlik, J. Pocedic, J. Vrana, J. Dundalek, J. Kosek, T. Bystron, *J. Power Sources* **2019**, 414, 354–365, DOI 10.1016/j.jpowsour.2019.01.019.

[147] P. Mazur, J. Mrlik, J. Charvat, J. Pocedic, J. Vrana, J. Dundalek, J. Kosek, *MethodsX* **2019**, 6, 534–539, DOI 10.1016/j.mex.2019.03.007.

[148] *Impedance spectroscopy: Theory, experiment, and applications*, 2nd Edition, (Eds.: E. Barsoukov, J. R. Macdonald), Wiley & Sons, Hoboken, NJ, **2005**.

[149] A. Lasia, *Electrochemical Impedance Spectroscopy and its Applications*, Springer New York, New York, NY, **2014**, DOI 10.1007/978-1-4614-8933-7.

[150] V. F. Lvovich, *Impedance spectroscopy: Applications to electrochemical and dielectric phenomena*, Wiley & Sons, Hoboken, NJ, **2012**.

[151] X. Zhang, T. Zhang, H. Chen, Y. Cao, *Appl. Energy* **2021**, 286, 116481, DOI 10.1016/j.apenergy.2021.116481.

[152] A. R. C. Bredar, A. L. Chown, A. R. Burton, B. H. Farnum, *ACS Appl. Energy Mater.* **2020**, 3, 66–98, DOI 10.1021/acsaem.9b01965.

[153] N. Meddings, M. Heinrich, F. Overney, J.-S. Lee, V. Ruiz, E. Napolitano, S. Seitz, G. Hinds, R. Raccichini, M. Gaberscek, J. Park, *J. Power Sources* **2020**, 480, 228742, DOI 10.1016/j.jpowsour.2020.228742.

[154] H. Li, T. Zhang, Z. Yang, Y. Shi, Q. Zhuang, Y. Cui, *Int. J. Electrochem. Sci.* **2021**, 16, 210229, DOI 10.20964/2021.02.33.

[155] L.-P. He, K. Li, Y. Zhang, J. Liu, *ACS Appl. Mater. Interfaces* **2020**, 12, 28253–28263, DOI 10.1021/acsami.0c06824.

[156] S. Y. Vassiliev, V. V. Sentyurin, E. E. Levin, V. A. Nikitina, *Electrochim. Acta* **2019**, 302, 316–326, DOI 10.1016/j.electacta.2019.02.043.

[157] A. Yano, K. Hikima, J. Hata, K. Suzuki, M. Hirayama, R. Kanno, *J. Electrochem. Soc.* **2018**, 165, A3221–A3229, DOI 10.1149/2.0151814jes.

[158] R. Morasch, J. Keilhofer, H. A. Gasteiger, B. Suthar, *J. Electrochem. Soc.* **2021**, 168, 080519, DOI 10.1149/1945-7111/ac1892.

[159] W. Kim, D. Jang, H.-J. Kim, *J. Power Sources* **2021**, 510, 230338, DOI 10.1016/j.jpowsour.2021.230338.

[160] T. ZINKEVICH, B. SCHWARZ, P. BRAUN, A. WEBER, H. EHRENBERG, S. INDRIS, *Solid State Ion.* **2020**, 357, 115486, DOI 10.1016/j.ssi.2020.115486.

[161] A. S. KEEFE, R. WEBER, I. G. HILL, J. R. DAHN, *J. Electrochem. Soc.* **2020**, 167, 120507, DOI 10.1149/1945-7111/abaa1b.

[162] J. XU, C. C. MI, B. CAO, J. CAO, *J. Power Sources* **2013**, 233, 277–284, DOI 10.1016/j.jpowsour.2013.01.094.

[163] A. LA RUE, P. J. WEDDLE, M. MA, C. HENDRICKS, R. J. KEE, T. L. VINCENT, *J. Electrochem. Soc.* **2019**, 166, A4041–A4046, DOI 10.1149/2.0221916jes.

[164] J. L. JESPERSEN, A. E. TØNNESEN, K. NØRREGAARD, L. OVERGAARD, F. ELEFSEN, *World Electr. Veh. J.* **2009**, 3, 127–133, DOI 10.3390/wevj3010127.

[165] F. LENG, C. M. TAN, R. YAZAMI, M. D. LE, *J. Power Sources* **2014**, 255, 423–430, DOI 10.1016/j.jpowsour.2014.01.020.

[166] R. MINGANT, J. BERNARD, V. SAUVANT MOYNOT, A. DELAILLE, S. MAILLEY, J.-L. HOGNON, F. HUET, *ECS Trans.* **2010**, 33, 41–53, DOI 10.1149/1.3589920.

[167] R. XIONG, J. TIAN, H. MU, C. WANG, *Appl. Energy* **2017**, 207, 372–383, DOI 10.1016/j.apenergy.2017.05.124.

[168] X. WANG, X. WEI, H. DAI, *J. Energy Storage* **2019**, 21, 618–631, DOI 10.1016/j.est.2018.11.020.

[169] M. GALEOTTI, L. CINÀ, C. GIAMMANCO, S. CORDINER, A. DI CARLO, *Energy* **2015**, 89, 678–686, DOI 10.1016/j.energy.2015.05.148.

[170] J. P. SCHMIDT, S. ARNOLD, A. LOGES, D. WERNER, T. WETZEL, E. IVERS-TIFFÉE, *J. Power Sources* **2013**, 243, 110–117, DOI 10.1016/j.jpowsour.2013.06.013.

[171] L. RAIJMAKERS, D. L. DANILOV, J. VAN LAMMEREN, M. LAMMERS, P. NOTTEN, *J. Power Sources* **2014**, 247, 539–544, DOI 10.1016/j.jpowsour.2013.09.005.

[172] J. G. ZHU, Z. C. SUN, X. Z. WEI, H. F. DAI, *J. Power Sources* **2015**, 274, 990–1004, DOI 10.1016/j.jpowsour.2014.10.182.

[173] X. WANG, X. WEI, Q. CHEN, J. ZHU, H. DAI, *J. Energy Storage* **2019**, 26, 100952, DOI 10.1016/j.est.2019.100952.

[174] H. BEELEN, L. RAIJMAKERS, M. DONKERS, P. NOTTEN, H. J. BERG-VELD, *Appl. Energy* **2016**, 175, 128–140, DOI 10.1016/j.apenergy.2016.04.103.

[175] P. HAUSSMANN, J. MELBERT, *SAE Int. J. Altern. Powertrains* **2017**, 6, 261–270, DOI 10.4271/2017-01-1215.

[176] S. SCHINDLER, M. A. DANZER, *J. Energy Storage* **2017**, 12, 157–166, DOI 10.1016/j.est.2017.05.002.

[177] J. XIA, K. J. NELSON, Z. LU, J. R. DAHN, *J. Power Sources* **2016**, 329, 387–397, DOI 10.1016/j.jpowsour.2016.08.100.

[178] R. PETIBON, J. XIA, L. MA, M. K. G. BAUER, K. J. NELSON, J. R. DAHN, *J. Electrochem. Soc.* **2016**, 163, A2571–A2578, DOI 10.1149/2.0321613jes.

[179] P. G. KITZ, M. J. LACEY, P. NOVAK, E. J. BERG, *J. Power Sources* **2020**, 477, 228567, DOI 10.1016/j.jpowsour.2020.228567.

[180] G. KWAK, J. PARK, J. LEE, S. KIM, I. JUNG, *J. Power Sources* **2007**, 174, 484–492, DOI 10.1016/j.jpowsour.2007.06.169.

[181] J. VETTER, P. NOVÁK, M. R. WAGNER, C. VEIT, K.-C. MÖLLER, J. O. BESENHARD, M. WINTER, M. WOHLFAHRT-MEHRENS, C. VOGLER, A. HAMMOUCHE, *J. Power Sources* **2005**, 147, 269–281, DOI 10.1016/j.jpowsour.2005.01.006.

[182] K. AMINE, C. H. CHEN, J. LIU, M. HAMMOND, A. JANSEN, D. DEES, I. BLOOM, D. VISSERS, G. HENRIKSEN, *J. Power Sources* **2001**, 97-98, 684–687, DOI 10.1016/S0378-7753(01)00701-7.

[183] T. P. HEINS, N. SCHLÜTER, U. SCHRÖDER, *ChemElectroChem* **2017**, 4, 2921–2927, DOI 10.1002/celc.201700686.

[184] P. SVENS, R. ERIKSSON, J. HANSSON, M. BEHM, T. GUSTAFSSON, G. LINDBERGH, *J. Power Sources* **2014**, 270, 131–141, DOI 10.1016/j.jpowsour.2014.07.050.

[185] X. ZHOU, J. HUANG, Z. PAN, M. OUYANG, *J. Power Sources* **2019**, 426, 216–222, DOI 10.1016/j.jpowsour.2019.04.040.

[186] R. CHATTOT, S. ESCRIBANO, *Int. J. Hydrogen Energy* **2015**, 40, 5367–5374, DOI 10.1016/j.ijhydene.2015.01.066.

[187] K. ZHANG, C. YAN, A. TANG, *Energy Storage Mater.* **2021**, 34, 301–310, DOI 10.1016/j.ensm.2020.10.005.

[188] J. N. NOACK, L. VORHAUSER, K. PINKWART, J. TUEBKE, *ECS Trans.* **2011**, 33, 3–9, DOI 10.1149/1.3589916.

[189] C. CHOI, S. KIM, R. KIM, J. LEE, J. HEO, H.-T. KIM, *J. Ind. Eng. Chem.* **2019**, 70, 355–362, DOI 10.1016/j.jiec.2018.10.036.

[190] S. MEHBOOB, A. MEHMOOD, J.-Y. LEE, H.-J. SHIN, J. HWANG, S. ABBAS, H. Y. HA, *J. Mater. Chem. A* **2017**, 5, 17388–17400, DOI 10.1039/c7ta05657e.

[191] I. DERR, D. PRZYREMBEL, J. SCHWEER, A. FETYAN, J. LANGNER, J. MELKE, M. WEINELT, C. ROTH, *Electrochim. Acta* **2017**, 246, 783–793, DOI 10.1016/j.electacta.2017.06.050.

[192] M. NOURANI, B. I. ZACKIN, D. C. SABARIRAJAN, R. TASPINAR, K. ARTYUSHKOVA, F. LIU, I. V. ZENYUK, E. AGAR, *J. Electrochem. Soc.* **2019**, 166, A353–A363, DOI 10.1149/2.1041902jes.

[193] H. SHARMA, M. KUMAR, *J. Power Sources* **2021**, 494, 229753, DOI 10.1016/j.jpowsour.2021.229753.

[194] P. RAO, S. JAYANTI, *J. Power Sources* **2021**, 482, 228988, DOI 10.1016/j.jpowsour.2020.228988.

[195] A. BHATTACHARJEE, A. ROY, N. BANERJEE, S. PATRA, H. SAHA, *J. Power Sources* **2018**, 396, 506–518, DOI 10.1016/j.jpowsour.2018.06.017.

[196] A. TROVO, W. ZAMBONI, M. GUARNIERI, *J. Power Sources* **2021**, 493, 229703, DOI 10.1016/j.jpowsour.2021.229703.

[197] M. A. DANZER, *Batteries* **2019**, 5, 53, DOI 10.3390/batteries5030053.

[198] P. AGARWAL, M. E. ORAZEM, L. H. GARCI-RUBIO, *J. Electrochem. Soc.* **1992**, 139, 1917–1927, DOI 10.1149/1.2069522.

[199] M. SCHOENLEBER, E. IVERS-TIFFEE, *Electrochem. Commun.* **2015**, 58, 15–19, DOI 10.1016/j.elecom.2015.05.018.

[200] K. T. MALKOW, *J. Electroanal. Chem.* **2019**, 838, 221–231, DOI 10.1016/j.jelechem.2019.01.057.

[201] C. DÉSILETS, A. LASIA, *Electrochim. Acta* **2012**, 78, 286–293, DOI 10.1016/j.electacta.2012.05.102.

[202] R. L. SACCI, F. SELAND, D. A. HARRINGTON, *Electrochim. Acta* **2014**, 131, 13–19, DOI 10.1016/j.electacta.2014.02.120.

[203] Y. HOSHI, Y. ITO, T. KATO, I. SHITANDA, M. ITAGAKI, *Electrochemistry* **2015**, 83, 142–149, DOI 10.5796/electrochemistry.83.142.

[204] B. A. BOUKAMP, *Solid State Ion.* **1986**, 20, 31–44, DOI 10.1016/0167-2738(86)90031-7.

[205] R. D. L. KRONIG, *J. Opt. Soc. Am.* **1926**, 12, 547, DOI 10.1364/JOSA.12.000547.

[206] H. A. KRAMERS, *Phys. Z.* **1929**, 30, 522–523.

[207] F. FASMIN, R. SRINIVASAN, *J. Solid State Electrochem.* **2015**, 19, 1833–1847, DOI 10.1007/s10008-015-2824-9.

[208] T. MALKOW, *ChemElectroChem* **2017**, 4, 2777–2782, DOI 10.1002/celc.201700630.

[209] B. A. BOUKAMP, *J. Electrochem. Soc.* **1995**, 142, 1885, DOI 10.1149/1.2044210.

[210] M. SCHÖNLEBER, D. KLOTZ, E. IVERS-TIFFÉE, *Electrochim. Acta* **2014**, 131, 20–27, DOI 10.1016/j.electacta.2014.01.034.

[211] G. S. POPKIROV, R. N. SCHINDLER, *Rev. Sci. Instrum.* **1993**, 64, 3111–3115, DOI 10.1063/1.1144316.

[212] T. BREUGELMANS, E. TOURWÉ, Y. VAN INGELGEM, J. WIELANT, T. HAUFFMAN, R. HAUSBRAND, R. PINTELON, A. HUBIN, *Electrochem. Commun.* **2010**, 12, 2–5, DOI 10.1016/j.elecom.2009.10.008.

[213] D. KOSTER, G. DU, A. BATTISTEL, F. LA MANTIA, *Electrochim. Acta* **2017**, 246, 553–563, DOI 10.1016/j.electacta.2017.06.060.

[214] U. PLIQUET, E. GERSING, F. PLIQUETT, *Biomed Eng-Biomed Te* **2000**, 45, 6–13, DOI 10.1515/bmte.2000.45.1-2.6.

[215] E. BARSOUKOV, S. H. RYU, H. LEE, *J. Electroanal. Chem.* **2002**, 536, 109–122, DOI 10.1016/S0022-0728(02)01209-3.

[216] S.-M. PARK, J.-S. YOO, *Anal. Chem.* **2003**, 75, 455 A–461 A, DOI 10.1021/ac0313973.

[217] D. KLOTZ, M. SCHÖNLEBER, J. P. SCHMIDT, E. IVERS-TIFFÉE, *Electrochim. Acta* **2011**, 56, 8763–8769, DOI 10.1016/j.electacta.2011.07.096.

[218] J. P. SCHMIDT, E. IVERS-TIFFÉE, *J. Power Sources* **2016**, 315, 316–323, DOI 10.1016/j.jpowsour.2016.03.026.

[219] J. HOUSER, J. CLEMENT, A. PEZESHKI, M. M. MENCH, *J. Power Sources* **2016**, 302, 369–377, DOI `10.1016/j.jpowsour.2015.09.095`.

[220] A. M. PEZESHKI, R. L. SACCI, G. M. VEITH, T. A. ZAWODZINSKI, M. M. MENCH, *J. Electrochem. Soc.* **2015**, 163, A5202–A5210, DOI `10.1149/2.0251601jes`.

[221] R. M. DARLING, M. L. PERRY, *ECS Trans.* **2013**, 53, 31–38, DOI `10.1149/05307.0031ecst`.

[222] J. SCHNEIDER, E. BULCZAK, G. A. EL-NAGAR, M. GEBHARD, P. KUBELLA, M. SCHNUCKLAKE, A. FETYAN, I. DERR, C. ROTH, *Batteries* **2019**, 5, 16, DOI `10.3390/batteries5010016`.

[223] K. S. COLE, R. H. COLE, *J. Chem. Phys.* **1941**, 9, 341–351, DOI `10.1063/1.1750906`.

[224] J. R. MACDONALD, M. K. BRACHMAN, *Rev. Mod. Phys.* **1956**, 28, 393–422, DOI `10.1103/RevModPhys.28.393`.

[225] J. R. MACDONALD, *Electrochim. Acta* **1990**, 35, 1483–1492, DOI `10.1016/0013-4686(90)80002-6`.

[226] J. R. MACDONALD, *J. Non-Cryst. Solids* **1996**, 197, 83–110.

[227] J. R. MACDONALD, *J. Chem. Phys.* **1998**, 102, 6241, DOI `10.1063/1.469070`.

[228] J. R. MACDONALD, *Inverse Probl.* **2000**, 16, 1561, DOI `10.1088/0266-5611/16/5/324`.

[229] A. D. FRANKLIN, H. J. DE BRUIN, *Phys. Status Solidi A* **1983**, 75, 647–656, DOI `10.1002/pssa.2210750240`.

[230] F. DION, A. LASIA, *J. Electroanal. Chem.* **1999**, 475, 28–37, DOI `10.1016/S0022-0728(99)00334-4`.

[231] H. SCHICHLEIN, A. C. MÜLLER, M. VOIGTS, A. KRÜGEL, E. IVERS-TIFFÉE, *J. Appl. Electrochem.* **2002**, 32, 875–882, DOI `10.1023/A:1020599525160`.

[232] M. SACCOCCIO, T. H. WAN, C. CHEN, F. CIUCCI, *Electrochim. Acta* **2014**, 147, 470–482, DOI `10.1016/j.electacta.2014.09.058`.

[233] T. H. WAN, M. SACCOCCIO, C. CHEN, F. CIUCCI, *Electrochim. Acta* **2015**, 184, 483–499, DOI `10.1016/j.electacta.2015.09.097`.

[234] Y. ZHANG, Y. CHEN, M. LI, M. YAN, M. NI, C. XIA, *J. Power Sources* **2016**, 308, 1–6, DOI `10.1016/j.jpowsour.2016.01.067`.

[235] A. MERTENS, J. GRANWEHR, *J. Energy Storage* **2017**, 13, 401–408, DOI `10.1016/j.est.2017.07.029`.

[236] A. LEONIDE, V. SONN, A. WEBER, E. IVERS-TIFFEE, *J. Electrochem. Soc.* **2007**, 155, B36–B41, DOI `10.1149/1.2801372`.

[237] C. ENDLER, A. LEONIDE, A. WEBER, F. TIETZ, E. IVERS-TIFFÉE, *J. Electrochem. Soc.* **2010**, 157, B292, DOI `10.1149/1.3270047`.

[238] A. WEISS, S. SCHINDLER, S. GALBIATI, M. A. DANZER, R. ZEIS, *Electrochim. Acta* **2017**, 230, 391–398, DOI `10.1016/j.electacta.2017.02.011`.

[239] B. A. BOUKAMP, A. ROLLE, *Solid State Ion.* **2018**, 314, 103–111, DOI `10.1016/j.ssi.2017.11.021`.

[240] S. SIMON ARAYA, F. ZHOU, S. LENNART SAHLIN, S. THOMAS, C. JEPPESEN, S. KNUDSEN KÆR, *Energies* **2019**, 12, 152, DOI `10.3390/en12010152`.

[241] J. P. SCHMIDT, T. CHROBAK, M. ENDER, J. ILLIG, D. KLOTZ, E. IVERS-TIFFÉE, *J. Power Sources* **2011**, 196, 5342–5348, DOI `10.1016/j.jpowsour.2010.09.121`.

[242] J. P. SCHMIDT, P. BERG, M. SCHÖNLEBER, A. WEBER, E. IVERS-TIFFÉE, *J. Power Sources* **2013**, 221, 70–77, DOI `10.1016/j.jpowsour.2012.07.100`.

[243] J. ILLIG, J. P. SCHMIDT, M. WEISS, A. WEBER, E. IVERS-TIFFÉE, *J. Power Sources* **2013**, 239, 670–679, DOI `10.1016/j.jpowsour.2012.12.020`.

[244] E. IVERS-TIFFÉE, A. WEBER, *J. Ceram. Soc. Jpn.* **2017**, 125, 193–201, DOI `10.2109/jcersj2.16267`.

[245] I. FREDHOLM, *Acta Math.* **1903**, 27, 365–390, DOI `10.1007/BF02421317`.

[246] E. HELLINGER, O. TOEPLITZ, *Integralgleichungen und Gleichungen mit Unendlichvielen Unbekannten: Sonderausgabe aus der Encyklopädie der Mathematischen Wissenschaften*, Vieweg+Teubner Verlag, Wiesbaden, **1928**, DOI `10.1007/978-3-663-15917-9`.

[247] L. LANDWEBER, *Am. J. Math.* **1951**, 73, 615, DOI `10.2307/2372313`.

[248] J. WEESE, *Comput. Phys. Commun.* **1992**, 69, 99–111, DOI `10.1016/0010-4655(92)90132-I`.

[249] M. HAHN, S. SCHINDLER, L.-C. TRIEBS, M. A. DANZER, *Batteries* **2019**, 5, 43, DOI `10.3390/batteries5020043`.

[250] Y. ZHANG, Y. CHEN, M. YAN, F. CHEN, *J. Power Sources* **2015**, 283, 464–477, DOI `10.1016/j.jpowsour.2015.02.107`.

[251] L. ZHANG, Y. ZENG, Z. CHENG, *J. Mol. Liq.* **2016**, 214, 175–191, DOI `10.1016/j.molliq.2015.12.013`.

[252] T. HÖRLIN, *Solid State Ion.* **1993**, 67, 85–96, DOI `10.1016/0167-2738(93)90313-R`.

[253] T. HÖRLIN, *Solid State Ion.* **1998**, 107, 241–253, DOI `10.1016/S0167-2738(98)00008-3`.

[254] A. B. TESLER, D. R. LEWIN, S. BALTIANSKI, Y. TSUR, *J. Electroceram.* **2010**, 24, 245–260, DOI `10.1007/s10832-009-9565-z`.

[255] S. HERSHKOVITZ, S. BALTIANSKI, Y. TSUR, *Solid State Ion.* **2011**, 188, 104–109, DOI `10.1016/j.ssi.2010.10.004`.

[256] B. A. BOUKAMP, *Electrochim. Acta* **2017**, 252, 154–163, DOI `10.1016/j.electacta.2017.08.154`.

[257] A. N. TIKHONOV, *Dokl. Akad. Nauk SSSR* **1943**, 39, 195–198.

[258] C. L. LAWSON, R. J. HANSON, *Solving Least Squares Problems*, Society for Industrial and Applied Mathematics, Philadelphia, **1995**, DOI `10.1137/1.9781611971217`.

[259] L. WU, *Electron. Trans. Numer. Anal.* **2003**, 16, 107–128.

[260] L. REICHEL, G. RODRIGUEZ, *Numer. Algorithms* **2013**, 63, 65–87, DOI `10.1007/s11075-012-9612-8`.

[261] P. C. HANSEN, *SIAM Rev.* **1992**, 34, 561–580, DOI `10.1137/1034115`.

[262] P. C. HANSEN, D. P. O'LEARY, *SIAM J. Sci. Comput.* **1993**, 14, 1487–1503, DOI `10.1137/0914086`.

[263] P. C. HANSEN, *Numer. Algorithms* **2007**, 46, 189–194, DOI `10.1007/s11075-007-9136-9`.

[264] P. C. HANSEN, T. K. JENSEN, G. RODRIGUEZ, *J. Comput. Appl. Math.* **2007**, 198, 483–492, DOI `10.1016/j.cam.2005.09.026`.

[265] D. P. O'Leary, *SIAM J. Sci. Comput.* **2001**, 23, 1161–1171, DOI 10.1137/S1064827599354147.

[266] J. Castellanos, S. Gómez, V. Guerra, *Appl. Numer. Math.* **2002**, 43, 359–373, DOI 10.1016/S0168-9274(01)00179-9.

[267] C. R. Vogel, *Inverse Probl.* **1996**, 12, 535–547, DOI 10.1088/0266-5611/12/4/013.

[268] E. J. Fordham, A. Sezginer, L. D. Hall, *J. Magn. Reson. Ser. A.* **1995**, 113, 139–150, DOI 10.1006/jmra.1995.1073.

[269] J. Granwehr, P. J. Roberts, *J. Chem. Theory Comput.* **2012**, 8, 3473–3482, DOI 10.1021/ct3001393.

[270] L. Wei, T. S. Zhao, Q. Xu, X. L. Zhou, Z. H. Zhang, *Appl. Energy* **2017**, 190, 1112–1118, DOI 10.1016/j.apenergy.2017.01.039.

[271] Gamry Instruments, Application Note: Reference Electrodes, https://www.gamry.com/application-notes/instrumentation/reference-electrodes/ (visited on 12/16/2022).

[272] S. Fletcher, *Electrochem. Commun.* **2001**, 3, 692–696, DOI 10.1016/S1388-2481(01)00233-8.

[273] A. Sadkowski, J.-P. Diard, *Electrochim. Acta* **2010**, 55, 1907–1911, DOI 10.1016/j.electacta.2009.11.008.

[274] A. Battistel, M. Fan, J. Stojadinovic, F. La Mantia, *Electrochim. Acta* **2014**, 135, 133–138, DOI 10.1016/j.electacta.2014.05.011.

[275] G. J. Brug, A. van den Eeden, M. Sluyters-Rehbach, J. H. Sluyters, *J. Electroanal. Chem. Interfacial Electrochem.* **1984**, 176, 275–295, DOI 10.1016/S0022-0728(84)80324-1.

[276] C. H. Hsu, F. Mansfeld, *Corrosion* **2001**, 57, 747–748, DOI 10.5006/1.3280607.

[277] B. Hirschorn, M. E. Orazem, B. Tribollet, V. Vivier, I. Frateur, M. Musiani, *Electrochim. Acta* **2010**, 55, 6218–6227, DOI 10.1016/j.electacta.2009.10.065.

[278] M.-A. Goulet, M. Eikerling, E. Kjeang, *Electrochem. Commun.* **2015**, 57, 14–17, DOI 10.1016/j.elecom.2015.04.019.

[279] M. Skyllas-Kazacos, M. Kazacos, *J. Power Sources* **2011**, 196, 8822–8827, DOI 10.1016/j.jpowsour.2011.06.080.

[280] D. N. BUCKLEY, X. GAO, R. P. LYNCH, N. QUILL, M. J. LEAHY, *J. Electrochem. Soc.* **2014**, 161, A524–A534, DOI 10.1149/2.023404jes.

[281] C. PETCHSINGH, N. QUILL, J. T. JOYCE, D. N. EIDHIN, D. OBOROCEANU, C. LENIHAN, X. GAO, R. P. LYNCH, D. N. BUCKLEY, *J. Electrochem. Soc.* **2016**, 163, A5068–A5083, DOI 10.1149/2.0091601jes.

[282] S. RUDOLPH, U. SCHROEDER, I. M. BAYANOV, K. BLENKE, D. HAGE, *J. Electroanal. Chem.* **2013**, 694, 17–22, DOI 10.1016/j.jelechem.2013.01.042.

[283] X. ZANG, L. YAN, Y. YANG, H. PAN, Z. NIE, K. W. JUNG, Z. D. DENG, W. WANG, *Small Methods* **2019**, 3, 1900494, DOI 10.1002/smtd.201900494.

[284] I. KRONER, M. BECKER, T. TUREK, *Batteries* **2019**, 5, 5, DOI 10.3390/batteries5010005.

[285] X. LI, J. XIONG, A. TANG, Y. QIN, J. LIU, C. YAN, *Appl. Energy* **2018**, 211, 1050–1059, DOI 10.1016/j.apenergy.2017.12.009.

[286] S. RESSEL, F. BILL, L. HOLTZ, N. JANSHEN, A. CHICA, T. FLOWER, C. WEIDLICH, T. STRUCKMANN, *J. Power Sources* **2018**, 378, 776–783, DOI 10.1016/j.jpowsour.2018.01.006.

[287] R. M. DARLING, M. L. PERRY, *J. Electrochem. Soc.* **2014**, 161, A1381–A1387, DOI 10.1149/2.0941409jes.

[288] C.-N. SUN, F. M. DELNICK, D. S. AARON, A. B. PAPANDREW, M. M. MENCH, T. A. ZAWODZINSKI, *J. Electrochem. Soc.* **2014**, 161, A981–A988, DOI 10.1149/2.045406jes.

[289] R. SCHWEISS, C. MEISER, D. DAN, *Batteries* **2018**, 4, 55, DOI 10.3390/batteries4040055.

[290] M. GEBHARD, M. SCHNUCKLAKE, A. HILGER, M. RÖHE, M. OSENBERG, U. KREWER, I. MANKE, C. ROTH, *Energy Technol.* **2020**, 8, 1901214, DOI 10.1002/ente.201901214.

Bibliography

Abbreviations

ACCV	alternating current cyclic voltammetry
AEM	anion-exchange membrane
BET	Brunauer-Emmett-Teller
BMWi	Federal Ministry for Economic Affairs and Energy
BV	Butler-Volmer
CE	Coulombic efficiency
CEM	cation-exchange membrane
CNLS	complex non-linear least-squares
CPE	constant phase element
CT	X-ray computed tomography
CV	cyclic voltammetry
DHC	double half cell
DOE	U.S. Department of Energy
DPD	discharge power density
DRT	distribution of relaxation times
ECM	equivalent circuit model
ECSA	electrochemically active surface area
EDX	energy dispersive X-ray spectroscopy
EE	energy efficiency
EIS	electrochemical impedance spectroscopy
CE	counter electrode
HER	hydrogen evolution reaction
KK	Kramers-Kronig
NEXAFS	near-edge X-ray absorption fine structure spectroscopy

NNLS	non-negative least-squares
OCP	open-circuit potential
PAN	polyacrylonitrile
PEM	proton-exchange membrane
RDE	rotating disk electrode
RE	reference electrode
RFB	redox-flow battery
RRDE	rotating ring-disc electrode
SEM	scanning electron microscopy
SHE	standard hydrogen electrode
SOC	state of charge
SOH	state of health
TEM	transmission electron microscopy
TXRF	total reflection X-ray fluorescence
VE	voltage efficiency
VRFB	vanadium redox-flow battery
WE	working electrode
XPS	X-ray photoelectron spectroscopy

List of Figures

Acknowledgements

Thanks to whom thanks are due!

I hereby want to express my deepest, eternal gratitude to my supervisor Prof. Dr. Christina Roth. Christina, thank you for your trust and (especially) patience as well as your unparalleled support in any work-related issues and beyond. The time spent as part of your group let me grow not only in my profession but also as a person and will forever have a special place in my heart. Thank you for giving me this opportunity.

Special thanks are due to Prof. Dr. Beate Paulus for unhesitatingly taking over responsibility after Christina's relocation and for agreeing to become second reviewer of this thesis.

Furthermore, I would like to thank all my (former) colleagues at the AG Roth, especially Drs. Tintula and Prashant Khadke, Dr. Marcus Gebhard and Dr. Tim Tichter.

Tintula and Prashant, your expertise as well as your views on life really helped me to keep calm and focus and the truly important things.

Marcus and Tim - gentlemen, it was an honour to share the office with you! Together we had reached unthinkable levels of peak performance and our mutual *Mettwochs* will forever be missed. Your inputs have been invaluable for the success of this thesis. Marcus, your attitude really had a great and positive impact on how I get things done and Tim, I think it's safe to say that regularly having coffee with you taught me more about electrochemistry than any book or lecture would ever be able to.

Thanks to Fabian Krieg for introducing me to programming with python and advancing my aspirations to create documents with latex.

Thanks be expressed to all co-authors and collaboration partners, including

those of the joint research project DegraBat. Our discussions and projects meetings were quite enjoyable. In particular, I want to thank Dr. Rüdiger Schweiß and Dr. Peter Fischer for having me as guest at their respective labs, which provided many valuable insights. Received funding by the BMWi is also gratefully acknowledged.

Finally, I want to thank all my friends and family for their constant support. Especially my lovely wife and son who endured having this bearded hermit in their home desperately trying to finish his thesis for the last couple of weeks...